Development of a Model for Predicting the Transmission of Sonic Booms into Buildings at Low Frequency

Marcel C. Remillieux

Dissertation submitted to the faculty of the Virginia Polytechnic Institute and State University in partial fulfillment of the requirements for the degree of

Doctor of Philosophy
in
Mechanical Engineering

Dr. Ricardo A. Burdisso, Chairman
Dr. Christopher R. Fuller
Dr. Roop L. Mahajan (non-voting member)
Dr. Marty E. Johnson
Dr. Georg Reichard
Dr. Patricio A. Ravetta

May 3, 2010
Blacksburg, Virginia

Keywords: sonic boom, residential building, fluid-structure interaction, modal decomposition, finite-element method, vibration response, interior acoustic response.

Development of a Model for Predicting the Transmission of Sonic Booms into Buildings at Low Frequency

Marcel C. Remillieux

ABSTRACT

Recent progresses by the aircraft industry in the development of a quieter supersonic transport have opened the possibility of overland supersonic flights, which are currently banned by aviation authorities in most countries. For the ban to be lifted, the sonic booms the aircraft generate at supersonic speed must be acceptable from a human-perception point of view, in particular inside buildings. The problem of the transmission of sonic booms inside buildings can be divided in several aspects such as the external pressure loading, structure vibration, and interior acoustic response. Past investigations on this problem have tackled all these aspects but were limited to simple structures and often did not account for the coupled fluid-structure interaction. A more comprehensive work that includes all the effects of sonic booms to ultimately predict the noise exposure inside realistic building structures, e.g. residential houses, has never been reported. Thus far, these effects could only be investigated experimentally, e.g. flight tests.

In this research, a numerical model and a computer code are developed within the above context to predict the vibro-acoustic response of simplified building structures exposed to sonic booms, at low frequency. The model is applicable to structures with multiple rectangular cavities, isolated or interconnected with openings. The response of the fluid-structure system, including their fully coupled interaction, is computed in the time domain using a modal-decomposition approach for both the structural and acoustic systems. In the dynamic equations, the structural displacement is expressed in terms of summations over the "in vacuo" normal modes of vibration. The interior pressure is expressed in terms of summations over the acoustic modes of the rooms with perfectly reflecting surfaces (hard walls). This approach is simple to implement and computationally efficient at low frequency, when the modal density is relatively low.

The numerical model is designed specifically for this application and includes several novel formulations. Firstly, a new shell finite-element is derived to model the structural components typically used in building construction that have orthotropic characteristics such as plaster-wood walls, floors, and siding panels. The constitutive matrix for these types of components is formulated using simple analytical expressions based on the orthotropic constants of an equivalent orthotropic plate. This approach is computationally efficient since there is no need to model all the individual subcomponents of the assembly (studs, sheathing, etc.) and their interconnections. Secondly, a dedicated finite-element module is developed that implements the new shell element for orthotropic components as well as a conventional shell element for isotropic components, e.g. window panels and doors. The finite element module computes the "in vacuo" structural modes of vibration. The modes and external pressure distribution are then used to compute modal loads. This dedicated finite-element module has the main advantage of overcoming the need, and subsequent complications, for using a large commercial finite-element program. Lastly, a

novel formulation is developed for the fully coupled fluid-structure model to handle room openings and compute the acoustic response of interconnected rooms. The formulation is based on the Helmholtz resonator approach and is applicable to the very low frequency-range, when the acoustic wavelength is much larger than the opening dimensions.

Experimental validation of the numerical model and computer code is presented for three test cases of increasing complexity. The first test structure consists of a single plaster-wood wall backed by a rigid rectangular enclosure. The structure is excited by sonic booms generated with a speaker. The second test structure is a single room made of plaster-wood walls with two double-panel windows and a door. The third test structure consists of the first room to which a second room with a large window assembly was added. Several door configurations of the structure are tested to validate the formulation for room openings. This latter case is the most realistic one as it involves the interaction of several structural components with several interior cavities. For the last two test cases, sonic booms with realistic durations and amplitudes were generated using an explosive technique. Numerical predictions are compared to the experimental data for the three test cases and show a good overall agreement.

Finally, results from a parametric study are presented for the case of the single wall backed by a rigid enclosure. The effects of sonic-boom shape, e.g. rise time and duration, and effects of the structure geometry on the fluid-structure response to sonic booms are investigated.

Lorsqu'Iggy rencontra Donnie, la terre commença à trembler…

ACKNOWLEDGEMENTS

First, I would like to thank my advisor, Dr. Ricardo Burdisso, for giving me the opportunity to work on this exciting research topic. His guidance and untiring help throughout this journey were invaluable. It was through the challenges he set along the way that I could strengthen my knowledge in acoustics and vibration; through the independence he gave me that I could express my creativity; and through his patience and understanding that I could finish this dissertation. I am also grateful to Drs. Chris Fuller, Roop Mahajan, Marty Johnson, Georg Reichard, and Patricio Ravetta, for serving on my advisory committee and for their constructive comments throughout the course of this work.

I am indebted to the Institute for Critical Technology and Applied Science (ICTAS) and its director, Dr. Roop Mahajan, for the financial support provided throughout my entire Ph.D. qualifying period. Beyond the generous fellowship, ICTAS was an extraordinary place, giving me a chance to interact with other Doctoral Scholars, within a framework of interdisciplinary research.

The research was initiated and supported by the NASA Langley Research Center. The technical support from Jacob Klos and Brenda Sullivan, and their help to collect experimental data were deeply appreciated.

There are many friends in the Vibrations and Acoustics Laboratories (VAL) to whom I am grateful for the precious help and time they offered. Joseph Corcoran and Ryan Haac were responsible for the experimental effort of this research and none of the experimental validations would have been possible without the tremendous amount of work they devoted to setting up the experiments and acquiring data. I also wish to thank Leonardo Errasquin who helped me many times improving the code capabilities through his expertise in computer programming. Gail Coe deserves many thanks for her patience in the many administrative tasks she assisted me with. My compatriot and friend Tom-Davy Saux deserves most of the gratitude for bearing with me in the office for nearly three years, for all the constructive conversations during the long nights spent writing papers, and all the rest of course.

I would like to thank other friends from the French-speaking community for the times shared in Blacksburg or during trips throughout the United States. Among these friends are Guillaume Christin, Vincent Blandeau, Gregory Kleinhans, Sarah Gasser, Lise Vincent, Thomas Marquié, Hugo Blettery, Yannick Morel, and Mickaël Lallart.

I am also very grateful to some members of my family in France who, despite the distance and the time spent away from home, have continuously encouraged and supported me.

Last, I am thinking of Fate because dreams can indeed come true. Je t'aime Stephanie.

Table of Contents

List of Figures

List of Tables

1. Introduction

The development of a commercial supersonic aircraft is a technological challenge, by the nature of the environmental regulations and economic performance such an aircraft needs to meet. In the early 1960s, large research programs were initiated in the United States, Europe, and formerly U.S.S.R. for the design of a commercial supersonic aircraft. The Soviet Tupolev Tu-144 and Anglo-French Concorde have been the only two supersonic aircraft ever operated commercially, with their first commercial flights in 1975 and 1976, respectively. The Tupolev Tu-144 has only been operated in the U.S.S.R. for a relatively small number of flights. The Concorde remained in service for 27 years. However, the strength of the sonic booms and the effects on structures and populations on the flyover path prevented the Concorde to fly supersonic overland, limiting its service to mainly trans-Atlantic routes. The damage caused to the ozone layer by the fuel emissions layer was also a concern. In the United States, protests about noise resulted in the termination of the Supersonic Transport (SST) program in 1971. Several programs were then initiated such as the Supersonic Cruise Research (SCR) from 1971 to 1981 or High-Speed Research (HSR) from 1989 to 1999, with the prospects to develop the required technologies to overcome the environmental and fuel efficiency issues related to supersonic flights for commercial applications. Interest in supersonic transport has not declined since the last commercial flight of the Concorde in 2003. As an answer to the market demand, Japan and France are jointly researching since 2005 a new supersonic passenger plane to succeed to the Concorde, with up to 300 passenger seats and a flight speed of Mach 2. In the U.S., efforts are currently concentrated on smaller aircraft. Among them, a quiet design by Lockheed-Martin and Supersonic Aerospace

International (SAI) [1] could potentially meet regulations from the Federal Aviation Administration (FAA) and thus open a new era of supersonic transport. However, the ban on overland supersonic flight will only be lifted if the sonic booms at the ground level are acceptable from a human-perception point of view.

Most of the studies on sonic boom effects at the ground level were conducted in the 1960s and early 1970s. This includes the generation and propagation mechanisms of sonic booms from the aircraft to the ground, the transmission inside buildings, the structural response of buildings, ground reflection, diffraction, and interior noise levels. Although the different elements of the problem were studied separately, a more comprehensive work has not been reported that includes all the effects of sonic booms to ultimately predict the noise exposure inside realistic building structures, e.g. residential houses and office buildings. Thus far, these effects could only be investigated experimentally. Therefore, it would be desirable to have a computer-code package capable of predicting the vibro-acoustic response of realistic building structures exposed to sonic booms. Some potential users of this prediction tool could be the FAA and the aircraft designers, to supplement costly flight tests in the decision process about regulations on overland supersonic flights.

There are several aspects associated to the problem of interior noise due to sonic booms. A review of the current state of knowledge is presented.

1.1 Literature Review

1.1.1 Sonic Boom Generation, Propagation, and Evolution

The theory behind sonic boom generation, propagation, and evolution, was mostly established and validated by the early 1960s and implemented into practical models by the early 1970s. The sonic boom has been identified as the pressure signature close to the ground that is produced by the detached shock waves from a supersonic aircraft.

Figure 1.1 is a schematic description of the generation, propagation, and evolution of a sonic boom generated by an aircraft flying supersonic [2]. Several wavefronts and the signature at three distances are also depicted. The generation of shock waves, which corresponds to the near-field signature in the figure, is governed by the linearized supersonic flow theory [3] and computed from supersonic area rule methods [4-7]. The forward (fuselage nose, wing leading edge, cockpit canopy, and so forth) and rearward (rear fuselage, wing trailing edge, and so forth) facing elements of the aircraft are usually regions of positive and negative overpressures, respectively. The disturbance generated by the aircraft then propagates through the atmosphere. The theory behind propagation has been studied in the context of geometrical (or ray) acoustics [8,9]. Variations of the acoustic impedance and flow speed as the shock wave propagates from the aircraft to the ground results in the curvature of the rays. As the near-field signature propagates, its shape evolves. This phenomenon occurs because nonlinear effects accumulate over the long distance the shock wave travels. Higher pressure parts of the signature travel faster than ambient sound speed whereas lower pressure parts travel slower. Eventually, this results in the coalescence of the rays in the far-field into an N-wave. The theory

governing this physical phenomenon and the procedure to predict it was developed by Whitham [10,11].

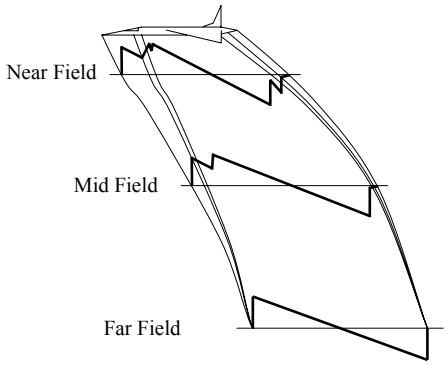

Figure 1.1: Sonic boom generation, propagation, and evolution [2] (fair use).

The pressure signature, $p_N(t)$, of a typical sonic boom is shown in Figure 1.2. The pressure profile is described by an N-wave of duration τ, with finite rise and fall times, and of maximum and minimum overpressures P_{t_1} and P_{t_2}, respectively. As the rise time increases, the high frequency content of the sonic boom is minimized and the boom noise will feel softer [12].

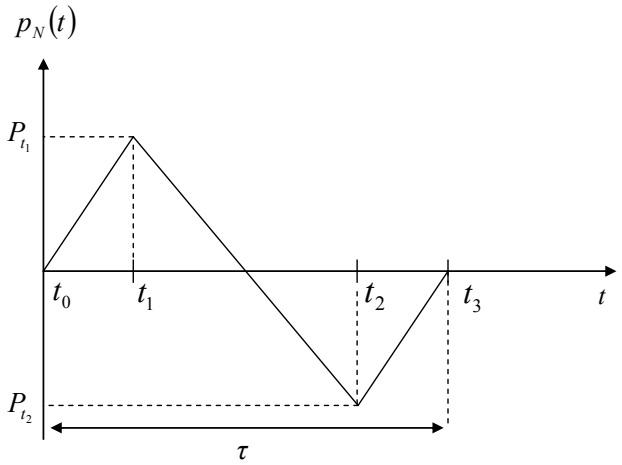

Figure 1.2: Time history of an ideal N-wave.

1.1.2 Designs for Sonic Boom Mitigation

Due to the strong interest in the commercialization of a Supersonic Business Jet (SBJ), many efforts have been devoted lately to the design of such an aircraft with reduced boom levels.

A preliminary design of a SBJ was carried out by Gulfstream [13] and is shown in Figure 1.3. The far-field pressure signature of the baseline aircraft, obtained from simulations, was a typical N-wave with a duration of 210 ms, maximum and minimum overpressures of 62.25 Pa (1.3 psf) and -52.67 Pa (-1.1 psf), respectively. Several parameters in the design were adjusted to reduce the overpressure levels of the baseline aircraft. Gulfstream's goal was to eventually design an aircraft that would produce a sonic boom with a maximum overpressure of 24 Pa (0.5 psf).

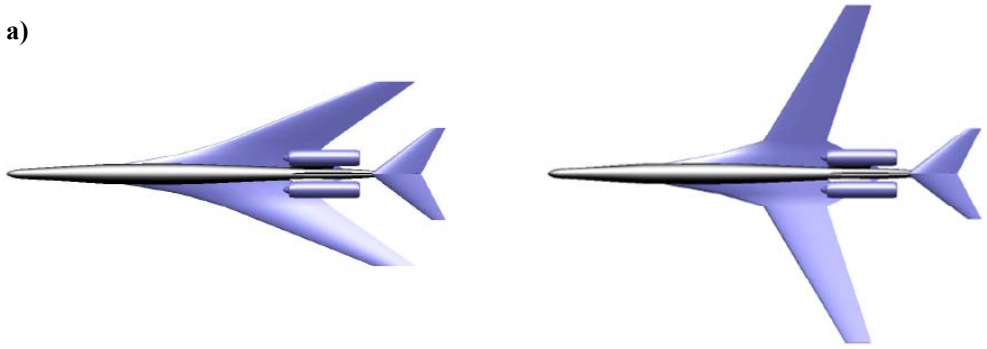

Figure 1.3: a) "Supersonic" and b) "Subsonic" baseline Gulfstream SBJ configurations [13] (fair use).

It was shown theoretically that sonic boom levels may be reduced through shaping by tailoring the area and lift (equivalent area) [14-16]. This concept was recently verified

experimentally through flight tests [17,18]. Figure 1.4 shows the aircraft used in the flight tests, an F-5 and an F-5 with a modified nose. Modification of the aircraft nose geometry resulted in a significant attenuation of the first overpressure peak of the sonic boom and thus demonstrated the validity of the concept. Gulfstream Aerospace flight-tested an F-15B whose nose was equipped with a telescoping spike [19,20], as shown in Figure 1.5. The spike was about 10-m long and was in three segments of different diameters. The purpose of this nose extension was to break the strong shock generated by the nose of the aircraft into a series of weaker shocks. The geometry of the spike was tuned so that the weaker shock waves would not coalesce into an N-wave as they reach the ground. This was achieved by looking at the relative position of the shocks and the coalescence rate. Recently, Lockheed Martin jointly with Supersonic Aerospace International (SAI) proposed the design of an SBJ [1] that would potentially meet FAA regulations and allow overland supersonic flight, thus opening a new era of supersonic transport. The aircraft, shown in Figure 1.6, would carry from 8 to 10 passengers, would fly at a cruise speed of Mach 1.6 to 1.8, and would generate sonic booms at the ground with one-hundredth the strength of Concorde's.

Figure 1.4: The baseline F-5E and modified F-5 SSBD aircraft [17] (fair use).

Figure 1.5: Photograph of an F-15B in flight with quiet spike attached [21] (fair use).

Figure 1.6: Quiet Supersonic Transport in development by Lockheed Martin and Supersonic Aerospace Institute [1] (fair use).

1.1.3 Experimental Sonic-Boom Simulation

Currently, experimental tests are the only means by which the effects of sonic booms inside residential buildings may be assessed. Typically, fighter jets are used to generate sonic booms and excite a structure that is appropriately instrumented to record its vibro-acoustic response [22,23]. However, the resources required to fuel and maneuver a supersonic aircraft are prohibitively expensive. In addition, there is a degree of control lost to the realm of far-field outdoor acoustics. For instance, atmospheric effects along the propagation path, such as wind, temperature gradients, and humidity are unavoidable

over such a long distance. As a result of these limitations, there has been some interest in the feasibility and accuracy of using sonic-boom simulators.

Horn-type simulators consist of a large pyramidal [24,25] or exponential horn [26] connected to a device capable of releasing a sudden gas discharge that creates the traveling shock wave. Horn-type simulators create the sonic boom waveform as a traveling wave but are unable to reproduce the lowest frequency content of a real sonic boom. Explosive techniques have also been used to simulate sonic booms. These techniques are particularly suited to large-scale outdoor testing and allow for a wide range of shock-wave shapes to be reproduced. One explosive technique consists of multiple explosive line charges arranged appropriately to produce desired shock-wave pressure signatures [27,28]. The length of the line determines the duration of the signal; the charge strength and distance to the observer determine the peak overpressure. Another explosive technique uses a sausage-shaped balloon containing oxygen and methane with a line charge through the center of the balloon [29]. Small chambers equipped with arrays of loudspeakers have been used extensively in studies of human response to impulsive noises, including sonic booms [12,30-32]. Arrays of speakers have also been used for structural forcing [33]. With appropriate frequency and phase compensation, those devices are capable of producing a wide range of overpressures, rise times, and stimuli durations. Speakers have the advantage of reproducing many pressure signatures without the experimental efforts required from other sonic boom simulators such as explosives or horns. However, such systems may fall short of overpressure amplitude.

1.1.4 Structural Response Due to Sonic Booms

The dynamic response of plates under sonic boom excitation has been mostly investigated using modal decomposition methods [34]. An analytical solution to the vibration problem of a plate excited by a traveling N-wave was found by Cheng and Benveniste [35]. The analysis was simplified to predict the fundamental mode of vibration of the plate. Crocker [36] solved the problem for an ideal (rise and fall times equal to zero) N-wave, traveling across the plate and normal to the plate. The analysis was later extended to arbitrary plate geometries using the isoamplitude contour lines method in conjunction with modal decomposition [37,38].

Craggs [39] proposed a numerical model for the response of a rectangular plate excited by an N-wave arriving at oblique incidence. For the case presented, it was shown that the orientation of the incident wave has a significant effect on the plate response. The asymmetric modes, which do not make any contribution when the wave is at normal incidence, are excited by a convection term in the generalized forces when the wave is at oblique incidence.

Popplewell [40,41] investigated the response of a building exposed to N-wave excitation using a finite-element displacement method. A simple box-type structure was used as a model for a single-story dwelling building. The model was based on several assumptions. The box structure was to be made of rectangular homogeneous isotropic plates with the base edges either fixed or simply supported. Stretching of the middle

surface of the constituent plates was neglected. The common edges were free to rotate so that the adjacent edges of plates remain at right angles but do not move in translation. Thus, corner deflections were not permitted, and they were also assumed not allowed to twist. The effect of the air enclosed within the box was neglected. Satisfying these assumptions permitted the three-dimensional box to be treated as an assemblage of two-dimensional plates with additional box constraints. The natural frequencies and normal modes were computed.

The assumption that the walls are made of isotropic and homogeneous materials is not always valid because of typical conventional construction methods, such as houses built of composite walls, e.g. plaster-wood walls. Then, in-plane stretching of the middle surface of the plate cannot be neglected. The dynamic response of a plaster-wood wall, of the type commonly seen in residential constructions, was first predicted by Wahba assuming a series solution of the displacement along with Lagrange equations [42,43]. The dynamics of the plaster-wood wall was also investigated using finite elements (consistent- and lumped-mass formulations) to obtain solutions for arbitrary wall geometries [44].

1.1.5 Fluid-Structure Coupling

An important aspect of interior noise analysis is the coupling between the fluid and the structure. Pretlove derived an analytical expression for the free structural response of a panel backed by a closed cavity [45]. The structural displacement was represented by a series of the “in vacuo” normal modes of a rectangular plate with simply-supported

boundary conditions. The pressure was an exact solution of the acoustic wave equation for a rectangular room with one flexible wall and the other walls being perfect acoustic reflectors. Coupling between the panel and the cavity was expressed by matching the particle velocity at the flexible wall with the motion of the plate, and by taking advantage of the orthogonality of the modes. It was shown that for a panel with a larger stiffness than the cavity, the acoustic field inside the cavity may be calculated directly from the "in vacuo" vibration of the panel (fluid-structure coupling may be ignored). On the other hand, if the stiffness of the cavity is of the same order as or larger than the one of the panel, coupling occurs. The system acts then like a Helmholtz resonator when the panel vibrates in its fundamental mode. The panel is then similar to a mass connected to a spring-like cavity. The approach was later extended to predict the structural response of the panel excited by a random pressure loading [46]. The problem was solved in the frequency domain by taking the Fourier transform of the structural dynamic equation. Finally, this approach was simplified by Pretlove and Craggs [47] to predict the fundamental mode of the coupled system. The dynamics of such systems was also studied by Craggs [48] using finite elements for the structural motion and the volume-displacement theory for the acoustic system. In this approach, the effect of the cavity was introduced in the structural dynamic equations as an extra stiffness matrix term that coupled the degrees of freedom. The problem was also solved using finite elements for both the plate and the acoustic systems [49], allowing thus for systems with arbitrary geometries and boundary conditions to be studied.

Fahy [50] proposed a very general model (modal-interaction model) for the transmission of an arbitrary wave through a plate backed by a cavity. In the dynamic equations of the system, the plate displacement is expressed in terms of summations over the "in vacuo" normal modes of vibration, and the interior pressure in terms of summations over the acoustic modes of the cavity with perfectly reflecting surfaces (hard walls). Then, using the orthogonality properties of the modes, two finite sets of ordinary differential equations (modal equations) are obtained, describing the modal displacement of the plate and the modal pressure inside the cavity. The response of the fluid-structure system is obtained by simultaneously integrating the two sets of equations. The modal approach is well suited to this problem as most of the acoustic energy of a typical sonic boom is contained in the very low frequency range and thus a relatively small number of structural and acoustic modes need to be considered.

1.1.6 Transmission of a Sonic Boom through an Opening

The transmission of a sonic boom inside a room with an open window was first studied by Vaidya [51,52]. The initial transient response of the room occurs in a "multiple-reflection" stage and was shown to be the most important from a subjective point a view. To describe this part of the response, the room was viewed as a duct terminated by an end wall. The pressure field inside the room was viewed as the components of two fields, which together satisfy the relevant boundary condition on the end wall. The solution was carried out in the frequency domain. The inverse Fourier transform was then used to obtain the response in the time domain. During the later part of the response, the sound field inside the room becomes rather diffuse. This part of the

response is of primary interest from the structural point of view. The room is represented by a lumped acoustic element. Therefore, the Helmholtz resonator approach was used to compute the sound field. Lin [53] presented an electrical analogy of the Helmholtz resonator approach. Results were in good agreement with those obtained by Vaidya [51,52]. Both authors (Vaidya and Lin) used an arbitrary constant to describe the system-damping. Wahba et al. [54] refined the Helmholtz approach by expressing the system-damping in terms of known parameters. The Helmholtz approach was also used by Hubbard and Shepherd [55] to study the behavior of rigid rooms interconnected with openings. The Helmholtz resonances computed by their model were compared with experimental data for various structures and showed to be in good agreement.

1.2 Objectives

The literature review indicates that a significant amount of work has been devoted to studying the vibration of various structures exposed to sonic booms and the resulting interior acoustic response. However, most studies were limited to the cases of simple structures, e.g. rectangular plates, and often did not account for the fluid-structure coupling, which has significant effects on the system response at low frequency. Some authors have tackled more realistic cases, e.g. box-type structure [40,41] and plaster-wood wall [42-44], but in these studies the acoustic part of the problem was ignored (only the structure response was studied).

The motivation behind the work presented in this dissertation is the need for a numerical tool to supplement costly flight tests in assessing the noise impact of sonic

booms at the ground level, in particular the human exposure inside residential buildings. As a further step in the development of this tool, the first objective of this work is to improve on past research by proposing a numerical formulation and a computer code capable of predicting the vibro-acoustic response of simplified but realistic building structures exposed to sonic booms, at low frequency. The formulation should be computationally efficient and easy to implement. In that sense, the direct application of numerical techniques, e.g. finite element method, for both the structure vibration and interior acoustics would not be realistic and should be avoided. Also, fluid-structure coupling should be accounted for in the modeling effort. Finally, the formulation should include the capability to analyze structures with multiple rooms that are fully separated by structural components (isolated rooms) or that include openings, interconnecting them and to the outside. For many of these tasks to be integrated within a single numerical tool, the formulation that is to be developed has to be novel.

The second objective of this work is to gradually validate the numerical formulation and computer code experimentally. Therefore, structures of increasing complexity should be built, extensively instrumented to record their responses, and exposed to sonic booms. The necessary techniques to generate sonic booms, and to acquire and post-process data should also be developed.

The third objective is to use the validated computer code to carry out parametric studies and thus to better understand the transmission mechanisms of sonic booms inside building structures.

1.3 Organization

The dissertation is organized in four chapters and two appendices as follows. Chapter 1 presents a literature review on the various aspects of the problem of interior noise due to sonic booms. In this section, the objectives of this study are also listed. Chapter 2 presents the numerical formulation of the problem. This includes: the problem description and solution approach; a structural-acoustic model to compute the vibro-acoustic response of a building structure; a new shell element to model most components of a typical building structure and a finite-element model to compute its normal modes; the expressions for the acoustic modes of isolated rooms; the modeling of room openings and interconnected rooms; and the computer code to carry out the numerical simulations. Chapter 3 presents the experimental validation of the model for three tests cases of increasing complexity: a single wall, a single room, and a structure with two rooms and two attics. The validation of the formulation for room openings and interconnected rooms is also included in this chapter. Chapter 4 presents a parametric study on the effects of sonic-boom shape and structure geometry on the response to sonic booms. Chapter 5 recalls the important conclusions of the study and outlines a number of recommendations for future work. Appendix A is a description of the Newmark-β algorithm for the numerical integration of dynamic equations. Appendix B presents the detailed formulation of the shell finite element.

2. Numerical Formulation

This section presents the theoretical steps involved in the development of a numerical model for predicting the transmission of sonic booms into buildings at low frequency. The formulation is directly applicable to realistic building structures, such as wood-type residential houses, box stores, or office buildings, exposed to an arbitrary pressure loading, including sonic booms. Given the geometry and properties of the structure and given the external pressure loading, the model is capable of predicting the vibration of the structure and the interior acoustic response. The dynamics of the fluid-structure system, including their fully-coupled interaction, is computed in the time domain using a modal-decomposition approach similar to the one proposed by Fahy [50].

2.1 Problem Description

Figure 2.1 is a schematic description of the problem. A building structure with an arbitrary geometry is exposed to an incident sonic boom with an arbitrary time history. The interaction of the sonic boom with the external surfaces of the structure produces a traveling wave over these surfaces (pressure loading function). The travelling wave results from three pressure fields: the doubling of the pressure due to the reflected wave, the radiated field due to the vibration of the structure, and that due to diffraction of the incident wave on the structure. As a result of the pressure loading, the structure vibrates (structure response) and radiates sound into the enclosures (room acoustics). The pressure fluctuation inside the enclosures creates an additional pressure loading on the structure that causes the fluid-structure system to be fully coupled.

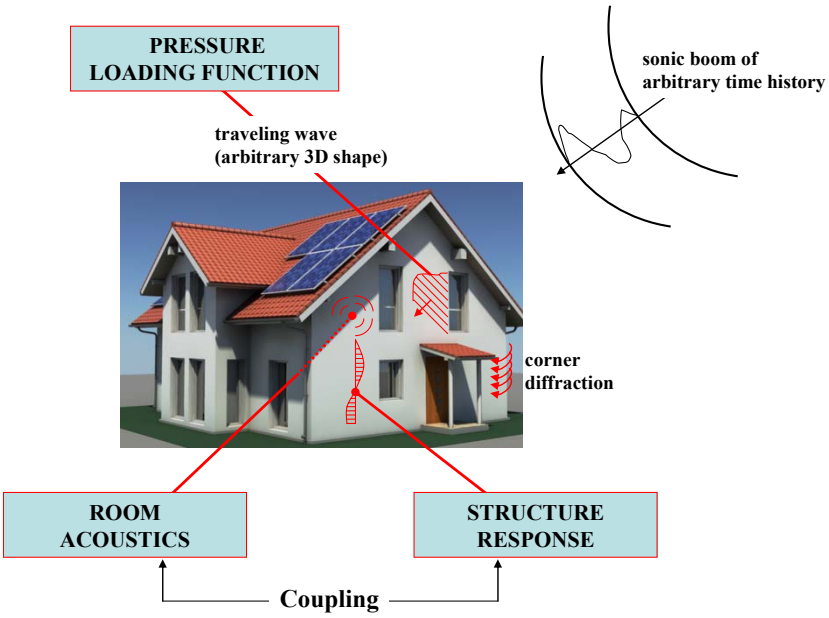

Figure 2.1: Problem description of a structure subjected to an exterior pressure excitation.

The numerical formulation is carried out for the most general case of a structure with an arbitrary shape enclosing a number, N_V, of volumes. An example of such a structure in its global coordinate system (x,y,z) is shown in Figure 2.2. The structure is composed of the external surfaces S_i^E (blue surfaces) that are exposed to an external pressure loading p_{ext} and that enclose the volumes V_i (the union of these surfaces form the surface S^E) and the interior surfaces S_{ij}^I (red surfaces) that separate volumes V_i and V_j. Witness that cavities interconnected with an opening (e.g. volumes V_2 and V_3) truly form one volume. However, it is convenient to consider these cavities as two separate volumes for reasons that will become apparent later in the problem formulation. The following convention about the orientation of the surfaces is adopted, external surfaces have their normal

pointing outward and interior surfaces have their normal pointing to the positive axes directions of the global coordinate system (x,y,z).

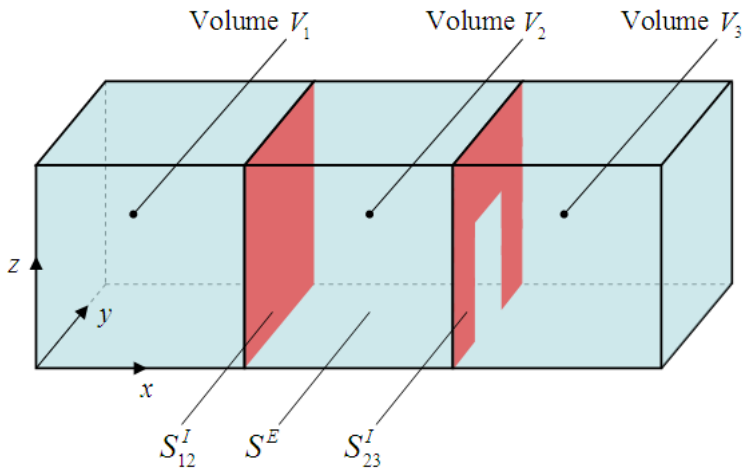

Figure 2.2: Schematic description of a structure enclosing three rooms.

2.2 Solution Approach

The formulation of the model is carried out in the time domain using a modal-decomposition approach. In the dynamic equations of motion of a given fluid-structure system, the structural displacement is expressed in terms of summations over the "in vacuo" modes of vibration. The pressures inside the interior volumes are expressed as summations over the acoustic modes of rooms with perfectly reflecting surfaces. The structural modes are computed numerically using the finite-element method. A shell element was specifically derived to model the structural components of typical residential buildings, e.g. plaster-wood walls, windows, and doors. Another structural element was derived to model openings interconnecting rooms or to the outside. The acoustic modes are computed for rectangular geometries using analytical expressions.

Using the orthogonality properties of the structural and acoustic modes, the dynamics of a given fluid-structure system is formulated by two finite sets of ordinary differential equations (modal equations). These equations are then integrated numerically to solve for the vibro-acoustic response of the system. The system response is also predicted in the frequency domain, by taking the Fourier transform of the time-domain response.

2.3 Structural-Acoustic Model

The structure response is governed by one dynamic equation that includes source terms corresponding to the external pressure loading and to the pressure fluctuation inside the enclosed volumes (coupling term). The acoustic response inside each volume is governed by the acoustic wave equation (N_v is the total number of acoustic equations) with source terms corresponding to the structure vibration.

The normal component, *w,* of the structural displacement is expressed in terms of summations over the "in vacuo" normal modes of vibration as,

$$w(x_s, y_s, t) \approx \sum_{n=1}^{N_s} q_n(t)\phi_n(x_s, y_s) \tag{2.1}$$

where N_s is the number of modes included in the expansion, $q_n(t)$ is the modal displacement, and $\phi_n(x_s, y_s)$ are the mode shapes of the structure.

Inside each volume V_i, the pressure p^{V_i} is expressed in terms of summations over the acoustic modes of the rooms with perfectly reflecting surfaces (hard walls),

$$p^{V_i}(x,y,z,t) \approx \sum_{m=0}^{N_a^i} a_m^{V_i}(t)\psi_m^{V_i}(x,y,z) \tag{2.2}$$

where N_a^i is the number of modes included in the expansion, $a_m^{V_i}(t)$ is the modal pressure, and $\psi_m^{V_i}$ are the acoustic mode shapes of volume V_i.

The expressions for the structural displacement w and interior pressures p^{V_i} given in Equations (2.1) and (2.2) are substituted into the dynamic equations of the fluid-structure system. The orthogonality properties of the modes are then used to reduce the dynamic equations to a finite set of ordinary differential equations. The two orthogonality conditions for the structural modes are expressed here as,

$$\iint_S \phi_{n'}(x_s,y_s) m_s \phi_n(x_s,y_s) ds = \delta_{nn'} \tag{2.3}$$

$$\iint_S \phi_{n'}(x_s,y_s) D\nabla^4[\phi_n(x_s,y_s)] ds = \omega_n^2 \delta_{nn'} \tag{2.4}$$

where m_s is the mass per unit area of the structure and ω_n is the n^{th} angular natural frequency. Similarly, the two orthogonality conditions for the acoustic modes are expressed here as,

$$\iiint_V \psi_m(x,y,z)\psi_{m'}(x,y,z) dv = \delta_{mm'} V_i \tag{2.5}$$

$$\iiint_V \psi_{m'}(x,y,z)\nabla^2[\psi_m(x,y,z)] dv = -\left(k_m^{V_i}\right)^2 \delta_{mm'} V_i \tag{2.6}$$

where $k_m^{V_i}$ is the wavenumber of the m^{th} acoustic mode of volume V_i. Note that the wavenumber relates to the angular natural frequency as $k_m^{V_i} = \omega_m^{V_i}/c$, where c is the speed of sound in the fluid.

For the structure, one finite set of modal equations is obtained as,

$$\begin{aligned}(\omega_n)^2 q_n + 2\xi_n \omega_n \dot{q}_n + \ddot{q}_n &= \int_{S^E} p_{ext}\phi_n ds + \rho_r \sum_m \sum_i \dot{\Phi}_m^{V_i} \int_{S_i^E} \phi_n \psi_m ds \\ &+ \rho_r \sum_m \left[\sum_{i,j} \left(\dot{\Phi}_m^{V_i} \int_{S_{ij}^I} sign.\phi_n \psi_m^{V_i} ds + \dot{\Phi}_m^{V_j} \int_{S_{ij}^I} sign.\phi_n \psi_m^{V_j} ds \right) \right]\end{aligned} \tag{2.7}$$

where ρ_r is the mass density of the fluid, ξ_n the modal damping ratios, $\Phi_m^{V_i}$ is the modal velocity potential, q_n is the modal displacement of the structure, j is an index referring to the volumes V_j adjacent to volume V_i, and *sign* is equal to -1 (or 1) if the normal to the surface of integration points inward (or outward) with respect to the volume considered in the integrand.

The above set of modal equations has two source terms (right hand side of the equation), the action of the external pressure loading on the external surfaces (first integral), and the action of the interior pressures on the structure (coupling term), which is separated into external surfaces S^E (second integral) and internal surfaces S^I (last two integrals).

For each volume V_i, a set of acoustic modal equations is formulated as,

$$\left(\omega_m^{V_i}\right)^2 \Phi_m^{V_i} + 2\xi_m^{V_i} \omega_m^{V_i} \dot{\Phi}_m^{V_i} + \ddot{\Phi}_m^{V_i} = -\frac{2c^2}{V_i} \left[\sum_n \dot{q}_n \left(\int_{S_i^E} \psi_m^{V_i} \phi_n ds + \sum_j \int_{S_{ij}^I} sign.\psi_m^{V_i} \phi_n ds \right) \right] \tag{2.8}$$

where $\xi_m^{V_i}$ are the acoustic modal damping ratios.

The above set of equations has one source term, separated into the vibration of the external surfaces (first integral) and internal surfaces (second integral).

The set of structural modal equations and the N_v sets of acoustic modal equations are recombined into one set as,

$$\begin{bmatrix} [\Omega^s_{nn}] & [0] & \cdots & [0] \\ [0] & [\Omega^{V_1}_{mm}] & \ddots & \vdots \\ \vdots & \ddots & \ddots & [0] \\ [0] & \cdots & [0] & [\Omega^{V_{N_v}}_{mm}] \end{bmatrix} \begin{Bmatrix} \{q_n\} \\ \{\Phi^{V_1}_m\} \\ \vdots \\ \{\Phi^{V_{N_v}}_m\} \end{Bmatrix} + \begin{bmatrix} [D^s_{nn}] & [0] & \cdots & [0] \\ [0] & [D^{V_1}_{mm}] & \ddots & \vdots \\ \vdots & \ddots & \ddots & [0] \\ [0] & \cdots & [0] & [D^{V_{N_v}}_{mm}] \end{bmatrix} \begin{Bmatrix} \{\dot{q}_n\} \\ \{\dot{\Phi}^{V_1}_m\} \\ \vdots \\ \{\dot{\Phi}^{V_{N_v}}_m\} \end{Bmatrix}$$
$$+ \begin{bmatrix} [I^s_{nn}] & [0] & \cdots & [0] \\ [0] & [I_{mm}] & \ddots & \vdots \\ \vdots & \ddots & \ddots & [0] \\ [0] & \cdots & [0] & [I_{mm}] \end{bmatrix} \begin{Bmatrix} \{\ddot{q}_n\} \\ \{\ddot{\Phi}^{V_1}_m\} \\ \vdots \\ \{\ddot{\Phi}^{V_{N_v}}_m\} \end{Bmatrix}$$
$$+ \begin{bmatrix} & [0] & & & & -\rho_r\left(\left[C^{V_i/S^E_i}_{mn}\right]^T + \left[C^{V_i/S^I_{ij}}_{mn}\right]^T + \left[C^{V_j/S^I_{ij}}_{mn}\right]^T\right) \\ & & [0] & & & [0] \\ & & [0] & \ddots & & [0] \\ \frac{2c^2}{V_i}\left(\left[C^{V_i/S^E_i}_{mn}\right] + \left[C^{V_i/S^I_{ij}}_{mn}\right]\right) & & [0] & [0] & & [0] \end{bmatrix} \begin{Bmatrix} \{\dot{q}_n\} \\ \{\dot{\Phi}^{V_1}_m\} \\ \vdots \\ \{\dot{\Phi}^{V_{N_v}}_m\} \end{Bmatrix}$$
$$= \begin{Bmatrix} \{F_n(t)\} \\ \{0\} \\ \vdots \\ \{0\} \end{Bmatrix} \tag{2.9}$$

which can be rewritten in compact form as,

$$\mathbf{I}\ddot{\mathbf{u}}_t + \mathbf{C}\dot{\mathbf{u}}_t + \mathbf{K}\mathbf{u}_t = \mathbf{F}_t \tag{2.10}$$

where bold indicates matrices and vectors.

Finally, the above set of modal equations is numerically integrated to simultaneously solve for the modal structural displacement and modal velocity potentials in the time domain. The Newmark-β integration scheme was used for this purpose [56]. A detailed derivation of the Newmark-β algorithm may be found in Appendix A. Modal summation

is then used to obtain the vibro-acoustic response of the system in the physical domain. The vibro-acoustic response of the system is also predicted in the frequency domain by taking the Fourier transform of the time-domain response.

The formulation presented above was primarily derived to model isolated rooms, i.e. rooms that are not interconnected with openings. In this formulation, it is assumed that the mass and stiffness properties of the fluid-structure system are not dependent on frequency. Therefore, a time-domain solver can be used to integrate the dynamic equations of the system. The same formulation will be used to handle structures with openings at very low-frequency, where an opening can be modeled as the mass element of a Helmholtz-resonator system. However, in a transition frequency-region, where the Helmholtz approach does no longer hold, a frequency-domain solver should be used since the opening properties are frequency dependent. The frequency-domain solver was not implemented in this research but its formulation is presented in Section 2.6, as a recommendation for future work.

2.4 A New Finite Element to Model Building Components with Orthotropic Characteristics

The structural-acoustic model requires knowledge of the structural modal properties, i.e. natural frequencies, mode shapes, and modal damping ratios. The natural frequencies and mode shapes are determined from solving an eigenvalue problem. On the other hand, the damping ratios were estimated from modal testing and analysis. Because of the complexity of the structures targeted in this study, the eigenvalue problem must be solved numerically. The finite element approach was chosen to solve this eigenvalue problem.

Typical residential houses in the United States are primarily made of wooden framed walls that have orthotropic characteristics such as plaster-wood walls, floors, and ceilings. To model the free vibration of such walls, one could be tempted to use a commercial finite-element package to create a three-dimensional mesh of the walls and model all the wall subcomponents such as the studs and the sheathing, as shown in Figure 2.3. This approach is not practical for a number of reasons: i) Too many elements are required to discretize a structure in such a detailed fashion; ii) the type of connections between the subcomponents is not known, iii) modeling walls as 3-D components adds complexity to the modeling of the fluid-structure interaction by increasing the number of surfaces in the structure that interact with the interior fluid field. Besides, point iii) would make the task of modeling room openings very challenging.

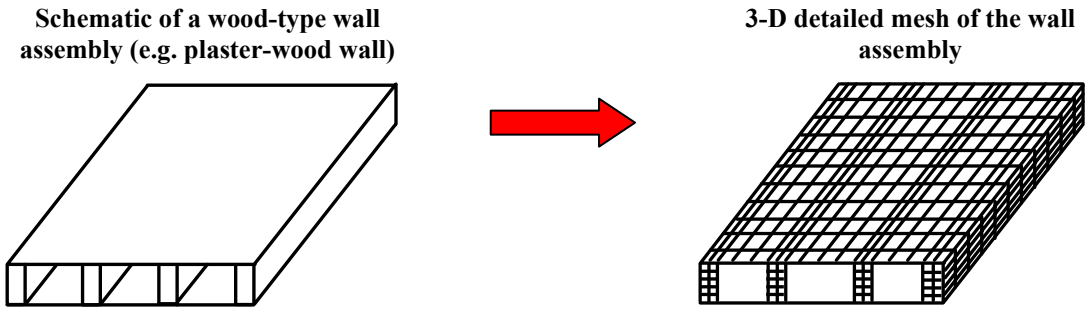

Figure 2.3: Schematic of a wood-type wall assembly modeled with a detailed finite element approach.

Wahba [44] recognized these points and proposed a finite-element model for the free and forced dynamic responses of a plaster-wood wall based on two-dimensional finite elements. The wall was discretized into eight-noded, parabolic, isoparametric, quadrilateral elements. The element stiffness matrix was determined from the expression

of strain energy. The element mass matrix was determined using both consistent- and lumped-mass (diagonal matrix) formulations.

In this research, an innovative approach was implemented that differs from that proposed by Wahba [44] in several aspects. A specific finite element targeted to the modeling of most structural components forming a building structure was derived. The novelty of the approach followed in this study is to consider a wall assembly (e.g. studs, plaster, and OSB boards) as a uniform orthotropic material. The orthotropic constants of the material can be determined using simple analytical expressions based on the theory of stiffened plates. The main theoretical steps of this formulation are presented in this section. A full derivation of the mass and stiffness matrices for this finite element is found in Appendix B.

In a structure with a three-dimensional geometry, both the in- and out-of-plane motions of a component, e.g. wall, couple with the other structural components, which are not necessarily in the same plane. Therefore, it is necessary to model the structural components as shell elements. To this end, four-node rectangular shell-elements were used to model the structure. The two-dimensional shell element models three-dimensional structural components such as walls, windows, and doors, at their mid-planes. A shell element is obtained by combining a plate bending element and a plane-stress element. As indicated in Figure 2.4, a plane-stress element has two in-plane displacements per node. On the other hand, a plate-bending element has a transverse

deflection and two bending rotations per node. All together, a shell has five degrees of freedom per node, three displacements and two rotations.

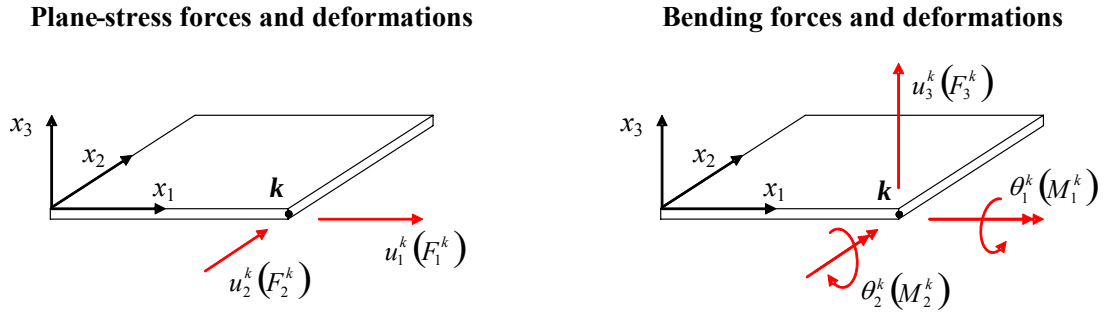

Figure 2.4: Shell as a combination of plate bending element and plane stress element.

The formulation of the element mass matrix is based on a lumping scheme. The mass of an element is distributed evenly between the four element nodes. The novelty of the shell element developed in this study lies in the formulation of the element stiffness matrix. Figure 2.5 is a diagram showing the formulation of these matrices for building components with isotropic and orthotropic characteristics. The element stiffness matrix $[K^e]$ is computed from the following expression,

$$[K^e] = \int_{\Omega^e} [B]^T [D][B] d\Omega^e \tag{2.11}$$

where $[D]$ is the constitutive matrix of the element material and $[B]$ is a matrix relating the nodal displacements to the strain field. The numerical scheme to carry out the integration in Equation (2.11) over the element surface is found in Appendix B. Note that the element stiffness matrix is a 20×20-component matrix because each of the element nodes has 5 degrees of freedom. However, for the purpose of assembling the element matrix into the system matrix, the "drilling" degree of freedom (rotation along the normal

to the element surface) is taken into account in the formulation. Therefore, the element stiffness matrix is a 24×24-component matrix.

The constitutive matrix is divided into membrane $[D_m]$, bending $[D_b]$, and shear $[D_s]$ components. For an isotropic material, e.g. windows and doors, the formulation of the constitutive matrix is trivial as it depends solely on the material properties, e.g. Young's modulus and Poisson ratio. The expression of the constitutive matrix for an isotropic material is given by Equation (B.24). Based on this expression for an isotropic material, an approximated expression of the constitutive matrix for an orthotropic material was derived in this research in terms of its orthotropic constants D_x and D_y as,

$$[D_m] = h\begin{bmatrix} 12D_x/h^3 & 12D_x/(\nu h^3) & 0 \\ 12D_x/(\nu h^3) & 12D_y/h^3 & 0 \\ 0 & 0 & 12G/h^3 \end{bmatrix} \tag{2.12}$$

$$[D_b] = \frac{h^2}{12}[D_m] \tag{2.13}$$

$$[D_s] = \frac{12G}{S_f h^2}\begin{bmatrix} 1 & 0 \\ 0 & 1 \end{bmatrix} \tag{2.14}$$

where h is the thickness of the material, S_f is the shear factor (S_f = 6/5, assuming a parabolic variation along the thickness), and G is the shear modulus averaged for all wall materials.

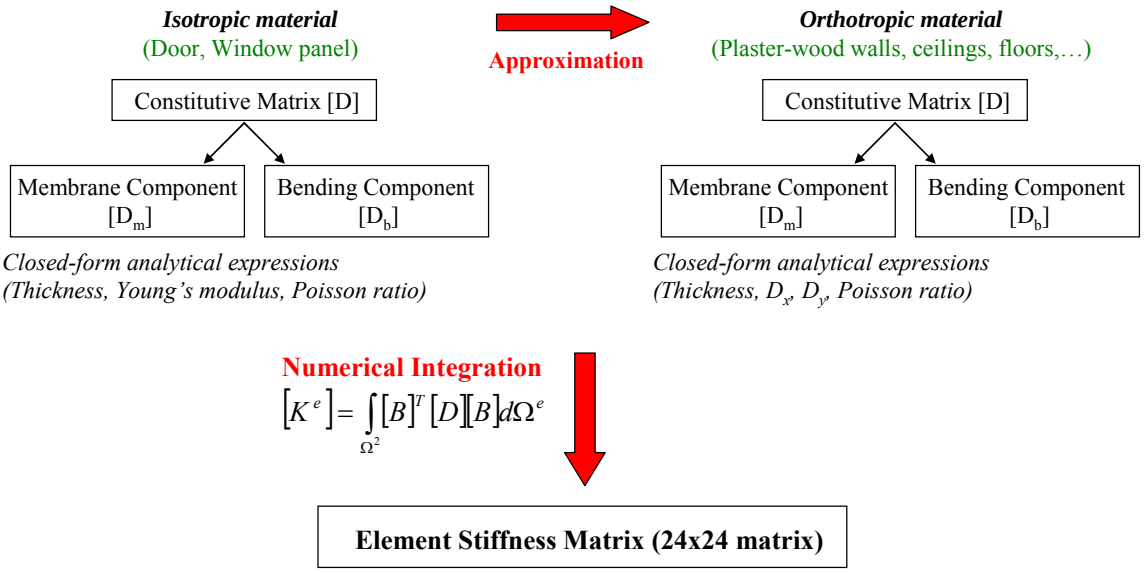

Figure 2.5: Formulation of the element stiffness matrix.

A typical wooden framed wall consists of an assembly of studs arranged vertically and sandwiched between plaster and/or wood boards. Rather than modeling all the subcomponents of the wall, e.g. studs, wood and plaster boards, the Timoshenko-Woinowsky-Krieger theory of stiffened plates [58] is used to approximate the wall as a uniform orthotropic plate with orthotropic constants D_x and D_y. The Timoshenko-Woinowsky-Krieger method has some limitations, many of which are violated by the geometry of a typical wall assembly. However, due to its simplicity, the method was adapted to our application by making some approximations. The wall is discretized into a series of T-beams, as shown in Figure 2.6, instead of I-beams in the actual geometry. The orthotropic constants are then estimated for a single T-beam using the following expressions,

$$D_x = \frac{E a_1 h_p^{\,3}}{12\left(a_1 - h_r + \alpha^3 h_r\right)} \tag{2.15}$$

$$D_y = \frac{EI}{a_1} \tag{2.16}$$

where α is the ratio of the plate thickness alone (h_p) to the total thickness (h), E is the Young's modulus averaged for all wall materials, a_1 is the average spacing between the ribs, h_r is the thickness of the rib, and I is the moment of inertia of a single T-beam.

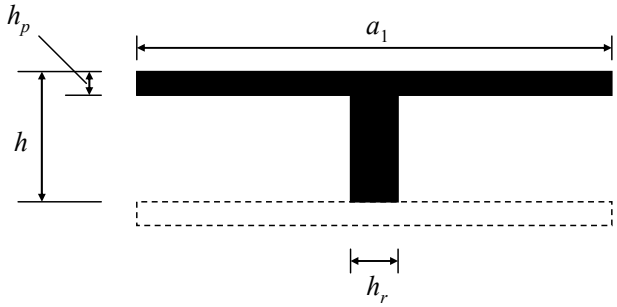

Figure 2.6: Cross-section geometry of a wall segment used to determine equivalent orthotropic plate properties. The dashed portion indicates geometry of the wall that exists physically but was not taken into account in determining geometric properties for the equivalent plate due to limitations of the method used.

The resulting constitutive matrix for a plaster-wood wall then becomes a simple analytical expression based on the orthotropic constants of an equivalent orthotropic plate. This approach includes several advantages. Firstly, this method is very simple and effective to implement computationally since it only requires two orthotropic constants and the mass surface density to model the dynamics of the wall. Secondly, there is no need to model all the individual subcomponents of the assembly (studs, OSB, drywall, etc.) and their interconnection, which would result in solving a complex 3D problem.

It is important to insure that the number of finite elements is sufficient to avoid spatial aliasing. Typically, this condition is satisfied if at least four elements are included in the smallest bending wavelength for the linear elements used in this model. The approach

used to insure that the mesh size is adequate consists in comparing the smallest bending wavelength of the structure at a given frequency to the size of the finite elements. The smallest bending wavelength of the structure is approximated by that of an infinite thin plate given by,

$$\lambda_b = 2\pi\left(\frac{D}{\omega^2 m_s}\right)^{\frac{1}{4}} \tag{2.17}$$

where D is the bending stiffness of the plate taken as the smallest orthotropic constant of the walls forming the structure. This approximate criterion has the advantage of assessing the adequacy of the finite-element mesh before running the finite-element model.

2.5 Acoustic Modal Properties of Isolated Rectangular Rooms

The eigenproperties of a room are obtained by solving the homogeneous wave equation with the appropriate boundary conditions,

$$\nabla^2 p(x,y,z,t) - \frac{1}{c^2}\frac{\partial^2 p(x,y,z,t)}{\partial t^2} = 0 \tag{2.18}$$

In this study, only rectangular room geometries are considered as this is the most common type encountered. In the structural-acoustic model, it is assumed that the surfaces of the room are perfect acoustic reflectors, i.e. hard walls. Under these assumptions, the natural frequencies and mode shapes can be expressed analytically as [59],

$$f_m = \frac{c}{\pi}\sqrt{\left(\frac{m_x}{L_{rx}}\right)^2 + \left(\frac{m_y}{L_{ry}}\right)^2 + \left(\frac{m_z}{L_{rz}}\right)^2}\ ,\ m \to (m_x, m_y, m_z) \tag{2.19}$$

$$\psi_m(x,y,z) = R_{(m_x,m_y,m_z)} \cos\left(\frac{m_x\pi}{L_{rx}}x\right)\cos\left(\frac{m_y\pi}{L_{ry}}y\right)\cos\left(\frac{m_z\pi}{L_{rz}}z\right),\ m \to (m_x,m_y,m_z) \qquad (2.20)$$

In the above equation, the mode shapes satisfy the orthogonality conditions given in Equations (2.5) and (2.6). The expression for the normalization factor $R_{(m_x,m_y,m_z)}$ is given by,

$$R^2_{(m_x,m_y,m_z)}\int_0^{L_{rx}} \cos^2\left(\frac{m_x\pi}{L_{rx}}x\right)dx\int_0^{L_{ry}} \cos^2\left(\frac{m_y\pi}{L_{ry}}y\right)dy\int_0^{L_{rz}} \cos^2\left(\frac{m_z\pi}{L_{rz}}z\right)dz = V \qquad (2.21)$$

which becomes, using trigonometric identities,

$$\begin{cases} R_{(m_x,m_y,m_z)} = 2\sqrt{2} \text{ if } m_x,m_y,m_z \geq 1 & (2.22a) \\ R_{(m_x,m_y,m_z)} = 2 \text{ if one of the indices is 0} & (2.22b) \\ R_{(m_x,m_y,m_z)} = \sqrt{2} \text{ if two of the indices are equal to 0} & (2.22c) \\ R_{(m_x,m_y,m_z)} = 1 \text{ if all three indices are zero} & (2.22d) \end{cases}$$

The case of rooms with arbitrary geometries is not treated in this research but could easily be solved using acoustic finite elements.

2.6 A New Model for Room Openings and Interconnected Rooms

In this section, a new formulation is presented to model openings interconnecting rooms and to the outside. The formulation is based on the Helmholtz resonator approach and was derived specifically to be implemented in the structural-acoustic model.

Previous research [51,52,54,55] suggests that rooms with openings may be considered as Helmholtz resonators as long as the opening dimensions are much smaller

than the acoustic wavelength. The motion of the resonator is analogous to that of a mechanical system having lumped elements of mass, stiffness, and damping. The fluid in an opening is induced to move forward and backward like a piston and provides the mass element of the system. The fluid in the room provides the stiffness element of the system as a result of the bulk compressibility. The damping element is provided by the radiation of sound at the opening, which leads to some dissipation of acoustic energy.

The equivalent mass of this opening can be expressed as [54],

$$m = \rho_r S L_e \tag{2.23}$$

where ρ_r is the mass density of the fluid, S is area of the opening section, and L_e is a certain effective length greater than the length (depth), l, of the opening, to account for displacement of air beyond the ends of the opening cavity. The effective length may be expressed as,

$$L_e = l + 2\delta \tag{2.24}$$

where δ is the end correction, which is function of the dimensions and shape of the opening [60]. For a rectangular opening, the end correction is given as,

$$\begin{aligned}\delta = \frac{2S}{\pi L}\Bigg\{&\left(1+\frac{1}{\alpha}\right)\ln\left[\left(1+\alpha^2\right)^{1/2}+\alpha\right]+\left(1+\alpha\right)\ln\left[\left(1+\frac{1}{\alpha^2}\right)^{1/2}+\frac{1}{\alpha}\right]+\\&+\frac{1}{3}\alpha\left(1+\alpha\right)\left[1+\frac{1}{\alpha^3}-\left(1+\frac{1}{\alpha^2}\right)^{3/2}\right]\Bigg\}\end{aligned} \tag{2.25}$$

Where L is the perimeter of the opening and α is the aspect ratio of the largest to the smallest dimension of the opening.

On the other hand, the equivalent stiffness of the fluid in the room can be expressed as [61],

$$k = \rho_r c^2 \frac{S^2}{V} \tag{2.26}$$

where c is the speed of sound in the fluid, and V is the volume of the room.

The above mass and stiffness properties can be used within a lumped-parameter model (Helmholtz resonator approach) where the structure is rigid, to model the acoustical behavior of interior cavities and openings at low frequency, as in the work of Hubbard and Shepherd [55]. However, a realistic structure vibrates and fluid-structure coupling contributes to the acoustic response in a significant fashion at low frequency, as demonstrated by the parametric study in Section 4. The lumped-modeling approach cannot be directly implemented if fluid-structure coupling is to be accounted for. The novelty of the numerical formulation developed in this research is to simultaneously model room openings and fluid-structure coupling. The approach to implement the formulation for room openings and interconnected rooms in the fully coupled structural-acoustic model presented in Section 2.3 is described below. The structural-acoustic model was primarily derived for isolated rooms, i.e. rooms not interconnected with openings. Advantage is taken of this model by treating room openings as structural components. In other words, the formulation for a closed door or window is replaced by a similar one that accounts for the dynamics of an opening. Therefore, rooms with openings can still be treated as isolated rooms.

The finite-element model presented in Section 2.4 to compute the eigenproperties of building structures is based on shell theory. The shell elements model the mid-plane of the structural components (walls, floors, doors, etc.) and thus have no physical thickness. The implication is that the mass-like behavior of the air in an opening will not be captured when discretizing the room cavity. Therefore, the approach taken is to assume that the room openings are modeled as "rigid piston" components with an equivalent mass computed from Equation (2.23) and an infinite stiffness. This is implemented in the finite-element model by discretizing the "rigid piston" component of the opening into a number of shell elements, the same as those modeling the other components of the building structure but with different material properties. Figure 2.7 shows the mesh of a wall segment with a door opening and the transition elements at the edges. For all shell elements forming the structure, including door openings, the element mass matrix is formulated using a lumping scheme, by distributing the mass of the element equally between its nodes. For openings, the element stiffness matrix is that of an isotropic material with a very large Young's modulus so that the elements do not move with respect to each other within the frequency range of the computations, e.g. 0 – 100 Hz. For the transition elements, the element stiffness matrix is also that of an isotropic material but with a very small Young's modulus so that the resonant frequencies of the piston moving as a rigid body are well below the first resonant frequency of the building structure and the sonic boom excitation, e.g. less than 1 Hz. Note that these resonant frequencies are not the same as those of the Helmholtz resonator system, which come from the interaction between the fluid in the room acting like a spring and the fluid in the doorway acting like a mass as illustrated in Section 3.4.

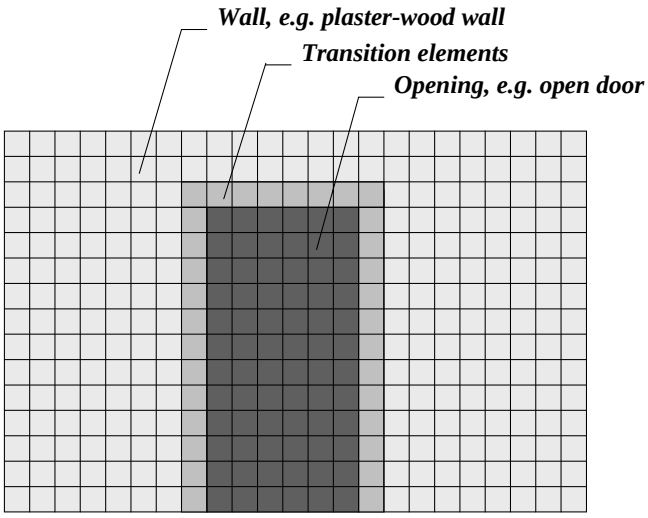

Figure 2.7: Mesh of a wall segment with an opening.

For the lumped-parameter model to be applicable, the characteristic length, L_c, of the opening must be much less than $\lambda/(2\pi)$, where λ is the acoustic wavelength. There is not a unique manner to define L_c for the type of opening geometries considered in this study, e.g. rectangular geometries. A reasonable assumption was to take L_c as the average of the two lengths of a rectangle, such as a door. A critical frequency, f_c, can then be expressed as $c/(2\pi L_c)$. Beyond this critical frequency, interconnected rooms are no longer coupled mechanically through the motion of the "rigid piston" but are coupled acoustically. One way to model this phenomenon while still considering the fluid in the opening as a structural component would be to have the mass and stiffness of the opening element approach zero. Then, the fluid in the opening acts like a membrane rather than a "rigid piston". The mass and stiffness properties of the opening element are frequency dependent. It is shown experimentally in Section 3.4 (see Figure 3.46) that the transition

occurring at the critical frequency is rather abrupt. Based on this experimental result, it would be a reasonable assumption to model the mass and stiffness properties of openings with step functions, as shown in Figure 2.8.

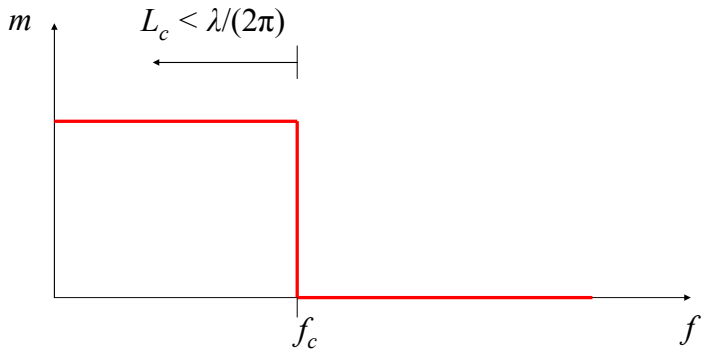

Figure 2.8: Equivalent mass of the piston as a function of frequency.

In this research, the acoustic response of interconnected rooms is computed below the critical frequency only, where the mass and stiffness properties of the openings are not frequency dependent. In this case, the formulation and time-domain solver presented in Section 2.3 for isolated rooms can be directly used to model room openings. Beyond the critical frequency, the formulation should be modified in a number of ways to handle the frequency-dependent properties of openings. These modifications were not implemented in this research but are presented below as recommendations for future work.

Firstly, the vibro-acoustic response of a fluid-structure system with openings should be solved with a frequency-domain solver. The set of modal equations describing the dynamics of the system in the time domain and written in compact form in Equation (2.10) can then be expressed in the frequency domain as,

$$\mathbf{I}(f)\ddot{\mathbf{u}}_f + \mathbf{C}(f)\dot{\mathbf{u}}_f + \mathbf{K}(f)\mathbf{u}_f = \mathbf{F}_f \tag{2.27}$$

Secondly, two sets of modes should be computed for the structure, a first set with the mass and stiffness properties of a "rigid piston" giving the matrices $\mathbf{I}_1$, $\mathbf{C}_1$, and $\mathbf{K}_1$, and a second set with those of a membrane giving the matrices $\mathbf{I}_2$, $\mathbf{C}_2$, and $\mathbf{K}_2$. The above set of modal equations in the frequency domain can then be separated into two sets, a first set solving for the system response below the critical frequency and a second set beyond it, which can be expressed as,

$$\mathbf{I}_1\ddot{\mathbf{u}}_f^1 + \mathbf{C}_1\dot{\mathbf{u}}_f^1 + \mathbf{K}_1\mathbf{u}_f^1 = \mathbf{F}_f^1 \tag{2.28}$$

$$\mathbf{I}_2\ddot{\mathbf{u}}_f^2 + \mathbf{C}_2\dot{\mathbf{u}}_f^2 + \mathbf{K}_2\mathbf{u}_f^2 = \mathbf{F}_f^2 \tag{2.29}$$

Thirdly, the inverse Fourier transform of the combined frequency-domain responses should be computed to obtain the time domain response of the fluid-structure system.

2.7 Pressure Loading Function

The external pressure loading on the structure can be decomposed into three pressure fields. The first is the blocked pressure, which is close to twice the incident pressure in the absence of the body, i.e. pressure doubling. This field may be computed with simple analytical expressions based on the geometry of the structure and angle of incidence of the wave. The second is the scattered field due to diffraction of the incident wave around the structure assumed rigid. The third is the radiated field, which is due to the elastic and inertial properties of the structure. The last two pressure fields are more involved and require numerical techniques, e.g. boundary element method.

The formulation for computing the pressure distribution on the structures was not carried out in this research. For the purpose of experimental validations, the pressure distribution is determined experimentally using microphones mounted on the external surfaces of the structure. As indicated in Figure 2.9, the microphone data is then interpolated and extrapolated to estimate the pressure at each node of the finite-element mesh used to compute the modal properties of the structure.

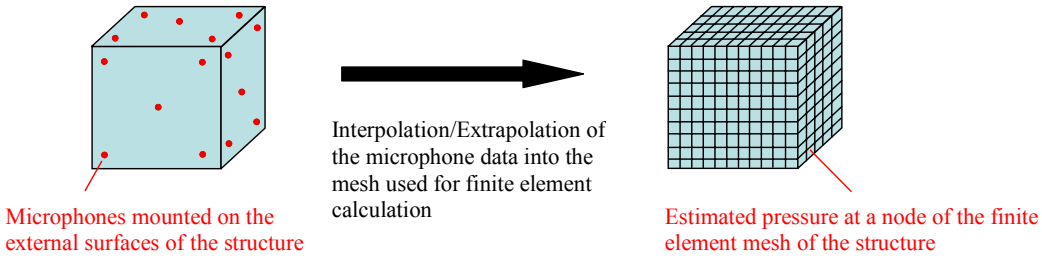

Figure 2.9: Schematic description of the approach used to estimate the pressure loading over a structure.

2.8 Computer Code

Based on the formulation presented above, a computer code was written in MATLAB. An overview of the code organization is shown in Figure 2.10. The code is organized in different modules. The core of the code (red box) is based on the structural-acoustic model presented in Section 2.3. It formulates the system of equations governing the modal dynamics of a given fluid-structure system, expressed in compact form by Equation (2.10). The formulation of the matrices **C** and **K** requires knowledge of the structural modal properties and of the acoustic modal properties of each volume enclosed by the structure. Therefore, modules were developed (top two blue boxes) to provide the core of the code with the natural frequencies, mode shapes, and modal masses of the

acoustic and structural systems. The damping ratios were estimated from modal tests, which are described in Section 3. The structure geometry and properties are specified as inputs to the code (top two green boxes). The structure properties include for instance the orthotropic constants of the walls D_x and D_y, the Young's modulii of the doors and windows, and the mass density of the various structural components. Using these inputs, a finite-element module (top black box) discretizes the structure into shell elements and computes its "in vacuo" eigenproperties, following the formulation presented in Section 2.4. The code is restricted for now to rectangular room geometries. Therefore, the interior acoustic modal properties are computed using the analytical expressions given in Equations (2.19) and (2.20). Finally, a module provides the core of the code with the modal force $\mathbf{F}_t$ that is computed using the structural mode shapes and the measured external pressure loading. Currently the computer code does not have a routine that computes the pressure distribution on the structure. In order for this code to be truly practical, this module needs to be created in the future. A Newmark-β algorithm (bottom blue box) then integrates the dynamic modal equations of the fluid-structure system. The direct outputs (top orange box) from this numerical integration are: 1) the modal structural displacement, and its time derivatives, and 2) the modal velocity potentials in the interior volumes, and their time derivatives. Finally, using modal summation, the vibro-acoustic response of the system is obtained in the physical (as opposed to modal) domain (bottom orange box).

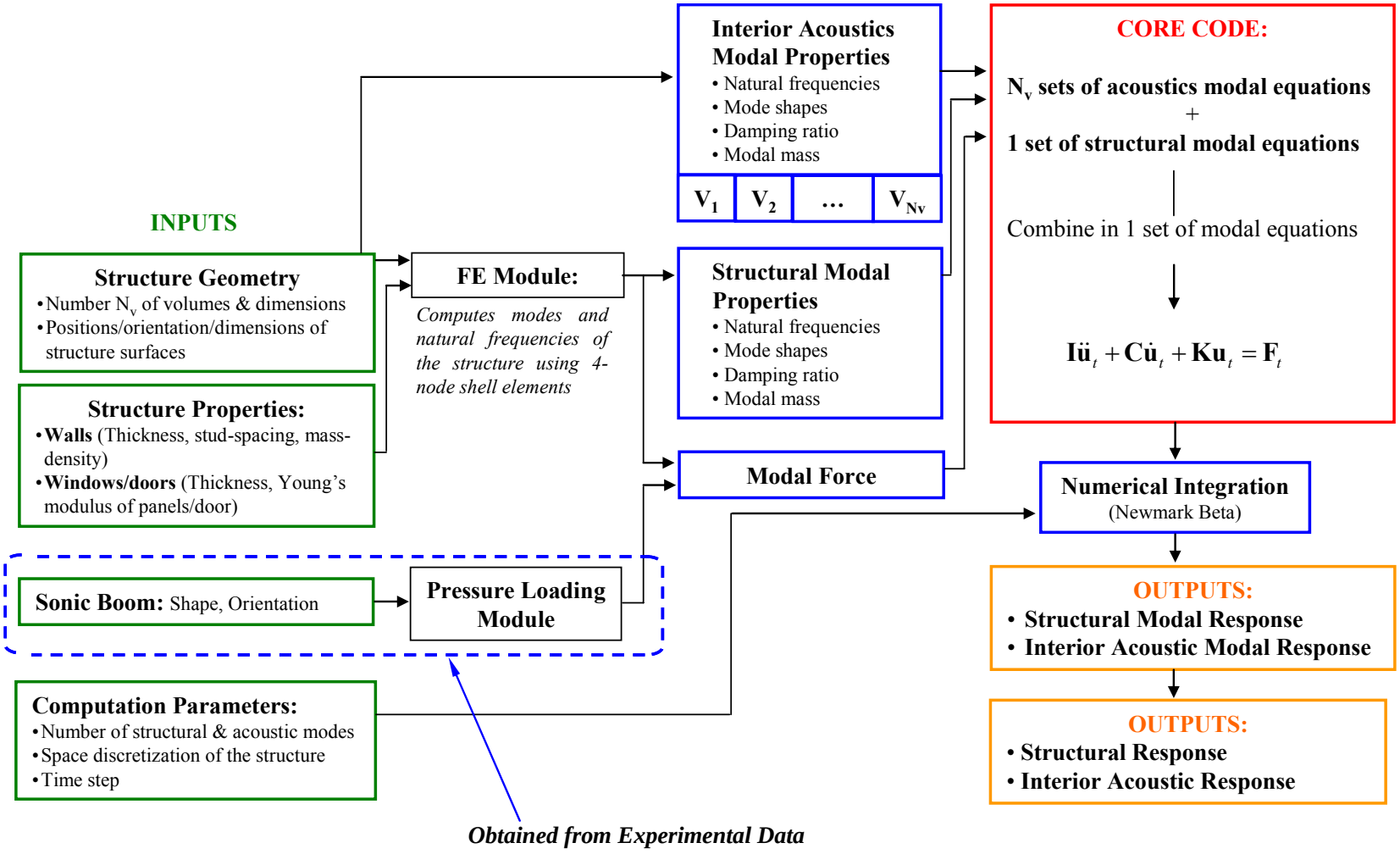

Figure 2.10: Flow chart of the code.

3. Experimental Validation of the Numerical Model

The three tests structures shown in Figure 3.1 are considered for experimental validation of the model and computer code presented in Section 2. The first test structure is a single plaster-wood wall backed by a rectangular room made of cinderblocks (rigid structure). The external pressure loading on the wall is generated with a speaker playing sonic booms of unrealistic durations and amplitudes. This test case was chosen for its simplicity, i.e. interaction of one structure component with one volume, and was used for a preliminary validation of the model. In the next two cases, the excitation and the structures are more realistic. The external pressure loading is generated by an explosive technique. The second test structure is a single room made of plaster-wood wall with two double-panel windows and a door. The third test structure consists of two rooms interconnected with a door, and two attic cavities above the rooms. This latter case is the most realistic. It involves the interaction of several structural components with multiple rooms. In addition, for this case, booms are generated from two directions.

Sections 3.1 through 3.3 treat the cases of structures with volumes fully enclosed by structural components (isolated rooms), meaning that for the single- and two-room structures, the doors interconnecting rooms and to the outside are kept closed. In Section 3.4, the validation of the modeling effort for room openings is presented. In this case, several configurations of the two-room structure are considered, first with only the interior door open, then with both doors open.

Figure 3.1: Test structures used for experimental validation.

3.1 Single Plaster-Wood Wall

3.1.1 Experimental Setup

Figure 3.2a) shows the test structure consisting of a plaster-wood wall mounted in the rectangular opening of a cinderblock room. The plaster wood wall was built following standard construction techniques [62]. The wall frame shown in Figure 3.2b) was made of 3.8×8.9-cm (1.5×3.5-inch) studs spaced 30 and 40 cm (12 and 16 inches) apart. The frame was sandwiched between wood-panel oriented strand boards (OSB) and plaster boards that were fastened to the studs to form the outside and inside wall surfaces, respectively. The OSB and plaster boards had a thickness of 1.27 cm (1/2 inch) and masses per unit area of 7.6 and 8.6 kg/m^2, respectively. Cavities in the wall were filled in with standard R-13 insulation. The finished wall was 2.21-m (87-inches) long, 1.82-m (71.5-inches) wide, and 11.4-cm (4.5-inches) thick. The cell had a width of 2.23 m (88 inches), a height of 2.6 m (102 inches), and a depth of 2.3 m (91 inches). A wood frame was secured into the opening of the cinderblock cell to mount the wall. The wall was fastened to the frame by its internal studs using mounting brackets. Last, self expanding

foam was inserted into the gaps between the wall and the room to seal the assembly acoustically.

A speaker built in-house was used to produce the external pressure loading on the wall. The speaker was made of a 63.5-cm (25-inch) subwoofer driver and a sealed cubic enclosure of 80 cm (31.5 inches). The speaker was placed in front of the wall at 2 m from the center. N-waves with durations ranging from 10 to 33.6 ms were played. The input signal had to be pre-distorted to account for the dynamics of the speaker-amplifier system and yield the desired output waveform. The wave superposition technique was used for this purpose [12]. As an example of the method, Figure 3.3a) shows the desired output waveform. This signal is input to the speaker and the response of a microphone on the structure recorded as shown in Figure 3.3b). These two time histories are then used to estimate how the input signal needs to be modified to account for the speaker dynamics and the presence of the structure. Figure 3.4a) shows the new signal that needs to be fed to the speaker after applying this method. The resulting response at the microphone is then shown in Figure 3.4b), which matches the original desired signal in Figure 3.3a) quite well.

The external pressure loading was monitored with an array of 21 microphones mounted to the outside of the wall, following the pattern shown in Figure 3.5a). In addition, three microphones were used to monitor the interior acoustics. These were positioned close to the center of the wall surface, center of the room, and in a corner of the room. The microphones were quarter-inch Panasonic WM-60AY Electret models

with a standard instrumentation amplifier conditioning circuit. An array of 36 accelerometers was mounted to the inside of the wall (on the plaster) to monitor the wall vibration, following the pattern shown in Figure 3.5b). The accelerometers were PCB model 330A calibrated in house. The microphone and accelerometer signals were acquired simultaneously with a sampling frequency of 12.8 kHz.

a)

b)

Figure 3.2: a) Plaster-wood wall instrumented with microphones and installed in the cinderblock room, and b) wall frame with insulation.

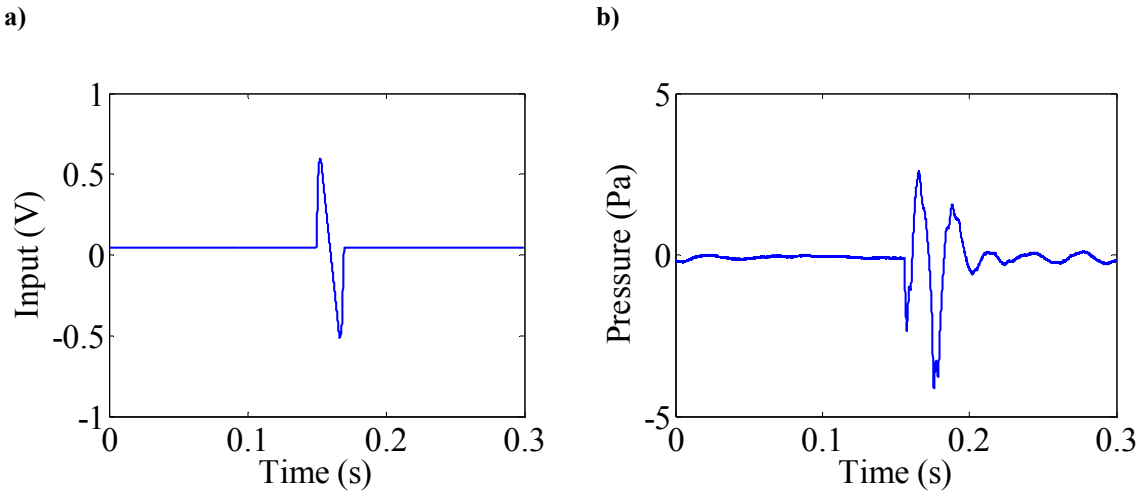

Figure 3.3: Measured (a) input and (b) output waveforms before pre-distorting the input signal.

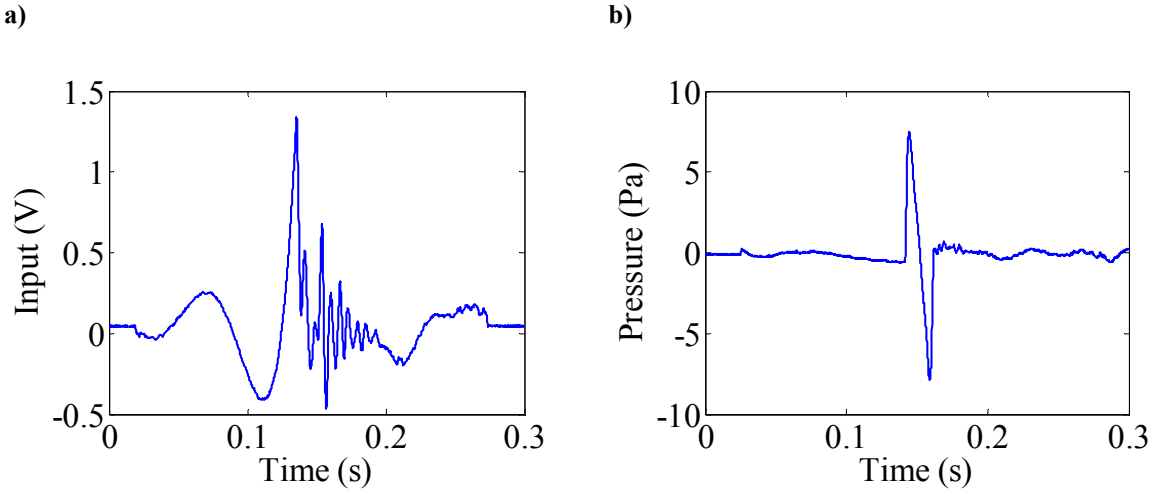

Figure 3.4: Measured (a) input and (b) output waveforms after pre-distorting the input signal.

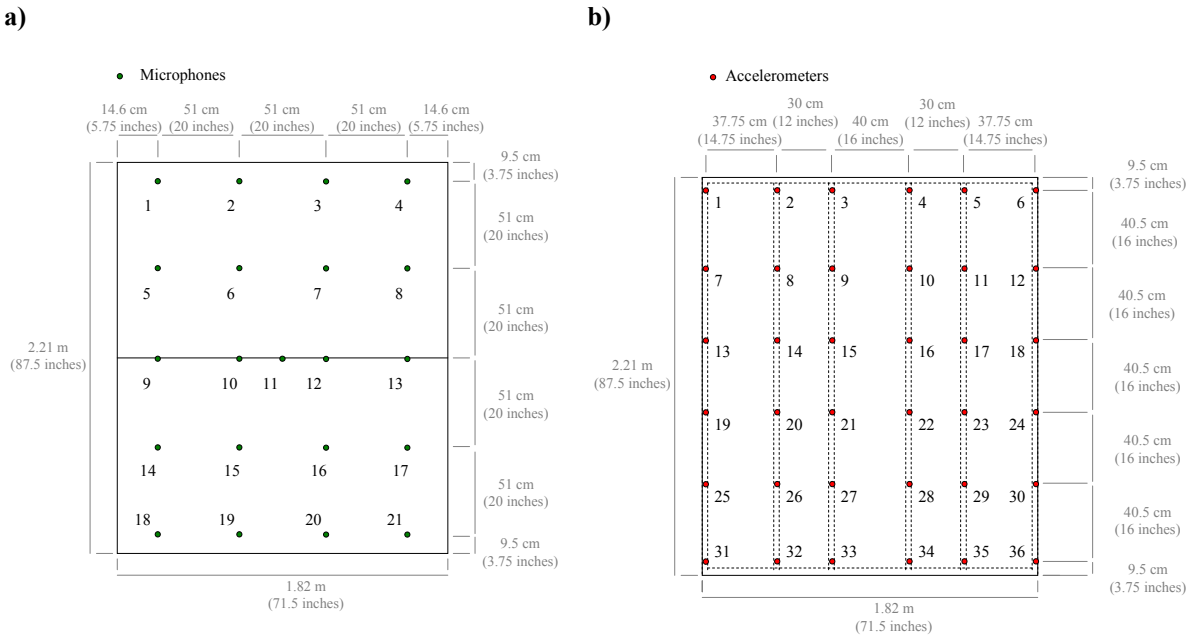

Figure 3.5: Positions and numbering of the sensors mounted on the wall, a) microphones on the outside surface and b) accelerometers on the inside surface.

3.1.2 Structural Modal Properties

The structural-acoustic model requires knowledge of the structural modal parameters, i.e. natural frequencies, mode shapes, and modal damping ratios. The natural frequencies and mode shapes were computed numerically using the finite-element model presented briefly in Section 2.4.1 and in more details in Appendix B. Modal testing was then conducted to provide experimental data against which the numerical predictions can be compared to, and also to extract the modal damping ratios of the wall.

The wall was discretized into 357 shell elements (396 nodes) and was assumed to be simply supported. At the nodes on the edge of the wall, the three Cartesian components of the displacement were constrained to zero. The equivalent orthotropic constants of the

wall were calculated with Equations (2.15) and (2.16). It was found that D_x = 623 and D_y = 153000 N.m. The mass per unit area of the wall was found to be 25 kg/m^2.

For the structural-acoustic model, 50 structural modes were computed, which covers a frequency range of 0 – 325 Hz. The bending wavelength at 325 Hz of an infinite plate with a bending rigidity of 623 N.m is λ_b = 0.31 m, which is close to four times the largest element length of 0.1 m. Therefore, the mesh size should be adequate to carry out the numerical simulations.

Conventional modal testing and analysis of the plaster-wood wall as installed in the cinderblock structure were conducted. Figure 3.6 is a picture of the experimental setup for testing. A shaker hanging from an aluminum stand and attached to the structure with a stinger was used to excite the wall. The array of accelerometers mentioned previously recorded the resulting response and a force transducer was used to measure the input force. The shaker was driven with white noise and data was collected at 6400 Hz for several input configurations. The wall was excited at three different positions along the wall studs with two different levels of excitation at each position. Two of these positions were symmetric with respect to the center of the wall, to check for reciprocity. The third position, near a corner of the wall, was selected to insure that all the modes were excited. Testing two excitation levels showed that the structure behaved linearly for the level of excitation provided.

The measured transfer functions (FRFs) between the accelerometers and the force transducer were calculated and used to extract the modal parameters. A sample FRF is plotted in Figure 3.7 and its associated coherence in Figure 3.8. These figures indicate that resonance peaks can be detected and the coherence is reasonable for experimental data in the frequency ranges around the resonances, so modal analysis was carried out. Modal damping ratios were estimated using the half-power method. Beyond the third mode, the modal parameters could not be accurately determined. Mode shapes were then computed using the values of the complex FRFs at the natural frequencies of the wall.

Figure 3.6: Experimental setup of the modal test.

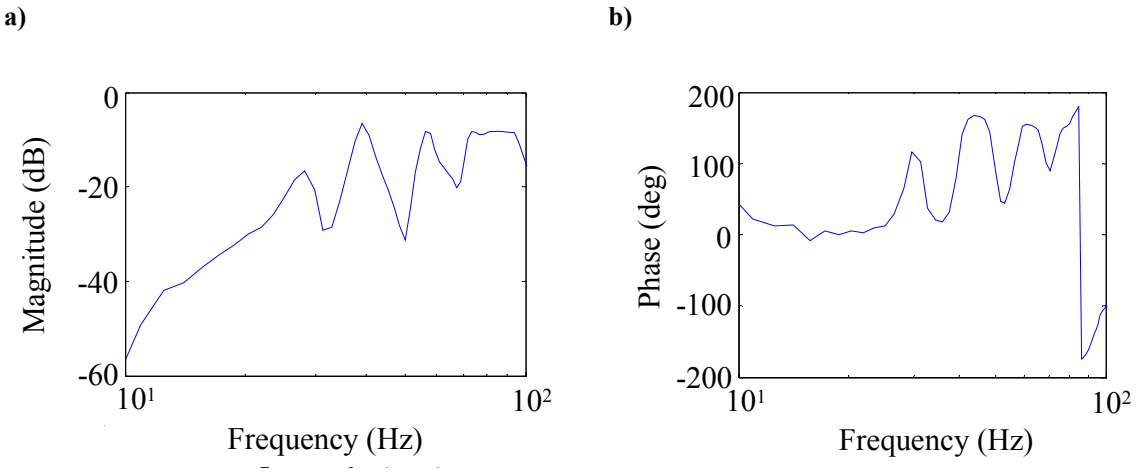

Figure 3.7: Measured FRF from accelerometer 11 a) magnitude and b) phase.

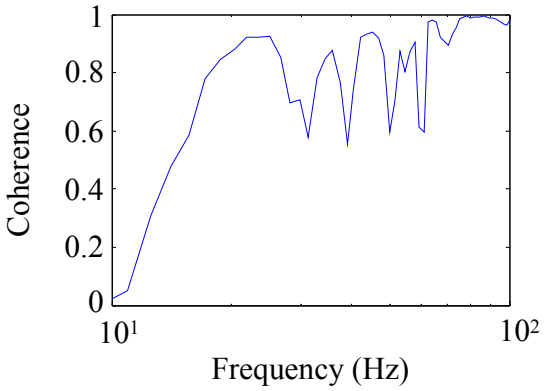

Figure 3.8: Measured coherence from accelerometer 11.

Table 3.1 reports the natural frequencies and modal damping ratios of the wall measured for the first three modes and the natural frequencies computed numerically for the first six modes. Numerical predictions of the natural frequencies are in very good agreement (less than 6% error for the first three modes) with the experimental data. Figure 3.9 and Figure 3.10 show the mode shapes of the wall obtained numerically and experimentally, respectively. Mode shapes determined numerically exhibit similar patterns to those obtained experimentally. In the finite-element model, the wall was

assumed to be simple supported, which does not capture the deformation of the wall edges observed experimentally.

Table 3.1: Natural frequencies and modal damping ratios of the wall measured using conventional modal testing, and natural frequencies computed numerically.

	Experimental		Analytical	
n	f_n^s (Hz)	ξ_n^s	f_n^s (Hz)	Error (%)
1	28.3	0.038	29.2	3.2
2	40.5	0.03	39.2	3.2
3	57.1	0.029	53.6	6.1
4	/	/	71.8	/
5	/	/	93.8	/
6	/	/	97.8	/

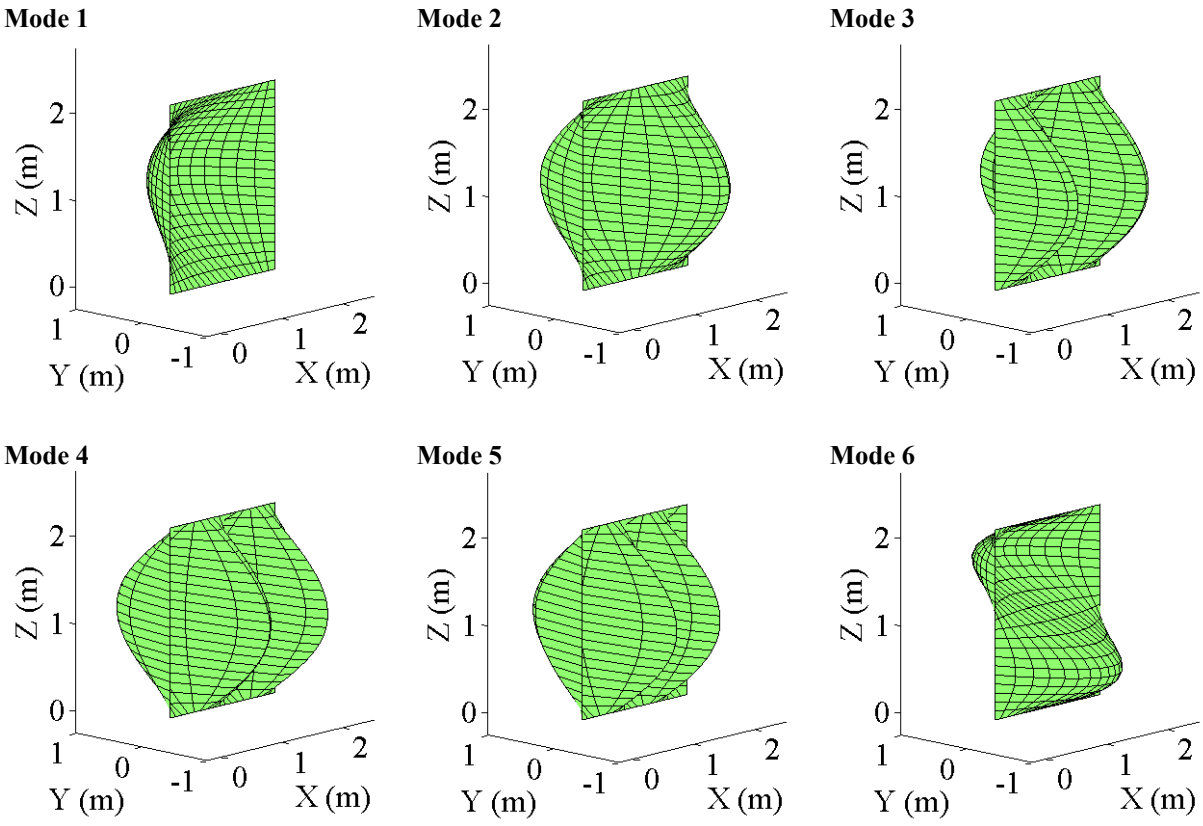

Figure 3.9: First six mode shapes of the wall computed numerically.

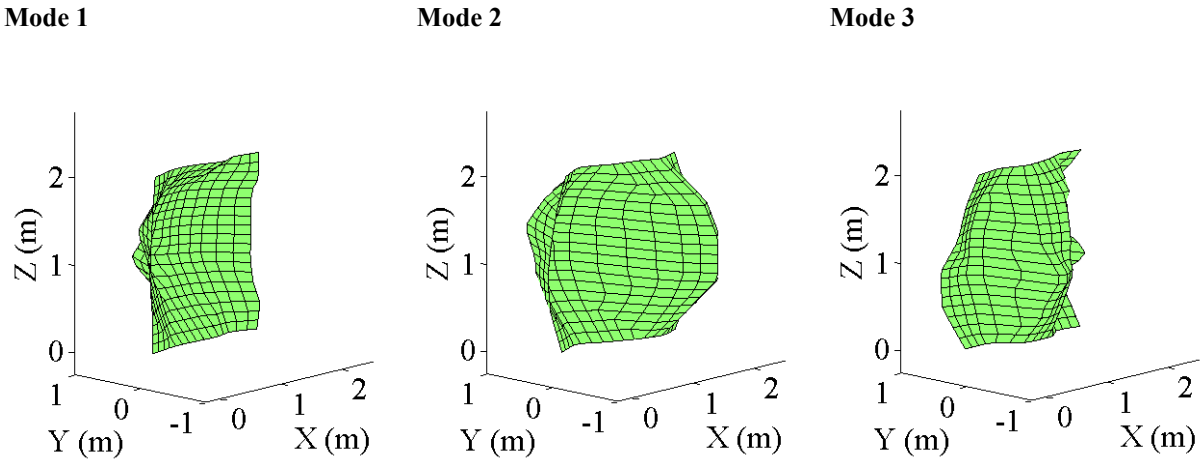

Figure 3.10: First three mode shapes of the wall obtained from conventional modal testing.

3.1.3 Acoustic Modal Properties

The natural frequencies and mode shapes for the room with perfectly reflecting surfaces (hard walls) were computed analytically with Equations (2.19) and (2.20). The modal properties of the room were also determined experimentally for validation purposes and to extract the acoustic modal damping ratios. A speaker playing white noise was placed in a corner of the room. The three interior microphones were used to record the pressure fluctuation. The pressure spectra along with the half power method were used to estimate the natural frequencies and modal damping ratios for the first three acoustic modes. Table 3.2 reports the natural frequencies and modal damping ratios of the room obtained experimentally and the natural frequencies of the room with perfectly reflecting surfaces computed analytically. Natural frequencies of the room computed analytically are within 5% of those obtained experimentally for the first three modes, which indicates that the acoustic modes of the room can be computed using the

assumption of perfectly reflecting surfaces. For the structural-acoustic model, 76 acoustic modes were computed, which covers a frequency range of 0 to 325 Hz.

Table 3.2: Acoustic natural frequencies of the room and modal damping ratios obtained experimentally and natural frequencies computed analytically.

	Experimental		**Analytical**	
m	$f_m^a\,(\mathrm{Hz})$	ξ_m^a	$f_m^a\,(\mathrm{Hz})$	Error $(\%)$
1	64	0.032	66.2	3.4
2	75	0.032	74.2	1.1
3	81	0.043	76.8	5.2

3.1.4 Vibro-Acoustic Response

In this section, the predicted vibro-acoustic response of the structure is compared to experimental data. The analysis of the results is carried out for two sonic-boom durations, 20 and 33.6 ms. Note that the latter wave duration is close to the period of the fundamental structural mode.

Time histories and magnitudes of the Fourier transform (FT) of the acceleration on the inside wall surface, close to the wall edges (accelerometers 3 and 18), closer to the center of the wall (accelerometers 8 and 10), and the closest to the center of the wall (accelerometers 15 and 20), are shown in Figure 3.11 and Figure 3.12 for the 20-ms N-wave and in Figure 3.13 and Figure 3.14 for the 33.6-ms N-wave, respectively. In the figures and in the rest of the section, the blue and red curves correspond to the measured and predicted responses, respectively. Experimental data from accelerometers 3 and 18 indicate that the wall edges vibrate significantly, with a maximum at 162 Hz near the top

and bottom of the wall (e.g. accelerometer 3) and at 28 Hz near the center of the wall vertical edge (e.g. accelerometer 18). At 162 Hz, the wall-mounted microphones close to the top and bottom of the wall exhibited a larger magnitude than the desired spectrum due to imperfections in the method of external pressure generation. The wall edges vibrate because the wall was mounted to the cinderblock cell using brackets, which do not provide a true and continuous simply-supported boundary condition. On the other hand, in the model, simply-supported boundary conditions impose no displacement on the edges. As a result, the acceleration of the wall is under-predicted near the edges. The discrepancy between experimental and numerical results observed at 162 Hz is caused by the vibration of the of top and bottom edges that is not captured by the simply-supported boundary conditions assumed in the model. At other locations, away from the wall edges, numerical predictions are in very good agreement with experimental data, e.g. accelerometers 8, 10, 15, and 20. However, the response remains under-predicted near 162 Hz as a result of the vibration of the wall edges not captured by the model.

Figure 3.15 and Figure 3.16 show the time histories (left column) and magnitudes of the FT (right column) of the pressure close to the center of the wall surface, at the center of the room, and in a corner of the room for N-waves with durations of 20 and 33.6 ms, respectively. At the three microphone locations, predictions of the interior pressure are in very good agreement with experimental data, for both boom durations. At the center of the room, the model under-predicts the pressure above 40 Hz. This is again believed to be due to the vibration of the wall edges that the model does not account for. The

contribution to the acoustic response from the edge vibration is likely to be small close to the center of the wall surface and to increase as the observer moves away from the wall.

The plaster–wood wall was considered as a uniform orthotropic plate in the prediction model. However, sound is also transmitted through the cavities between the OSB and plaster panels. The mass–air–mass resonance frequency is expressed as [50],

$$f_0 = \frac{1}{2\pi}\left[\left(\frac{\rho_c c^2}{d}\right)\left(\frac{m_1 + m_2}{m_1 m_2}\right)\right]^{1/2} \tag{3.1}$$

where d is the distance between the panels (d = 8.9 cm), ρ_c is the density of the fluid in the cavity, m_1 and m_2 are the respective masses per unit area of the panels (7.6 kg/m^2 for OSB and 8.6 kg/m^2 for plaster). Assuming that the cavities are filled in with air (ρ_c = 1.2 kg/m^3), it is found that f_0 = 100 Hz. Therefore, around this frequency, it can be expected that more sound will be transmitted into the room cavity than what the model predicts.

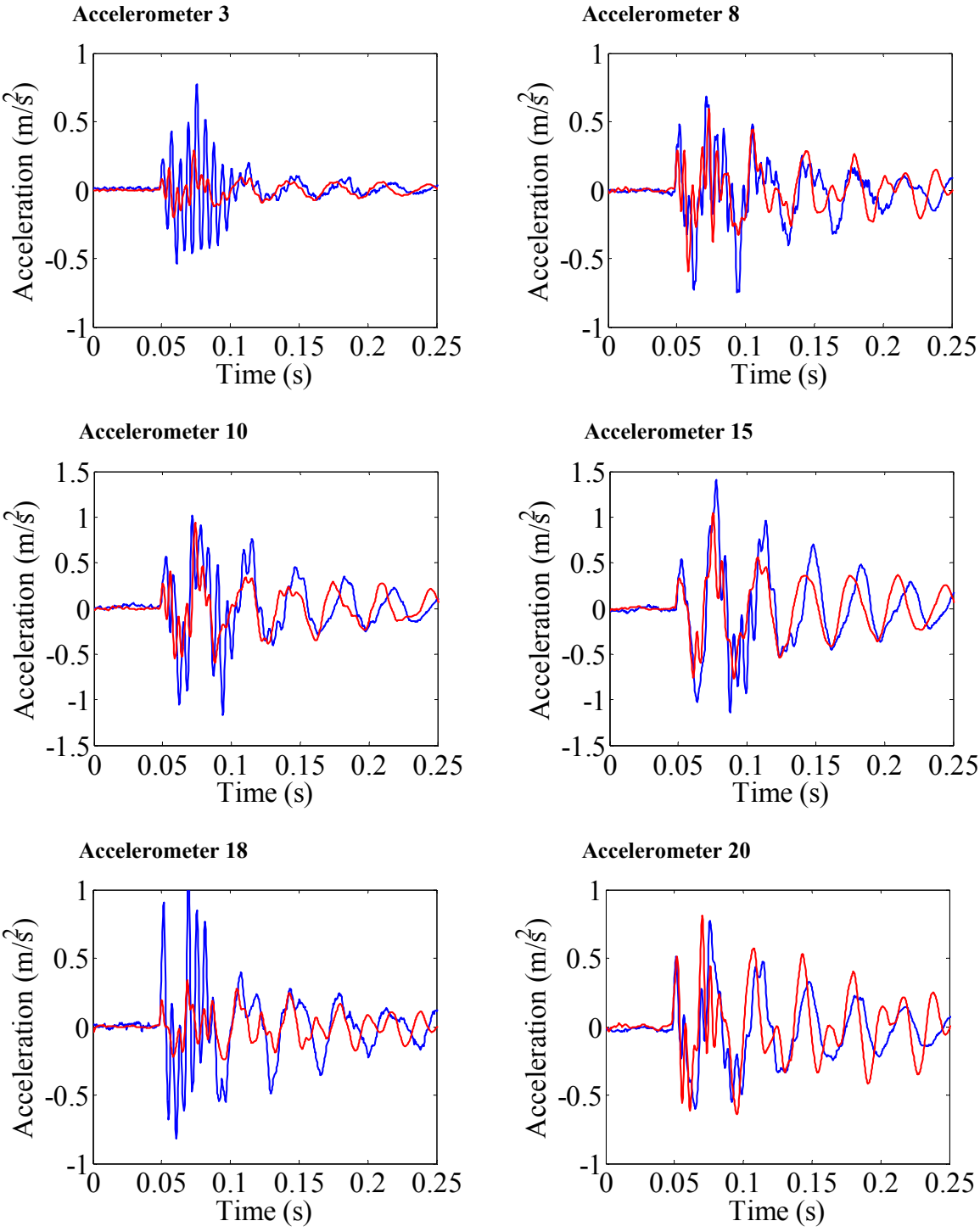

Figure 3.11: Accelerations on the inside wall surface as a function of time, measured (blue) and predicted (red), for a sonic boom with duration of 20 ms.

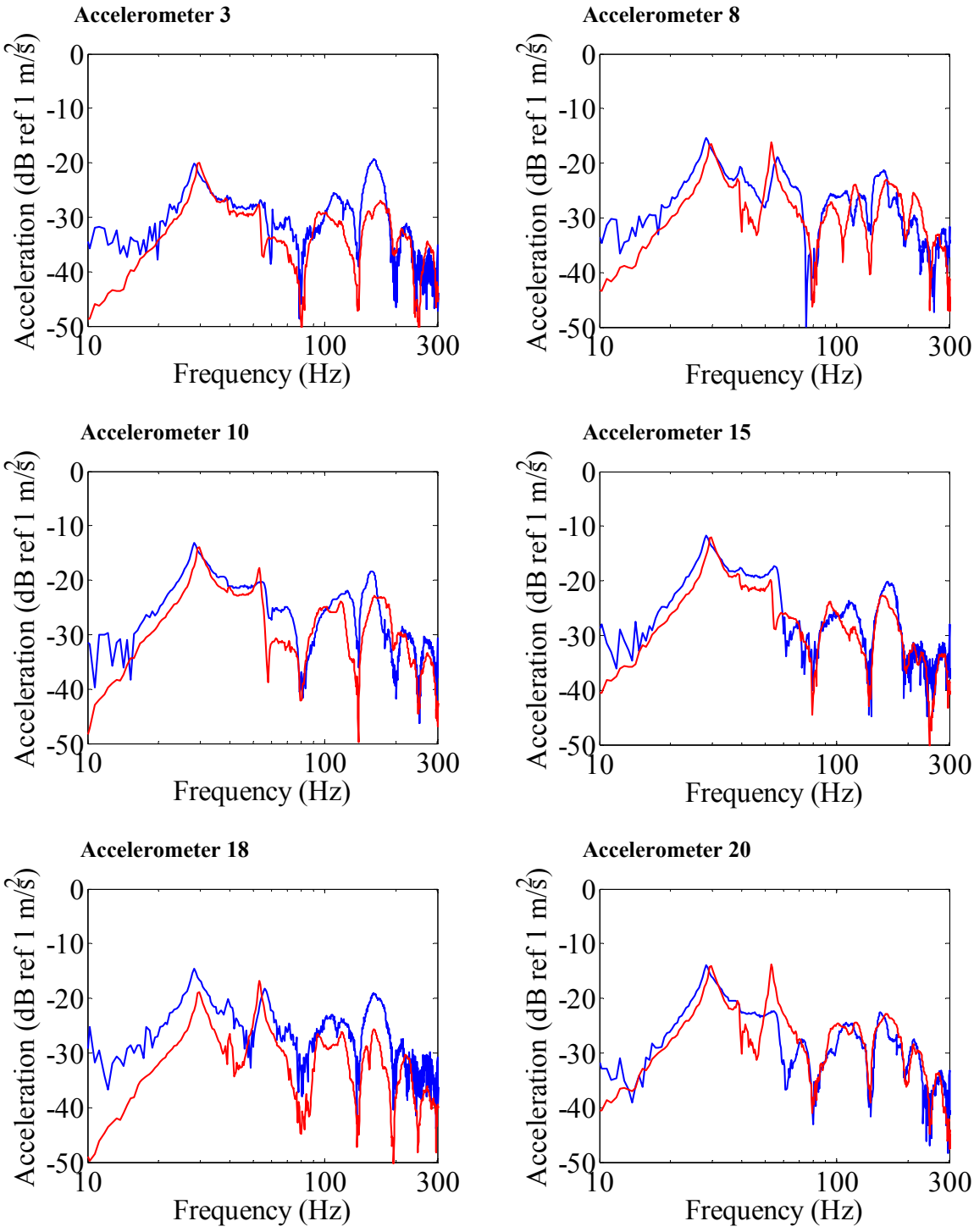

Figure 3.12: Magnitudes of the FT of the accelerations on the inside wall surface, measured (blue) and predicted (red), for a sonic boom with duration of 20 ms.

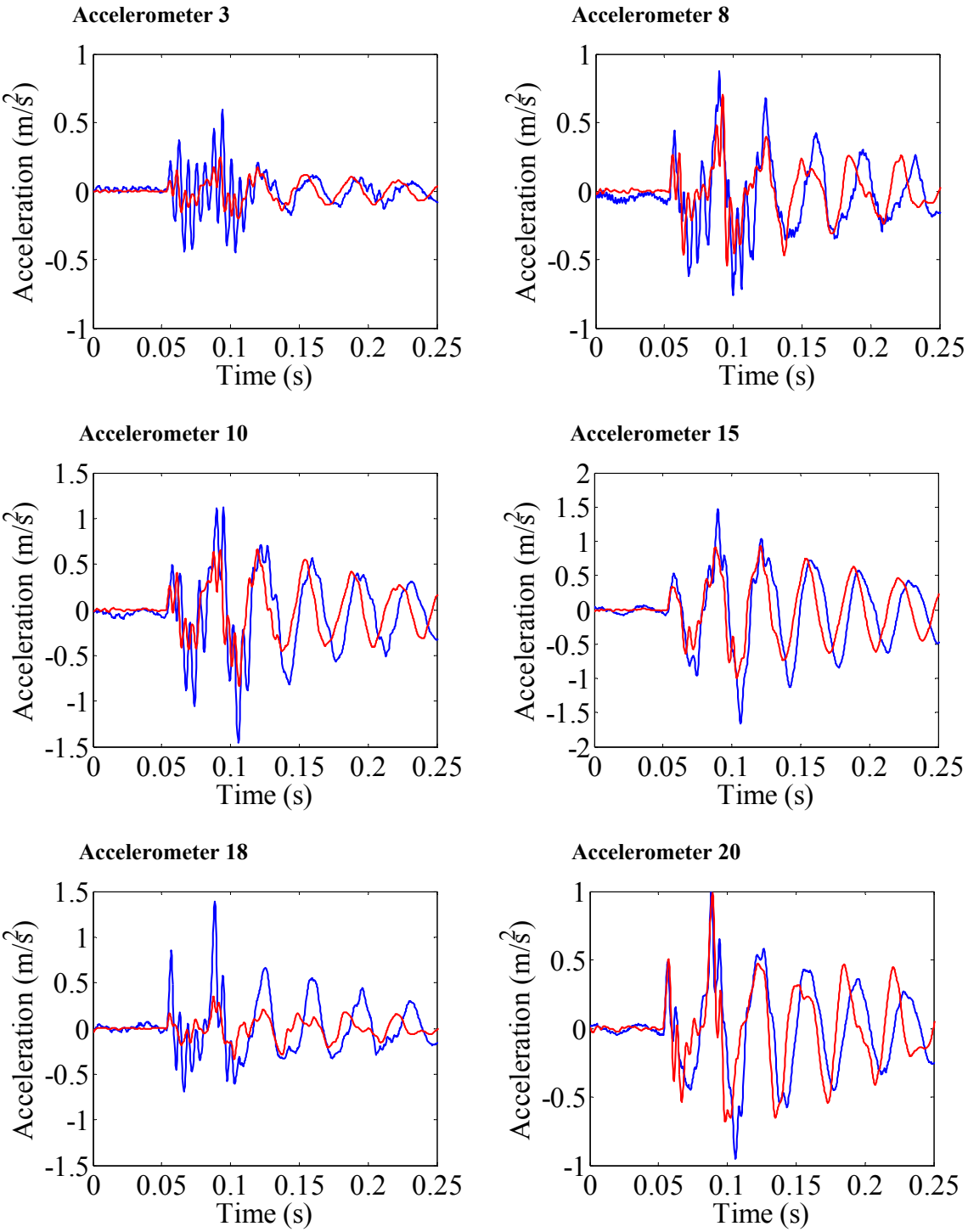

Figure 3.13: Accelerations on the inside wall surface as a function of time, measured (blue) and predicted (red), for a sonic boom with duration of 33.6 ms.

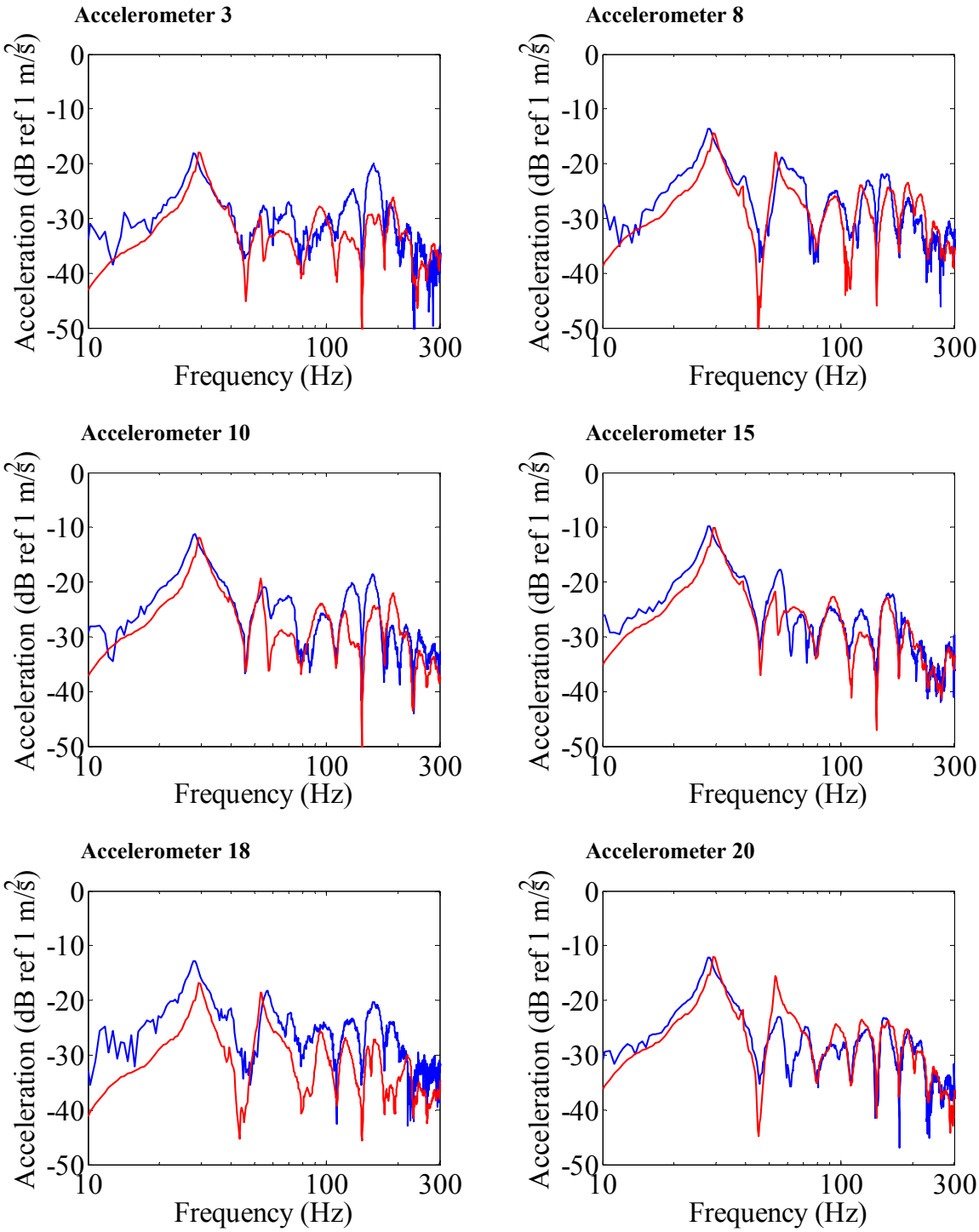

Figure 3.14: Magnitudes of the FT of the accelerations on the inside wall surface, measured (blue) and predicted (red), for a sonic boom with duration of 33.6 ms.

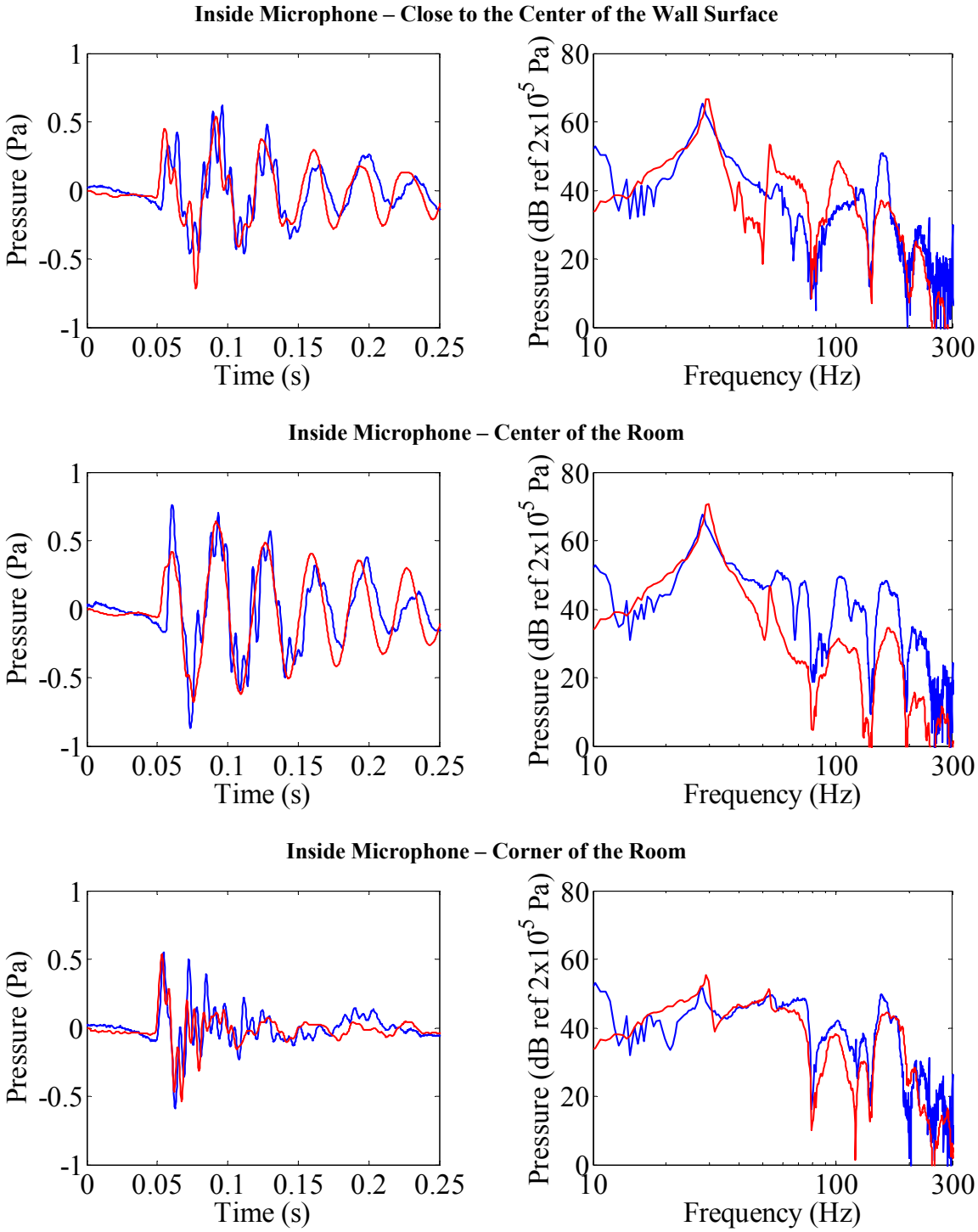

Figure 3.15: Pressures inside the room, time histories (left) and magnitudes of the FT (right), measured (blue) and predicted (red), for a sonic boom with duration of 20 ms.

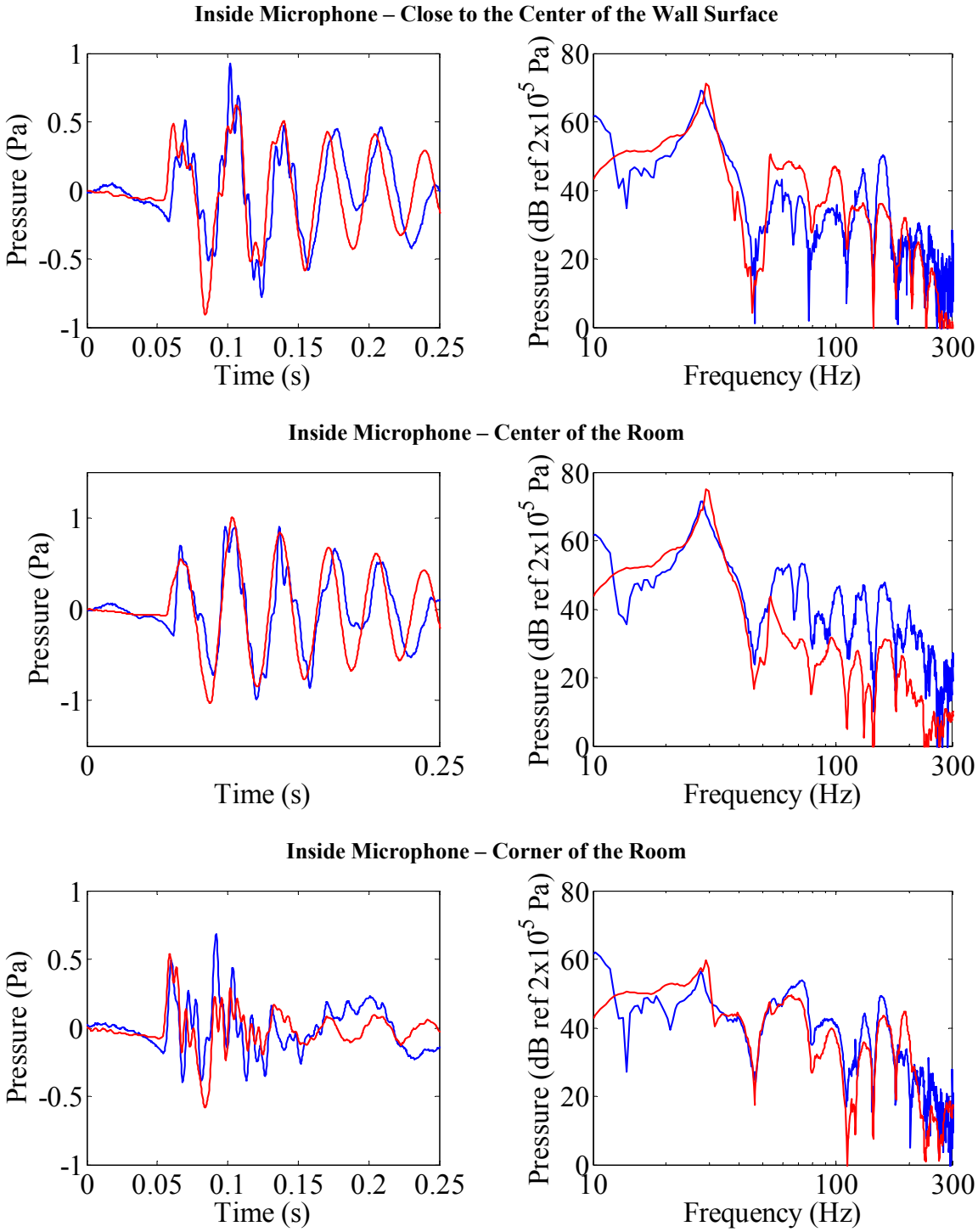

Figure 3.16: Pressures inside the room, time histories (left) and magnitudes of the FT (right), measured (blue) and predicted (red), for a sonic boom with duration of 33.6 ms.

3.1.5 Sensitivity to External Pressure Loading

Figure 3.17a and b show the time histories and magnitudes of the FT of the acceleration at the location of accelerometer 15 on the wall, respectively. Figure 3.18a and b show the time histories and magnitudes of the FT of the pressure in a corner of the room. The red solid curves correspond to responses due to an external pressure loading estimated by interpolating and extrapolating the data collected from the wall-mounted microphones, as described in Section 2.6. The blue dashed curves correspond to an external pressure loading estimated by averaging the microphone data over the wall surface. In this case, the effects of the diffracted field and ground-reflected wave that causes the pressure loading over the wall surface to be non-uniform at each time step are averaged, and thus ignored. The acceleration is virtually insensitive to the technique used to estimate the external pressure loading up to 200 Hz. Beyond this frequency range, averaging the microphone data over the wall surface results in under-predicting the wall response. In other words, diffraction and the ground-reflected wave have an effect on the structural response only at high frequencies. This result is in good agreement with the fact that diffraction is caused by the corners of opening in the cinderblock structure and thus expected to occur at relatively high frequency. The pressure predicted with an averaged pressure loading is virtually the same as that predicted with an interpolated one, across the full frequency range considered here, i.e. 0 – 300 Hz.

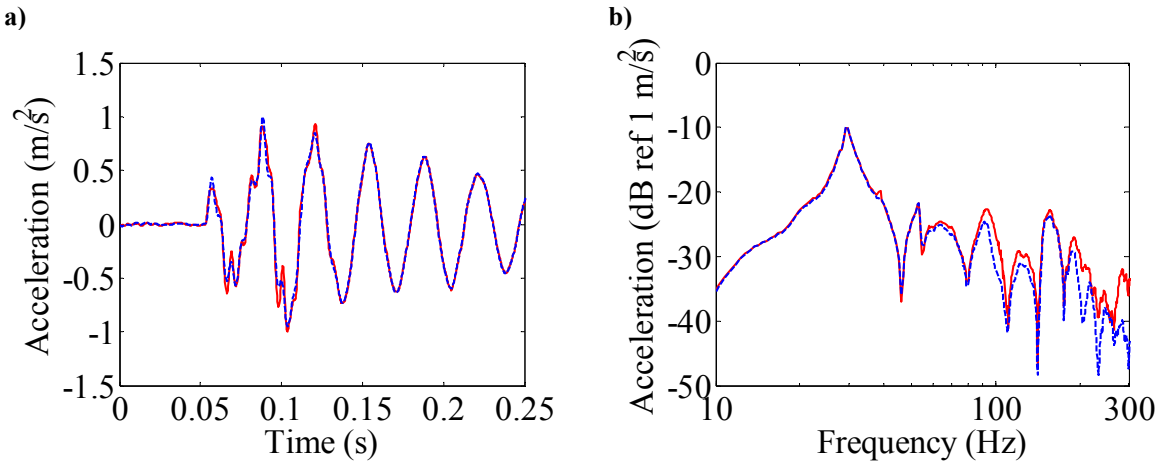

Figure 3.17: Acceleration at the position of accelerometer 15, a) time histories and b) magnitudes of the FT, computed for an external pressure loading where microphone data were interpolated (red solid curve) and averaged (blue dashed curve).

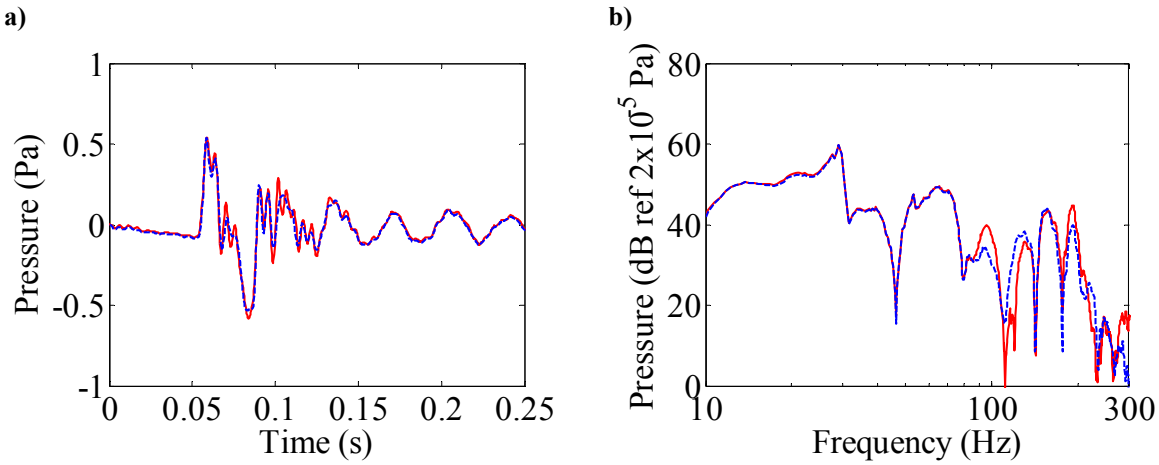

Figure 3.18: Pressure in a corner of the room, a) time histories and b) magnitudes of the FT, computed for an external pressure loading where microphone data were interpolated (red solid curve) and averaged (blue dashed curve).

3.2 Single-Room structure

3.2.1 Experimental Setup

a) Test Structure

Figure 3.19 is a photograph of the test structure consisting of a single room with two double-panel glass windows and a wooden door. The finished structure had interior dimensions of 4.72×2.58×2.54 m (186×101.75×100 inches), so a net volume of 31 m^3

(1095 ft^3). Upon completion it was installed on the test site, not directly on the ground but rather on six cinderblocks. The vertical walls, floor, and ceiling forming the structure were built using standard construction techniques, similar to those for the single wall treated previously. Differences in the construction techniques for the vertical walls include the use of thicker OSB panels on the exterior surfaces, 0.02-m (3/4-inch), and a smaller spacing between the studs, 30 cm (12 inches), in order to obtain a stiffer structure during the transportation process from the construction site to the test site. The frame used for the floor consisted of 3.8×28.6-cm (1.5×11.25-inches) studs for its perimeter and was spanned by studs spaced 0.61 m (24 inches) apart. The inside surface of the floor consisted of OSB panels while the outside was left uncovered. The cavities inside the floor were filled in with R-21 fiberglass insulation. The frame of the ceiling was fabricated in the same manner as that of the floor except that 3.8×23.5-cm (1.5×9.25-inches) studs were used for the perimeter and 3.8×18.4-cm (1.5×7.25-inches) for the span. The vertical walls, floor, and ceiling were assembled together with screws distributed at about 0.5-m (20-inches) intervals. The six surfaces of the structure are referred to as front wall (wall with the windows), back wall (opposite to front wall), side wall with door, side wall (without door), ceiling, and floor.

Two double-panel glass windows were installed on the front wall of the test structure. The windows are standard nail fin vinyl picture windows with no moving parts. The dimensions of the panels are 0.70×0.94 m (27.5×37 inches) with space between the two glass panels of about 1.3 cm (1/2 inch). The window frames were secured directly to the

outside wall surface with screws. The edges of the vinyl window frame were then sealed with builder's caulk to minimize acoustic leakage.

A hollow-core masonite door, sized for an opening of 0.7×2.16 m (27.75×85 inches) with a depth of 0.11 m (4.5 inches), was installed on one of the walls adjacent to the front. The dimensions of the door are 0.69×2.01 m (27×79 inches). To install the door, the trim was joined in the opening and fastened to the studs surrounding the opening. The trim was also sealed with builder's caulk and weather stripping was installed on the door supporting edges.

Figure 3.19: Photograph of the single-room structure.

b) Test Site

Experiments were performed at Kentland Farm in McCoy, VA, a facility of Virginia Tech. A picture of the entire testing area is shown in Figure 3.20a. The approximate locations of the test structure and linear charge distribution are shown as well (not to scale). A close-up picture of the test site and structure is shown in Figure 3.20b and a dimensioned schematic of the structure, simulator, and exterior microphones is given in

Figure 3.20c. Kentland Farm is an appropriate outdoor testing location since there are no communities in the vicinity. The test structure was located in a field used primarily for hay production. The area immediately around the test structure and detonating cord posts is relatively flat.

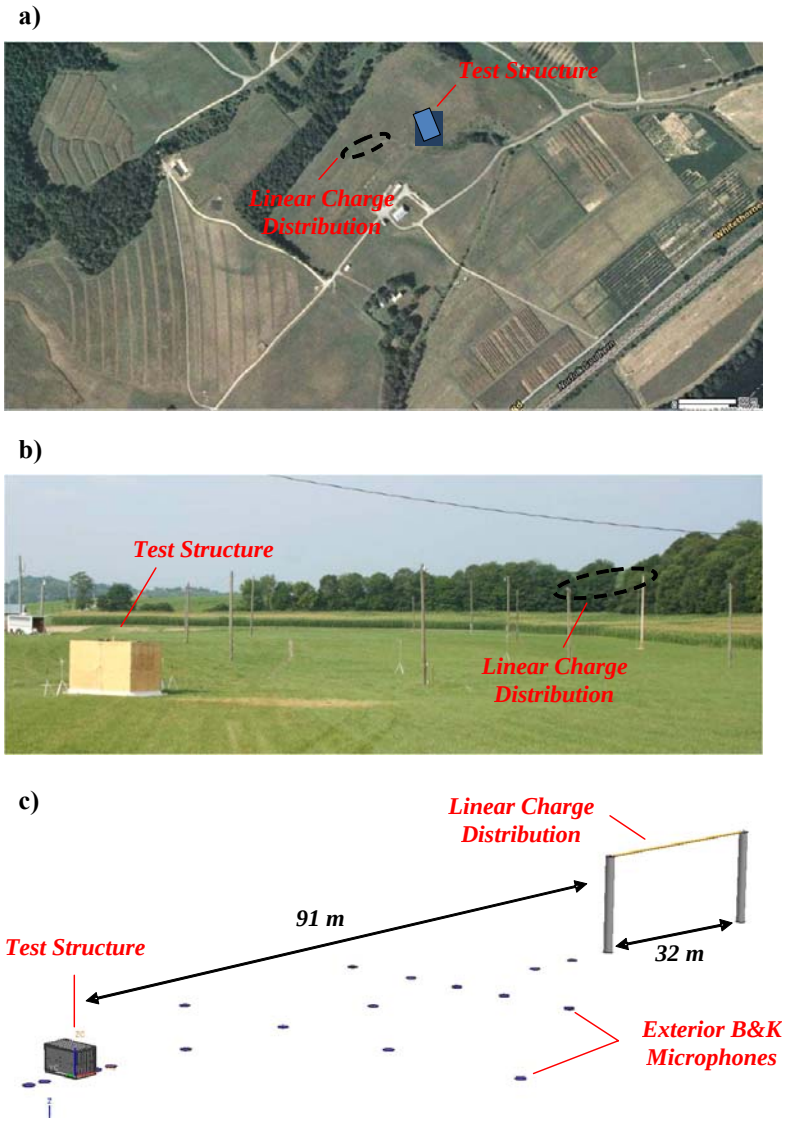

Figure 3.20: a) Aerial picture of the testing area at Kentland Farm with approximate locations of structure and linear charge distribution (not to scale), b) picture of test structure and linear charge distribution, and c) dimensioned schematic showing structure, linear charge distribution, and placement of low-frequency B&K microphones along the boom propagation path.

c) Simulated Sonic Boom

A weak sonic boom with a realistic amplitude and duration was produced with the explosive technique successfully tested and reported by Hawkins and Hicks [27]. The technique consists in arranging a number of detonating cord strands of the types used to ignite explosives so as to produce a desired pressure distribution in the direction given by the linear charge. In that sense, the structure to be tested must be aligned with the direction of the linear charge as shown in Figure 3.20c.

The detonating charges were spanned between two poles installed in the field at a height of 10.7 m (35 feet) parallel to the ground. The linear charge was ignited at the end closer to the structure yielding a pressure wave incident to the structure with a downward trajectory. Figure 3.20b and c show a picture and schematic of the sonic boom simulator placement relative to the test structure, respectively. The poles were 32 meters (105 feet) apart and the nearest pole was 91 meters (300 feet) away from the test structure. The structure was oriented so that the surface of the wall with windows was perpendicular to the axial propagation direction of the blast. Multiple linear charge distributions were tested using cord with a loading of 5.3 g/m (25 g/ft). For each distribution, strands were cut in specific lengths, taped together to form the charge distribution, and strung between the poles using pulleys and nylon ropes. Though several single and multiple strands charge distributions ranging in length from 6.1 to 24 m were tested, Figure 3.21 shows the specific distribution used to generate the weak sonic boom. This charge distribution is the same as the one used by Hawkins and Hicks [27] but with half the loading. The

ignition end is also indicated in the figure. A picture of the linear charge distribution being detonated is shown in Figure 3.22. The resulting time history and spectrum of the pressure recorded 13 m near the structure are shown in Figure 3.23. The waveform has a duration of 140 ms, an overpressure of close to 100 Pa (2.0 psf) and a rise time of approximately 10 ms. The wave signature is not completely symmetric with a rounded bow shock and a sharp stern shock and significant high frequency content. The spectrum indicates that most of the high frequency components is in the 100-500 Hz range.

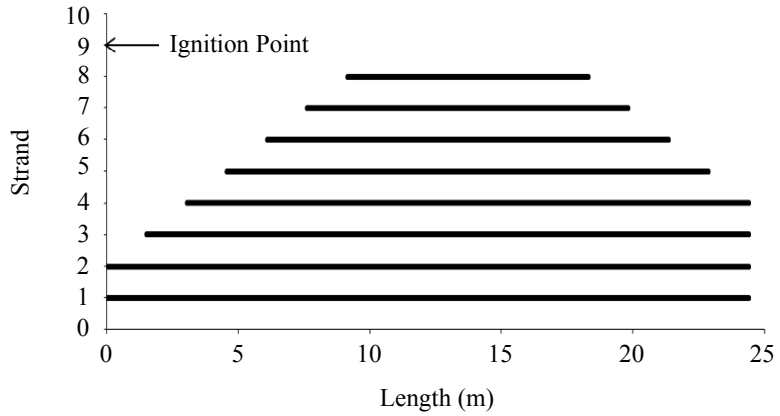

Figure 3.21: Detonating cord distribution used to produce a typical sonic boom.

Figure 3.22: Picture of linear charge distribution being detonated.

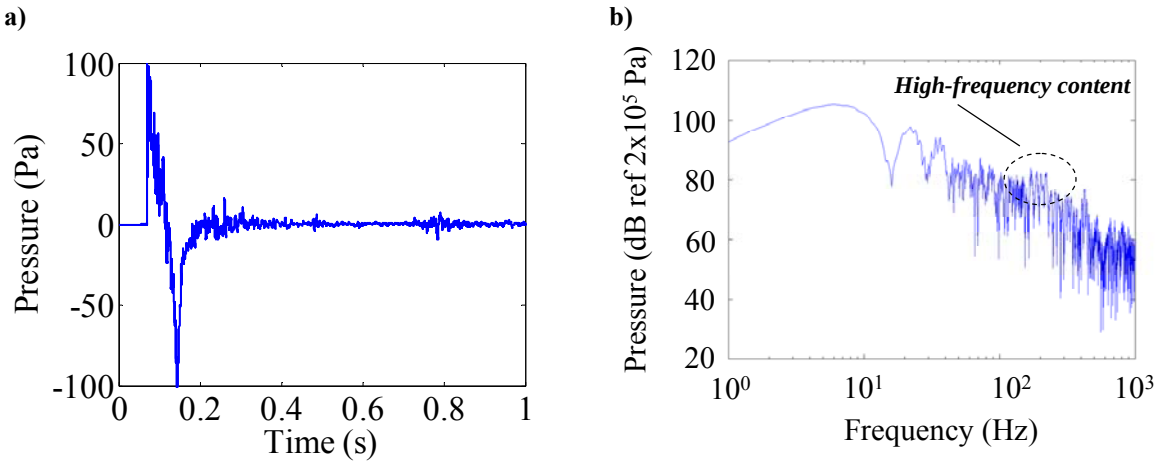

Figure 3.23: Pressure of a sonic boom recorded 13 m from the structure; a) time history and b) magnitude of the FT.

d) Instrumentation

An array of 84 wall-mounted microphones distributed through all exterior surfaces was used to record the pressure loading on the structure. The positions of these microphones are displayed in Figure 3.24a with blue dots. The middle surface in Figure 3.24a is the ceiling of the test structure and the views shown are unfolded from this middle surface. Additionally, 14 microphones distributed in four vertical arrays as shown by the schematic in Figure 3.25 were installed in the room enclosed by the structure to monitor the acoustic response. These microphones were 1/4-inch Panasonic WM-60AY Electret microphone cartridges with a standard instrumentation amplifier conditioning circuit. The average sensitivity of the microphones was found to be 70 mV/Pa. These low cost microphones exhibit a frequency roll off starting at about 20 Hz that was digitally compensated. The propagation (including the effect of atmospheric attenuation) of the pressure wave from the linear charge to the structure was monitored with an array of high quality, pressure-field 1/2-inch Microphones (B&K Type 4193). These microphones have

a flat frequency response function down to 0.07 Hz requiring no compensation. These microphones were placed on the ground following the pattern indicated in Figure 3.20c.

An array of 150 PCB accelerometers (Model 330A) was used to measure the response of the structure, 135 of them were mounted to the inside surfaces of the structure and 15 to the exterior ones. The accelerometers were calibrated with a Brüel & Kjær Calibration Exciter Type 4294 (acceleration of 10 m/s^2 at 159.2 Hz), to ensure that the accelerometers were working properly and to determine their sensitivity. The average sensitivity was found to be 96.8 $mV/(m/s^2)$ with a maximum measurable amplitude of 49 m/s^2. The frequency responses of the accelerometers were shown to be relatively flat over a frequency range of 5 to 2200 Hz. The positions of accelerometers are displayed with red dots in Figure 3.24b. The middle surface in Figure 3.24b is the floor of the test structure and the views shown are unfolded from this middle surface.

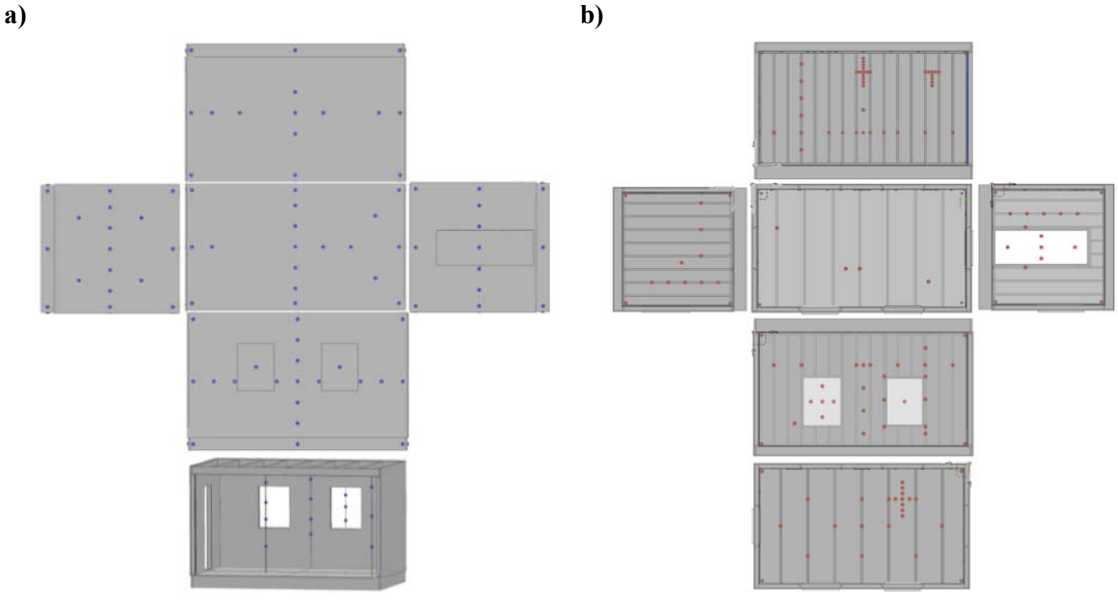

Figure 3.24: Unfolded views of the instrumented test structure, a) microphone positions on outside surfaces and b) accelerometer positions on inside surfaces.

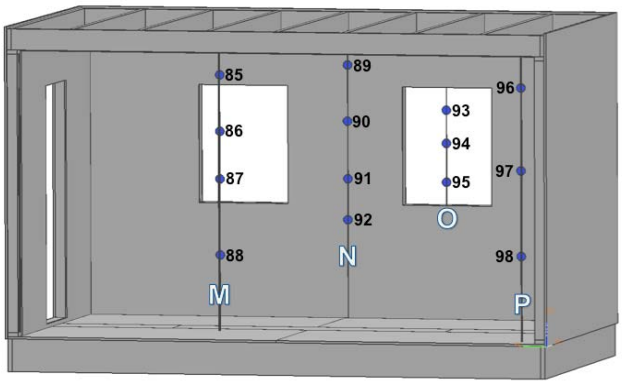

Figure 3.25: Positions and numbering of the microphones inside the single-room structure.

3.2.2 Structural Modal Properties

Figure 3.26 shows the mesh of the structure used for the finite-element calculation of the structural modal properties. The structure was discretized into 7050 shell elements (5126 nodes). The masses per unit area and equivalent orthotropic constants of the walls are reported in Table 3.3. The red and yellow nodes indicate the boundaries of window and door elements, respectively. Within these boundaries, the material is assumed isotropic with Young's modulus of 72 and 14.5 GPa, and with mass per unit area of 8 and 5.2 kg/m^2 for the window panels and doors, respectively.

Double-panel windows are modeled in the same fashion as room enclosures. The window cavity interacts with only two vibrating bodies, i.e. the two window panels. The acoustic modal properties of the window cavities were determined analytically as described below, in Section 3.2.3. The window panels were modeled as two separate sets of shell elements. The nodes of these elements shared the same physical coordinates because the rest of the structure is also modeled with two-dimensional shell elements. In

the finite-element model, it is assumed that there is continuity of the displacement and rotation at the junction of the windows and the front wall, and also at all the wall edges. At the junction of the door and the side wall, the continuity of the rotation is relaxed (only continuity of the displacement is enforced). At the locations of the cinderblocks supporting the structure, black nodes in the figure, the displacement along the three Cartesian directions is constrained to zero.

For the structural-acoustic model, 800 structural modes were computed, which covers a frequency range of 0 to 180 Hz. Note that the number of modes included in the model is limited by the computing capabilities of MATLAB. This issue could easily be overcome by using another programming language such as Fortran. The bending wavelength at 180 Hz of an infinite plate with a bending rigidity of 2000 N.m is $\lambda_b = 0.5$ m, which is at least four times the largest element length of 0.12 m. Therefore, the mesh size should be adequate to carry out the numerical simulations.

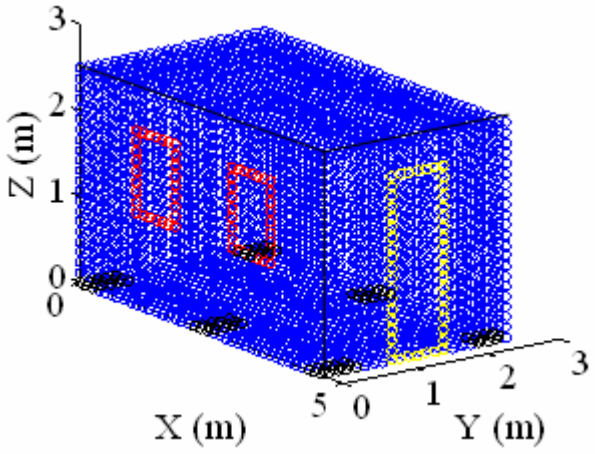

Figure 3.26: Finite-element mesh for the single-room structure.

Table 3.3: Orthotropic constants of the walls forming the single-room structure.

Wall	$m_s \left(\text{kg/m}^2\right)$	$D_x \left(\text{N.m}\right)$	$D_y \left(\text{N.m}\right)$
Front wall	29	2230	251000
Side wall with door	30.75	2210	242000
Back wall	29	2140	198000
Side wall	30.75	2140	198000
Ceiling	33	2000	824000
Floor	26.5	2280	2050000

Conventional modal testing and analysis of the structure were conducted to validate the finite-element formulation and to extract the modal damping ratios that the structural-acoustic model requires. In short, the structure was excited with an impact hammer at many locations over a rather fine grid encompassing the structure. On the other hand, accelerometers mounted on studs, close to the center of interior surfaces (walls, windows, and doors), recorded the vibration of the structure for each impact from the hammer. The modal analysis then consisted of three main steps. First, one of the accelerometers was selected as a reference for analysis. Next, the structure was assumed to demonstrate reciprocity, i.e. the response at the single reference points due to impulsive forces located on the grid of excitation points becomes the response at each point of the grid of excitation points due to an impulsive force at the location of the reference accelerometer. Finally, a curve fitting procedure (global single value decomposition) was followed to extract the eigenproperties of the structure in the frequency range of 5 to 100 Hz.

Table 3.4 reports the natural frequencies and modal damping ratios of the structure measured using conventional modal testing and the natural frequencies computed

numerically. The finite-element model predicts fairly well (less than 10% error) the natural frequencies of the structure, except for the first mode. The first mode shapes of the structure computed numerically and determined experimentally are shown in Figure 3.27 and Figure 3.28, respectively. The predicted and measured mode shapes exhibit similar characteristics. For instance, the first mode corresponds to deformations of the front and back walls, the second and third modes to deformations of the side walls, and the fourth mode to deformations of the side walls and the windows.

Table 3.4: Natural frequencies and modal damping ratios of the single-room structure measured using conventional modal testing, and natural frequencies computed numerically.

	Experimental		**Numerical**	
n	f_n^s (Hz)	ξ_n^s	f_n^s (Hz)	Error $(\%)$
1	8.84	0.0035	10.4	17.9
2	14.47	0.0194	13.1	9.1
3	17.2	0.0003	16.5	3.8
4	/	/	17.9	/
5	20.28	0.0319	20.7	2.1
6	21.6	0.001	21.0	2.9

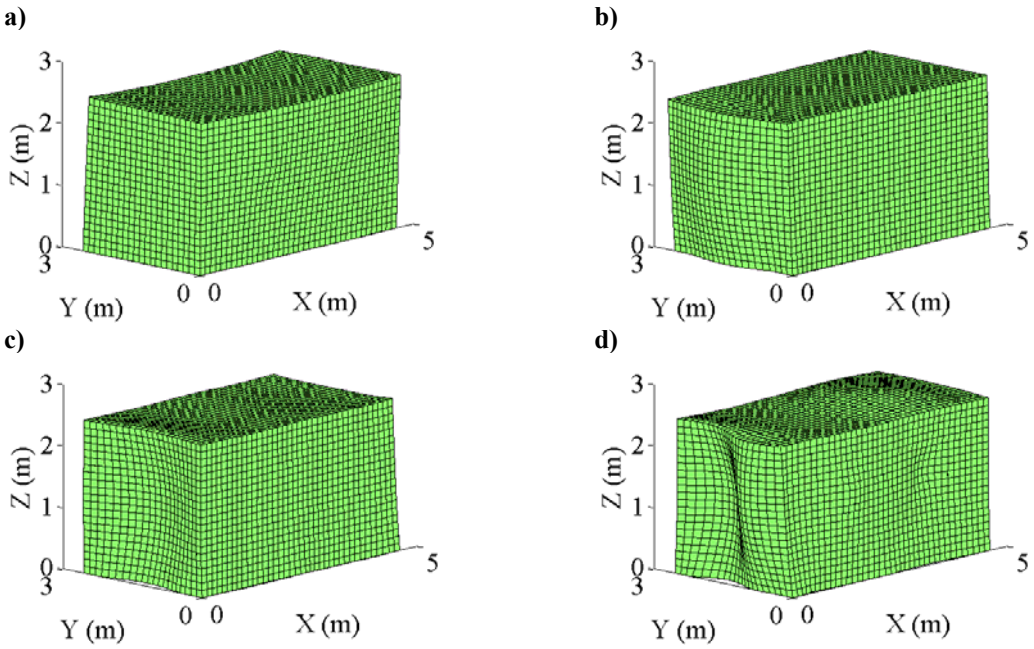

Figure 3.27: Mode shapes of the single-room structure computed numerically; modes a) n = 1, b) 2, c) 3, and d) 5.

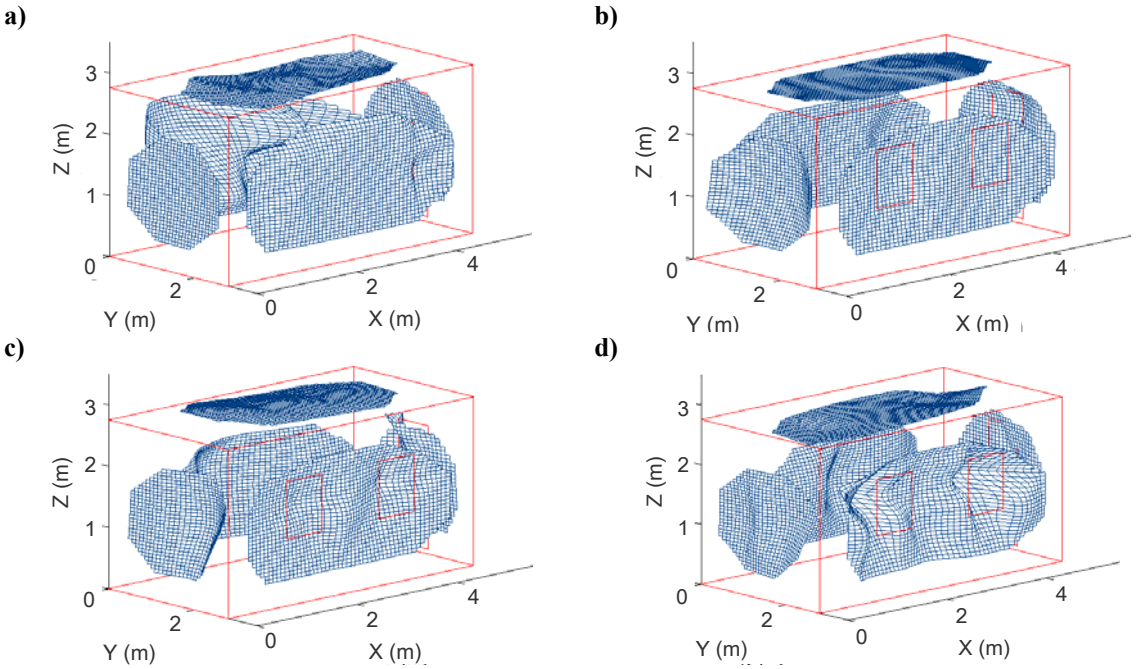

Figure 3.28: Mode shapes of the single-room structure extracted using conventional modal analysis; modes a) n = 1, b) 2, c) 3, and d) 5.

3.2.3 Acoustic Modal Properties

The acoustic system of the single-room structure is composed of three volumes, a room and two window cavities. The acoustic modal properties of the volumes were computed analytically assuming that the enclosing surfaces are perfect acoustic reflectors and using Equations (2.19) and (2.20). Experiments were conducted for validation purposes and to determine the acoustic modal damping ratios of the interior volumes. Since no measurement of the input to the acoustic system was recorded in the tests, the Natural Excitation Technique (NExT) [63] adapted to acoustic problems as reported by Corcoran et al. [57], was used to extract the modal parameters. Table 3.5 lists the natural frequencies and modal damping ratios of the room measured and computed analytically. All computed natural frequencies converged to within 3% of the measured ones, which shows the adequacy of the model. It is evident that some of the measured natural frequencies are related to the structural modes, e.g. the first acoustic mode at 15.1 Hz in Table 3.5 corresponds to the second structural mode reported in Table 3.4. Thus, the extracted modes 3, 9-13, and 16-19 are the room acoustic modes. In general, the acoustic modal damping ratios are small, e.g. less than 5%. Interestingly, there are three closely spaced, highly damped, modes at 59.2, 62.9, and 66.5 Hz with higher damping ratios, e.g. > 6%. The natural frequency at 62.9 Hz corresponds to the second acoustic mode and its damping is provided by its coupling to the structural modes. These results also indicate that the structural modes are highly damped.

Table 3.5: Acoustic natural frequencies of the room and modal damping ratios measured using the Natural Excitation Technique (NExT) and natural frequencies computed analytically.

	Experimental		Analytical	
m	$f_m^a\,(\mathrm{Hz})$	ξ_m^a	$f_m^a\,(\mathrm{Hz})$	Error (%)
1	15.1	0.038	/	/
2	22.4	0.001	/	/
3	37.6	0.027	37	1.6
4	42.1	0.033	/	/
5	45.2	0.058	/	/
6	50.5	0.043	/	/
7	55.1	0.05	/	/
8	59.2	0.061	/	/
9	62.9	0.066	61.1	2.9
10	66.5	0.065	66.5	0.0
11	70	0.058	71.4	2.0
12	74	0.049	74	0.0
13	78.2	0.043	76.1	2.7
14	82.4	0.037	/	/
15	86.9	0.032	/	/
16	91.9	0.027	90.3	1.7
17	97.1	0.025	96	1.1
18	99.1	0.086	97.7	1.4
19	102.5	0.032	99.5	2.9

3.2.4 Vibro-Acoustic Response

In this section, the predicted vibro-acoustic response of the single-room structure is compared to experimental data. The experimental signals were low-pass filtered to the frequency range of the numerical predictions, i.e. 0 – 180 Hz. Figure 3.29 and Figure 3.30 show the time histories and magnitudes of the Fourier transform (FT) of the accelerations at the center of some surfaces of the structure. The following surfaces are considered: a) front wall, b) left window, c) door, d) back wall, e) side wall without a door, and f) ceiling. In the figures and in the rest of the section, the blue and red curves correspond to the measured and predicted responses, respectively.

The windows (Figure 3.29b) exhibit larger acceleration levels than the rest of the structure. This result is in good agreement with the fact that the materials composing the windows are lighter and have less damping that the walls of the structure. Figure 3.30b indicates that the response of the windows is dominated by resonances near 15 and 20 Hz. Modal tests on the windows revealed that the resonance at 15 Hz corresponds to the fundamental mode of the window and the resonance at 20 Hz is due to the wall motion. The rest of the spectrum is at least 10 dB lower and does not contribute to the response. A shock wave incident to the front wall diffracts around the structure and leaves the back wall in a shadow zone. As a result, the acceleration levels of the back wall (Figure 3.29d) are less than half those of the front wall (Figure 3.29a). The spectra of the acceleration on the front (Figure 3.30a) and back (Figure 3.30d) walls exhibit resonances around 9 Hz, which are associated to the deformation of the front and back walls. On the front and back walls, the acceleration is under-predicted below 20 Hz by at least 10 dB. The discrepancy is most likely due to the assumptions and approximations in the modeling of the junctions between the structure subcomponents and the fact that structural responses are particularly sensitive to boundary conditions at low frequency. Another cause for the discrepancy could be errors in the experimental data due the limitations of the sensors below 20 Hz.

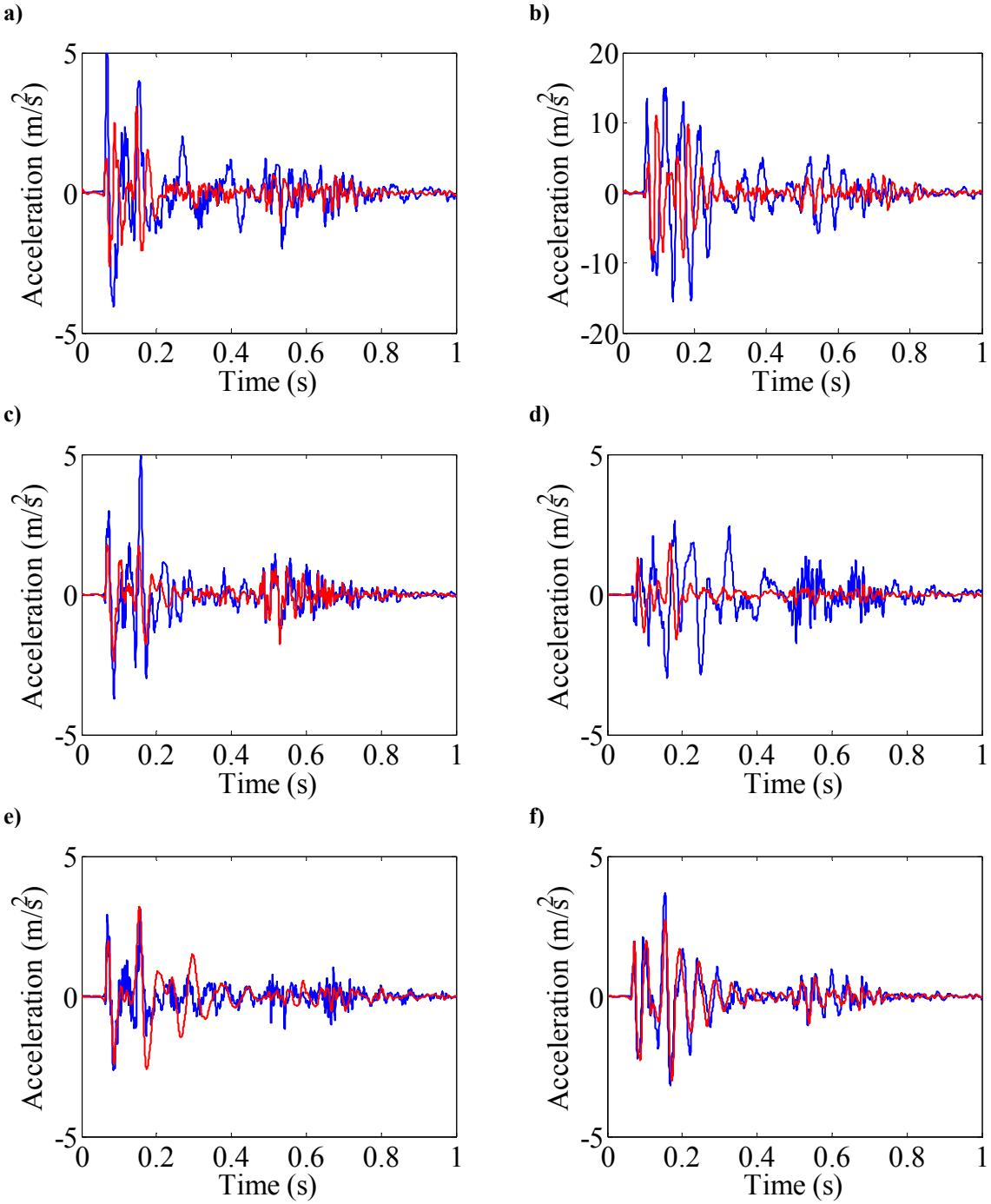

Figure 3.29: Times histories of the accelerations on the single-room structure, measured (blue line) and predicted (red line), at the center of a) front wall with windows, b) left window, c) door, d) back wall, e) side wall without door, and f) ceiling.

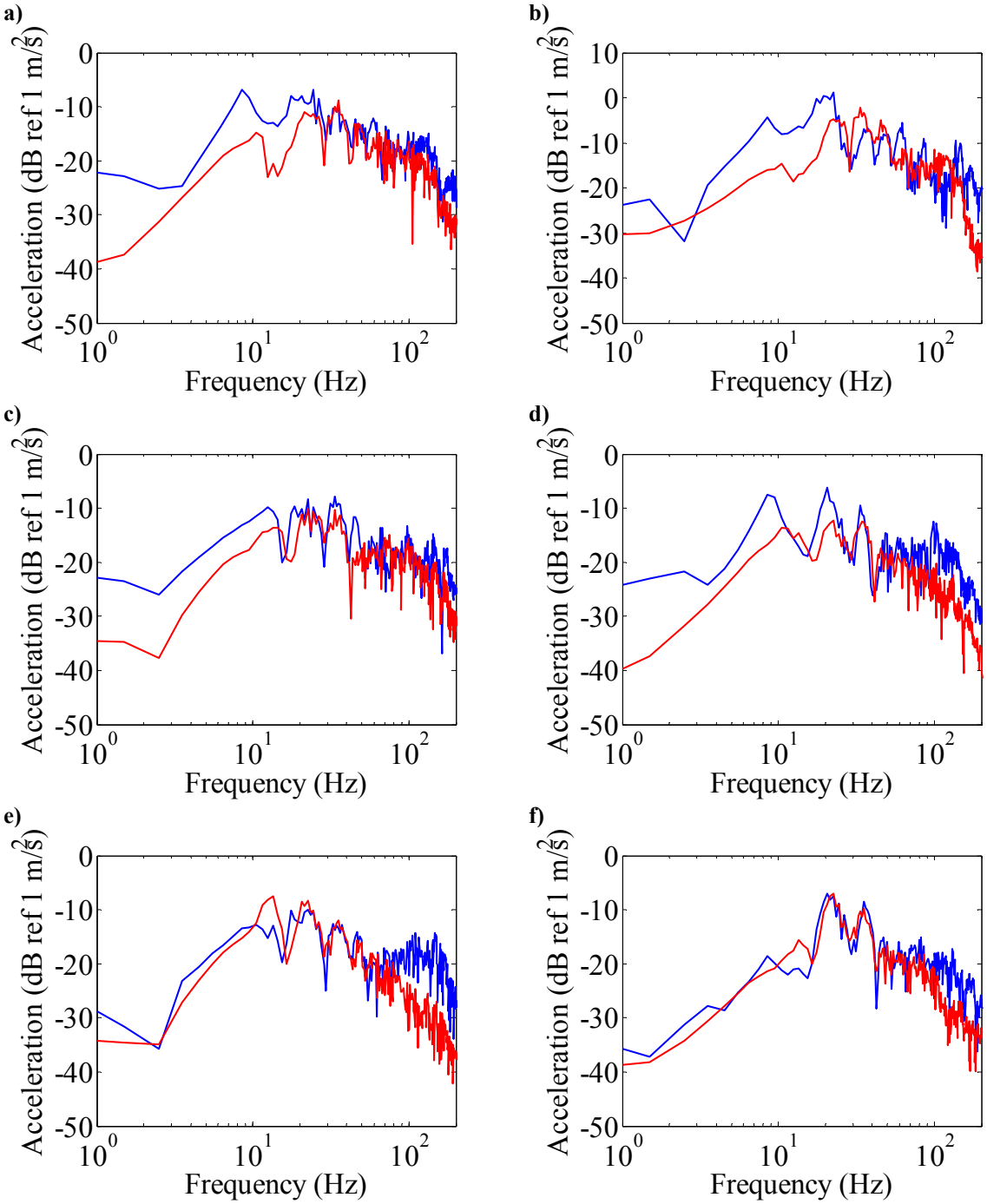

Figure 3.30: Magnitudes of the FT of the accelerations on the single-room structure, measured (blue line) and predicted (red line), at the center of a) front wall, b) left window, c) door, d) back wall, e) side wall without door, and f) ceiling.

For the type of applications targeted by this study, e.g. noise impact of sonic booms on human subjects, the interior acoustic response is the most important one. Figure 3.31 shows the time histories (left column) and magnitudes of the FT (right column) of the pressures inside the single-room structure, at the locations of interior microphones 86, 90, and 95. The interior responses at all three microphone locations are very similar, which indicates that, in this particular case, the interior acoustic response is insensitive to the observer position in the room. The pressure time histories show that the sonic boom has clearly been transmitted into the room as well as the subsequent free response. The mechanism of transmission of the boom into the building can be described as: i) the boom with a dominant frequency near 10 Hz excites the fundamental structural mode at 8.84 Hz, ii) this results in significant motion of the front and back walls, iii) that produces a pressure due to a net volume change inside the room. The reason the boom shape is relatively preserved while transmitted inside the room is that i) the boom is tuned to the fundamental frequency of the structure and ii) the interior acoustic response is due to the bulk compressibility of the cavity, i.e. no dynamics of the cavity acoustics since the fundamental frequency is near 37 Hz. The figure shows that the structure attenuates the level of the initial shock from 100 Pa (2 psf) outside to 30 Pa (0.65 psf) inside. The free response after the end of the boom is dominated by structural modes with resonances at 15 and 20 Hz, unaffected by the interior acoustic dynamics. Predictions of the pressure inside the room are in very good agreement with the experimental data. The model is successful in capturing most of the characteristics of the measured response. In the time domain, the bow of the sonic-boom-like response and the free response (after 0.2 s) are accurately predicted. The stern of the response is over-predicted by approximately 10 Pa.

In the frequency domain, this discrepancy corresponds to an over-prediction of the magnitude by approximately 4 dB in the range of 4 to 12 Hz, which is likely related to the poor microphone response below 20 Hz.

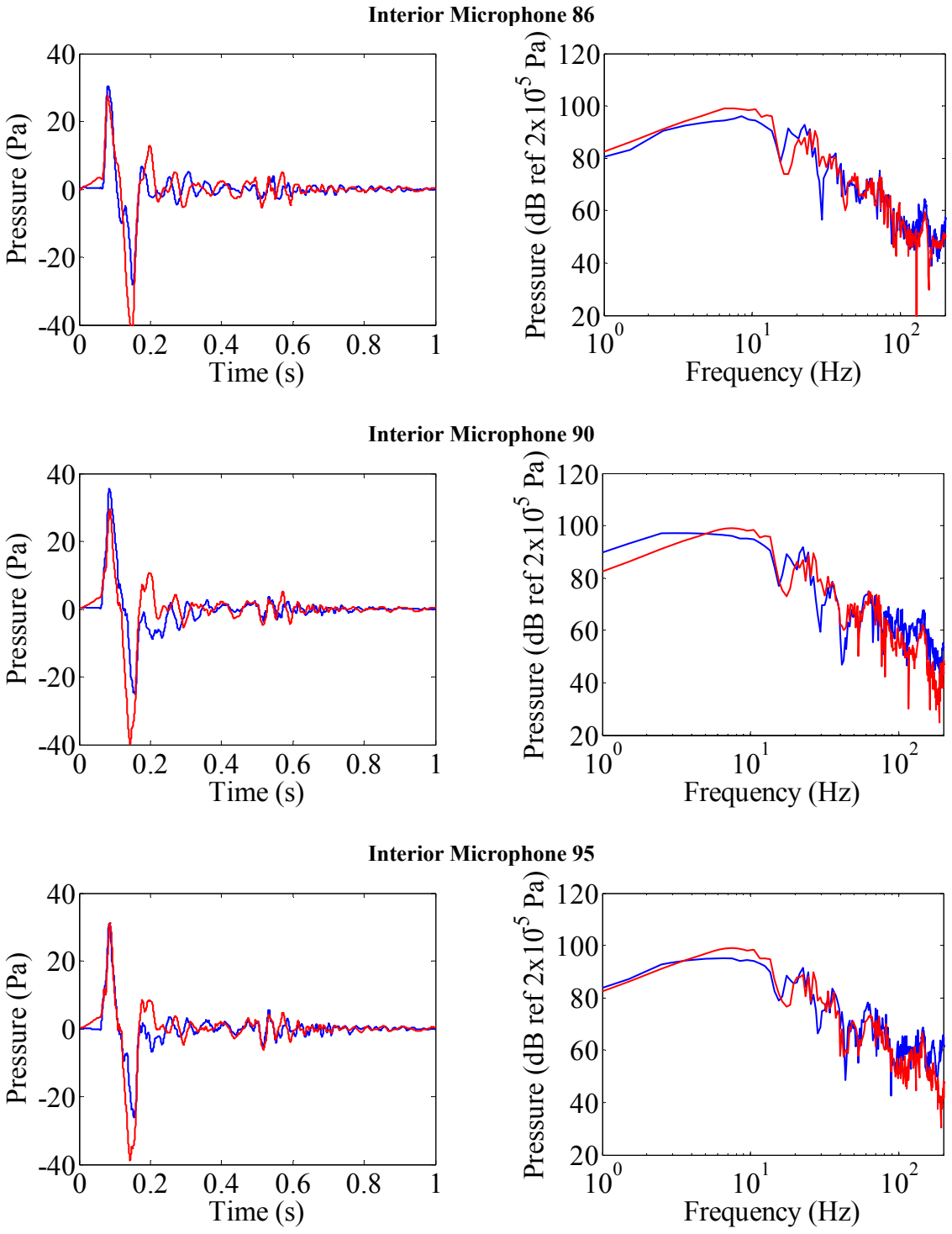

Figure 3.31: Pressures inside the room, time histories (left) and magnitudes of the FT (right), measured (blue) and predicted (red).

3.3 Two-Room Structure

3.3.1 Experimental Setup

Figure 3.32 is a photograph of the two-room structure fully instrumented and mounted on cinderblocks on the test site. The structure consists of the single-room structure (room 1) to which a room was added (room 2). Room 2 has dimensions of 2.26×4.14×2.48 m (89×163×97.5 inches), with a net volume of 23.2 m^3 (819 ft^3). The two rooms are interconnected with the same wooden door as that connecting room 1 to the exterior. In this section, both doors are kept closed so that each room of the structure is fully separated by structural components. Room 2 is fitted with a double-panel window assembly, larger than the windows on the single-room structure, with overall dimensions of 2.16×2.21 m (84×86 inches). In addition, each room is topped by an attic cavity to have a more realistic construction. For the purpose of setting up the numerical model, a given structure is decomposed in a number of surfaces (external and internal surfaces). Figure 3.33 shows the numbering of the surfaces for the two-room structure.

The external pressure loading on the structure was monitored with 94 microphones distributed over the external surfaces. The interior acoustic response of the structure was recorded with 13 microphones distributed in the rooms and attic cavities as shown in Figure 3.34. The vibration of the structure was recorded with 62 accelerometers distributed over the inside surfaces. More accelerometers were used to record the vibration of the single-room structure as local vibration effects were studied, e.g. vibration of the plaster panels in between the studs. In the case of the two-room structure, accelerometers are arranged along the wall studs only.

Structural loading was generated by the same explosive technique as that used for the single-room structure. Several distributions of detonating cords were tested, producing sonic booms with various peak amplitudes and durations. Linear charges were detonated from two locations, both approximately 90 m (300 feet) from the structure. From the first location (blast site 1 - Figure 3.35a), the boom measured 13 m from the structure had a duration and a peak amplitude of nearly 140 ms and 100 Pa (2 psf), respectively. From the second location (blast site 2 - Figure 3.35b), the duration and peak amplitude were nearly 140 ms and 110 Pa (2.3 psf), respectively. For illustration purposes, the time history and spectrum of a sonic boom generated from blast site 2 and recorded 13 m from the structure are shown in Figure 3.36.

Figure 3.32: Photograph of the two-room structure.

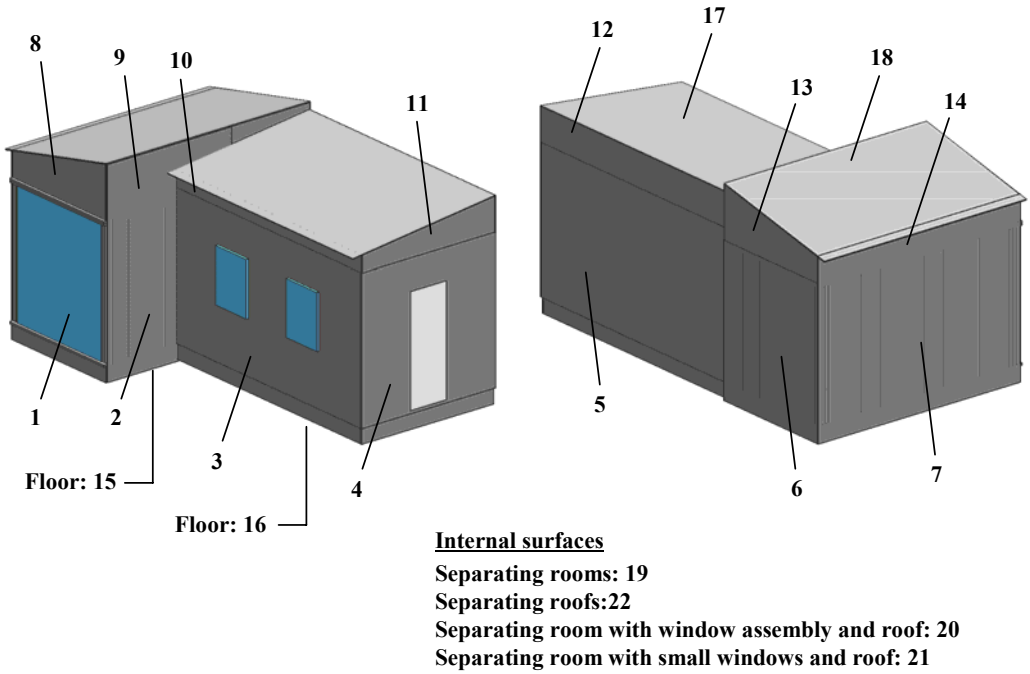

Figure 3.33: CAD drawings of the two-room structure showing the numbering of the surfaces.

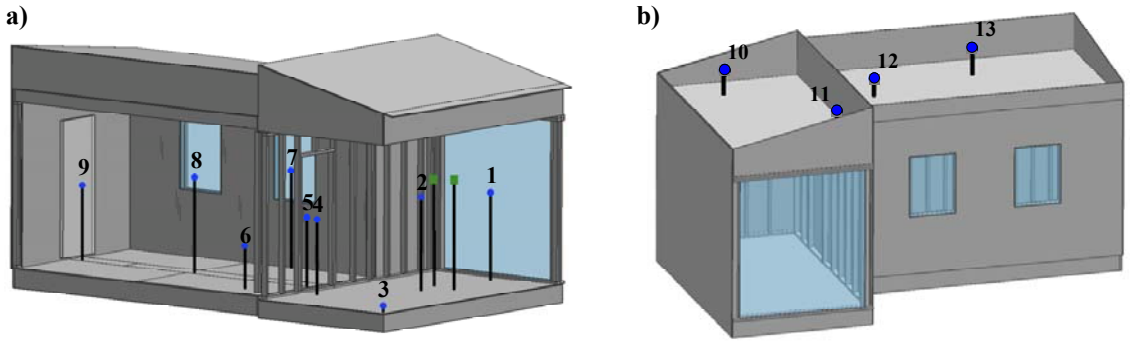

Figure 3.34: Position and numbering of the microphones inside the two-room structure, a) in the two rooms and b) in the attic cavities.

a)

b)

Figure 3.35: Photographs of the linear charges being detonated near the two-room structure from two positions, a) blast site 1 and b) blast site 2.

a) **b)**

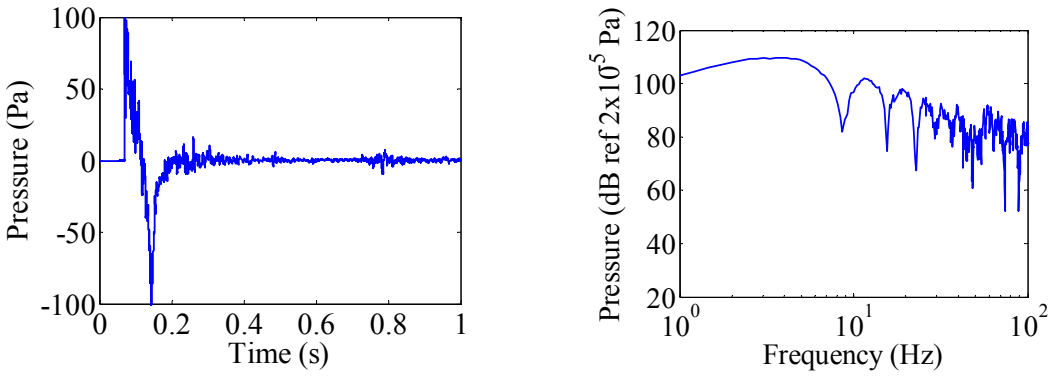

Figure 3.36: Pressure from the linear charge detonated at blast site 2 and recorded 13 m near the structure; a) time history and b) magnitude of the FT.

3.3.2 Finite-Element Modeling of the Structure

The two-room structure was discretized into 3583 shell elements (3434 nodes). The resulting mesh is shown in Figure 3.37. The same color code as for the single-room structure is used in this figure. The two-room structure includes some internal surfaces whose nodes are indicated in green in the figure. The masses per unit area and orthotropic constants of the walls forming the structure are reported in Table 3.6. The first surface (wall 1) consists of an assembly of three double-panel windows with a vinyl frame forming the boundaries of this assembly. The assembly was modeled as three separate double-panel windows with three cavities, in the same fashion as for the windows of the single-room structure. The panels of the windows and the frame of the window assembly were assumed isotropic materials with the properties of glass and vinyl, respectively. At the locations of the doors (within yellow boundaries), when the door is closed, the material is assumed isotropic with a Young's modulus of 14.5 GPa and with a mass per unit area of 5.2 kg/m^2. The roof of the structure is modeled as an equivalent rectangular cavity, to accommodate for the model limitations, i.e. rectangular room geometries.

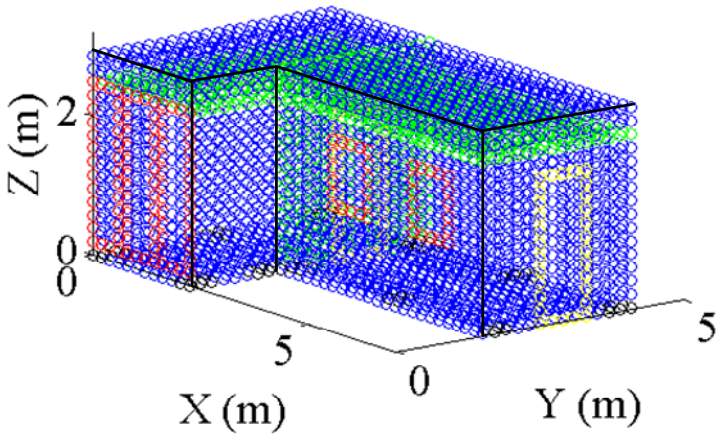

Figure 3.37: Finite-element mesh of the two-room structure.

Table 3.6: Masses per unit area and orthotropic constants of the walls forming the two-room structure.

Wall	$m_s\left(\text{kg/m}^2\right)$	$D_x\left(\text{N.m}\right)$	$D_y\left(\text{N.m}\right)$
1	5.7	/	/
2	24.0	616	139000
3	28.9	2230	233000
4	30.8	2190	227000
5	28.9	2140	198000
6	24.0	615	137000
7	24.0	620	148000
8	7.6	2000	2000
9	7.6	2000	2000
10	7.6	2000	2000
11	7.6	2000	2000
12	7.6	2000	2000
13	7.6	2000	2000
14	7.6	2000	2000
15	26.5	679	1050000
16	26.5	2280	2050000
17	17.9	5430	153000
18	17.9	5430	153000
19	25.1	292	161000
20	33.0	285	1040000
21	33.0	285	1040000
22	15.2	1249	4000

Because of the relatively large size of the two-room structure, it is believed that hits to the structure made with an impact hammer may not be sufficient to excite the structure into global motion and capture the low-frequency structural modes. Due to this fact, the structural response to a simulated sonic boom, in which global motion is attained, was used along with the Natural Excitation Technique (NExT) [57,63] to extract the modal properties of the two-room structure. This is an output-only modal analysis (unknown input), which consists of the following steps. First, a reference accelerometer was selected and cross-correlations were calculated between all structural response signals and this reference signal. The second halves, starting from zero lag, of these cross-

correlations were considered to be the impulse response functions (IRFs) of the structure due to an input at the location of the reference accelerometer. The IRFs were then converted to FRFs simply by calculating the Fast Fourier Transform of each IRF. Last, once the FRFs are calculated, the same curve fitting procedure as in conventional modal analysis is used to extract the eigenproperties of the structure in the frequency range of 5 to 100 Hz.

Table 3.7 reports the natural frequencies and modal damping ratios of the two-room structure obtained experimentally and the natural frequencies computed numerically. Figure 3.38 and Figure 3.39 show the first mode shapes of the structure computed numerically and determined experimentally, respectively. Note that many modes computed numerically correspond to the motion of the floor or roof, e.g. modes 2 and 3. These surfaces were not considered in the experimental modal analysis. Therefore, modes computed numerically are compared to those determined experimentally based on the overall shape of the deformation. The modes depicted in the figure correspond mainly to the deformation of the window assembly acting like a single large plate and to the deformation of the side wall next to the window assembly. These two components exhibit significantly larger displacement than the rest of the structure and thus are expected to be the main transmission path of the sonic booms from the outside to the inside of the structure. The natural frequency of the first mode is fairly well predicted (6.6% error). However, natural frequencies of modes 4, 5, and 6 are over-predicted and exhibit large errors. The cause for this discrepancy is still under investigation. The modes 18, 19, and 20 mainly correspond to the deformation of the wall with the smaller windows but are not

shown here, for the sake of conciseness. The natural frequencies of these modes are again fairly well predicted (less than 5% error).

Table 3.7: Natural frequencies and modal damping ratios of the two-room structure extracted using NExT, and natural frequencies computed numerically.

	Experimental		**Numerical**	
n	f_n^s (Hz)	ξ_n^s	f_n^s (Hz)	Error (%)
1	7.0	0.0817	7.5	6.6
2			11.4	
3			12.3	
4	8.1	0.0079	12.5	54
5	8.3	0.0507	12.9	56
6	9.9	0.0312	13.4	35
7			13.7	
8			13.9	
9			15.0	
10			15.1	
11			16.2	
12			17.4	
13			17.5	
14			18.1	
15			18.2	
16			18.8	
17			19.3	
18	20.2	0.0276	20.1	0.2
19	20.8	0.0174	20.4	1.7
20	21.5	0.0048	20.5	4.6

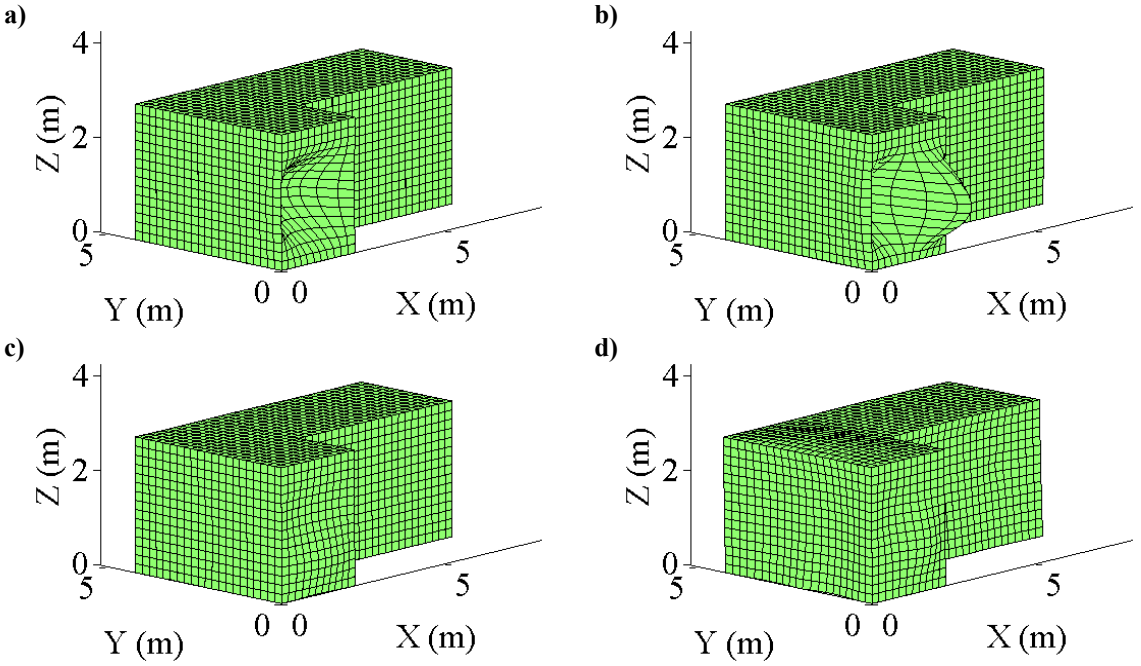

Figure 3.38: Mode shapes of the two-room structure computed numerically; modes a) n = 1, b) 4, c) 5, and d) 6.

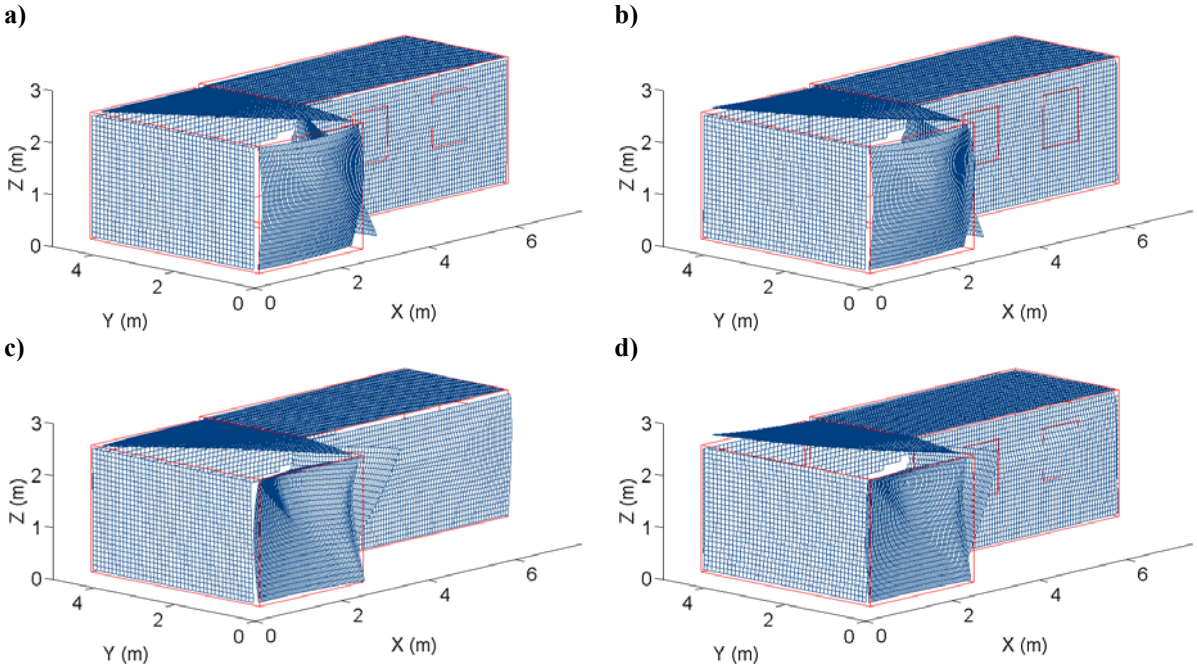

Figure 3.39: Mode shapes of the two-room structure extracted using NExT; modes a) n = 1, b) 4, c) 5, and d) 6.

3.3.3 Vibro-Acoustic Response

Given the number of surfaces on the two-room structure and the fact that the case of the single-room structure was validated in Section 3.2, predicted structural responses are compared to measured ones for surfaces of room 2 only. Figure 3.40 and Figure 3.41 show the accelerations, time histories (left column) and magnitudes of the FT (right column), at the center of some surfaces of room 2 for sonic booms generated from blast sites 1 and 2, respectively. In the figures and in the rest of the section, the blue and red curves correspond to the measured and predicted responses, respectively. Note that experimental data were filtered to the frequency range of the numerical predictions, i.e. 0 to 100 Hz.

The spectra in the figures indicate that below 10 Hz, for both blasts, the structural response is dominated by the vibration of the window assembly (face 1). In this frequency range the magnitude of the response is at least 10 dB higher than for the rest of the structure. This result is consistent with the experimental modal analysis (Figure 3.39), where the first mode at 7 Hz corresponds to the motion of the window assembly. It would be expected that the window assembly exhibits the largest amplitude because of its low mass and damping, and relatively large size. Surprisingly, some walls vibrate with equal or larger amplitudes, e.g. face 2. This is particularly true when the window assembly is in the shadow zone of the diffracted wave, i.e. for a sonic boom generated from blast site 2. The response of face 2 is dominated by a mode in the range of 20 to 25 Hz. Results from the experimental modal analysis show that displacement of this wall is observed in this frequency range, which corresponds to modes 18 to 20. The figures also indicate that the

overall structural response is fairly sensitive to the location from which the booms are generated.

Numerical predictions of the structural response are now compared to experimental data. For a boom produced from blast site 1 (Figure 3.40), the numerical model under-predicts the magnitudes of the dominant modes for the window assembly and the wall of face 2, below 10 Hz for the window and in the range of 20 to 40 Hz for face 2. The response of the window assembly is over-predicted above 10 Hz from this boom location. The model predicts fairly well the vibration of the other two walls (face 7 and face 19). For a boom produced from blast site 2 (Figure 3.41), numerical predictions are in much better agreement with experimental data for all surfaces. The reason for the discrepancies in the validation results between the two boom locations is not clearly determined yet. One possible reason could be some non-linear effects the model does not capture when the window assembly is directly facing the boom (blast site 1) because of the large amplitude and high-frequency content of the incident wave. Finally, it should be pointed out that most predicted spectra (red curves – right columns) exhibit a peak around 3 Hz. This effect is still unexplained as this frequency does not correspond to any natural frequency of either the structural or acoustic systems.

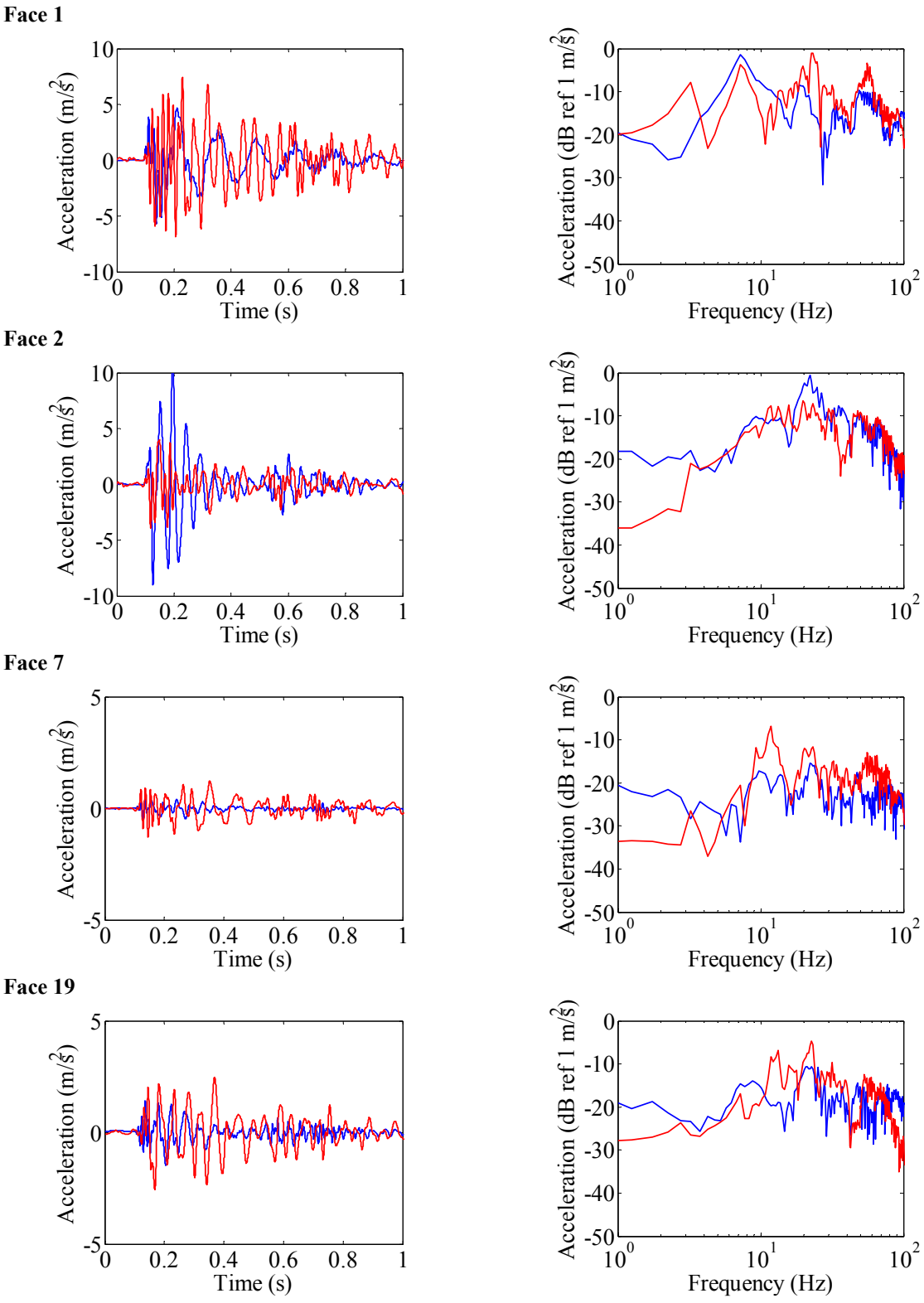

Figure 3.40: Acceleration on some surfaces of the two-room structure, time histories (left) and magnitudes of the FT (right), measured (blue) and predicted (red), due to a sonic boom produced from the first detonating location (blast site 1).

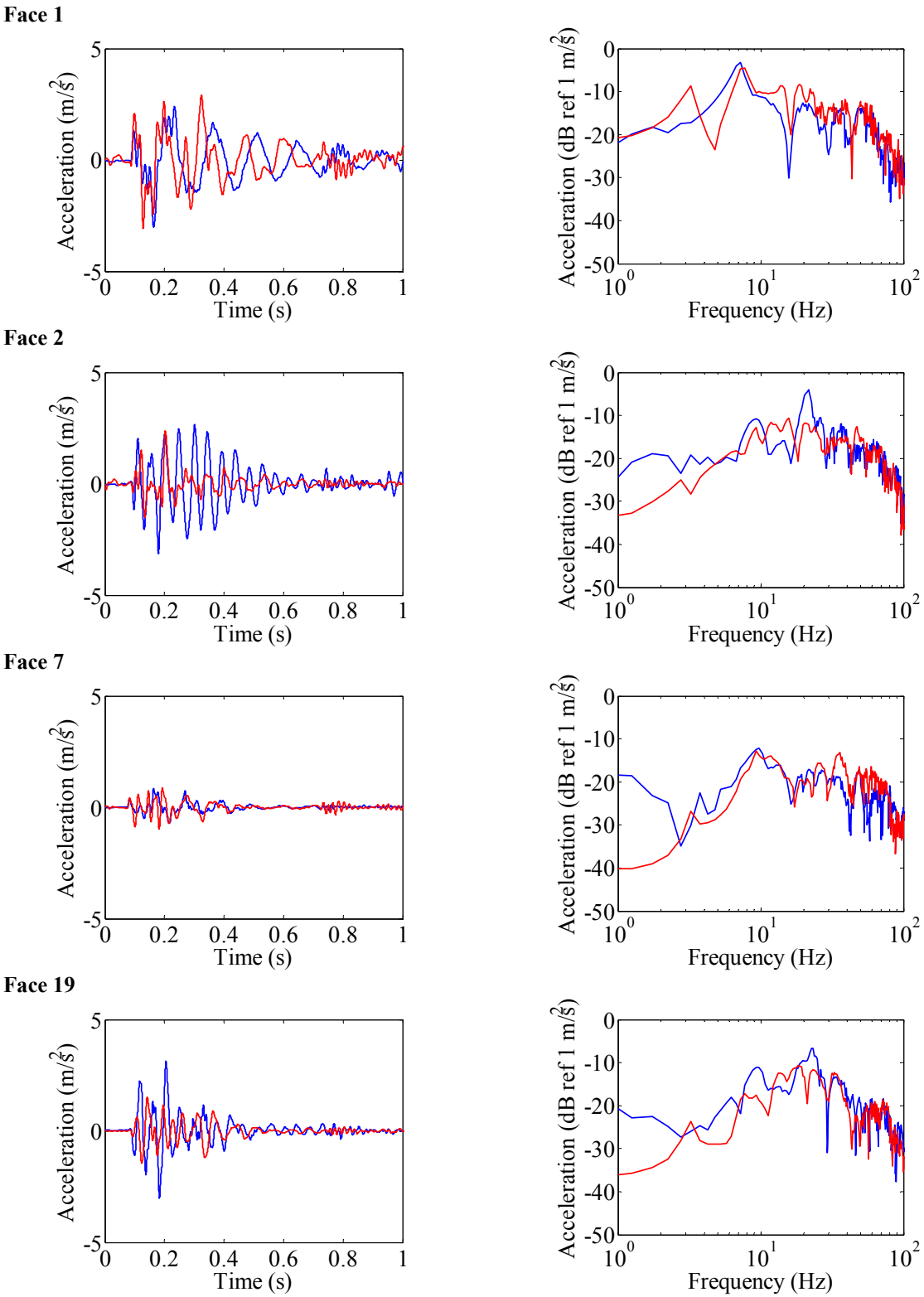

Figure 3.41: Acceleration on some surfaces of the two-room structure, time histories (left) and magnitudes of the FT (right), measured (blue) and predicted (red), due to a sonic boom produced from the second detonating location (blast site 2).

Figure 3.42 and Figure 3.43 show the pressures, time histories (left column) and magnitudes of the FT (right column), inside the two-room structure for sonic booms generated from blast sites 1 and 2, respectively. Results are shown at three microphone locations, near the center of room 2 (microphone 2), near the exterior door of room 1 (microphone 9), and in the attic above room 2 (microphone 10).

First, it is interesting to notice that the interior acoustic response is very sensitive to the location inside the structure and varies significantly from one volume to the other. This is directly a result of the difference in the geometries of the interior volumes and also differences in the structural components enclosing the volumes, e.g. two small windows and a door for room 1, a large window assembly for room 2, and stiffened panels for the roof. The spectrum of the response at the center of room 2 is dominated by a component around 7 Hz, which corresponds to the fundamental mode of the window assembly. As expected, this dominant component is not observed in the response of the room 1 because the rooms are not interconnected, i.e. closed door. Rather, a resonance can be observed around 20 Hz, which corresponds to the motion of the front wall of room 1 with the two small windows. The pressure inside the attic has larger amplitude than inside the two rooms, as a result of the stiffened panels forming the roof being much lighter and less stiff than the walls forming the rooms.

In terms of validation of the numerical model, results on the interior acoustic response are very consistent with those of the structural response described above in the sense that numerical predictions are in much better agreement with the experimental data when the

boom is generated from blast site 2 than from blast site 1. The model is successful in capturing most characteristics of the interior acoustic responses in all volumes, except at the center of room 2 where the response is under-predicted below 20 Hz, most likely as a result of the poor microphone response below 20 Hz.

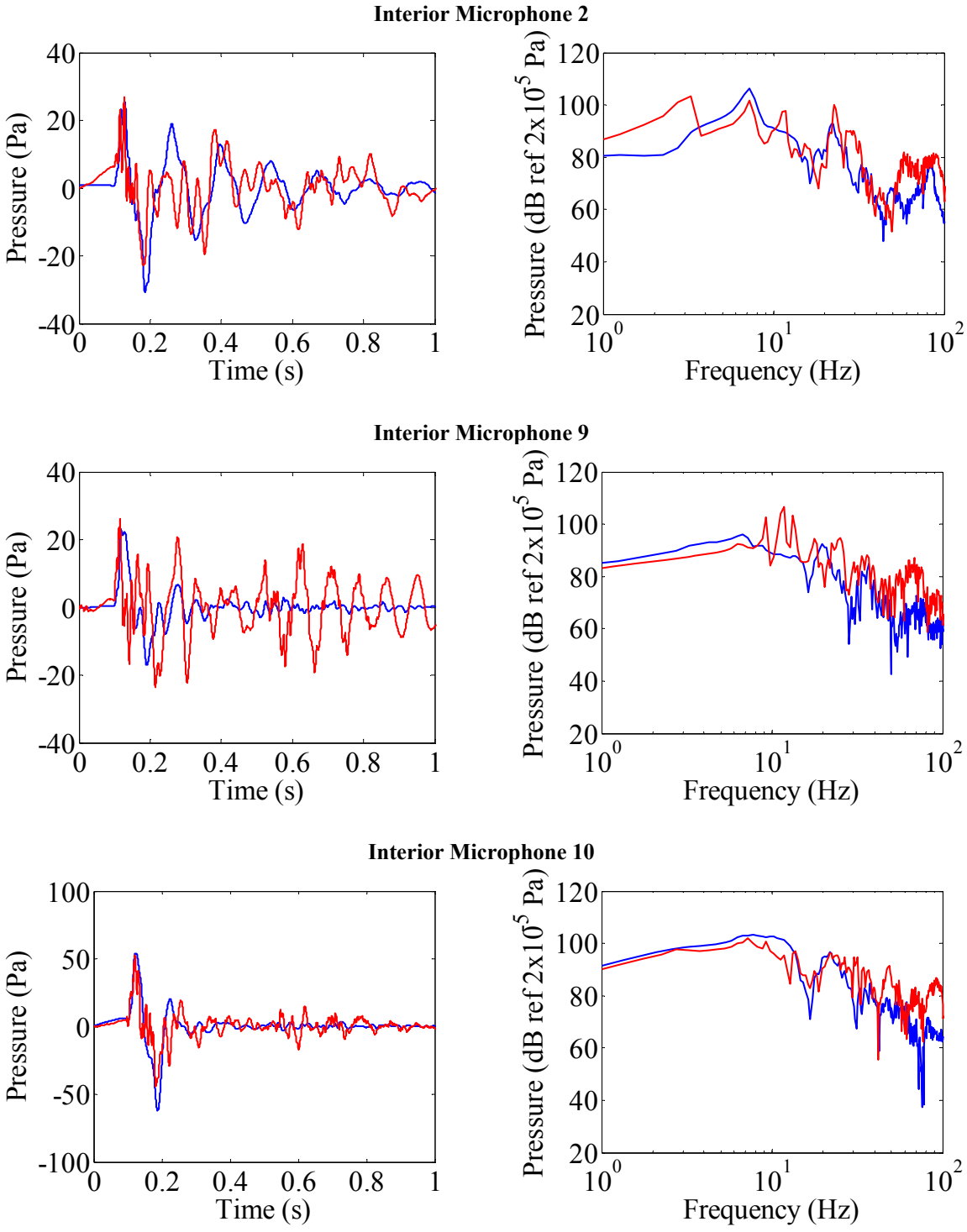

Figure 3.42: Pressures inside the two-room structure, time histories (left) and magnitudes of the FT (right), measured (blue) and predicted (red), due to a sonic boom produced from the first detonating location (blast site 1).

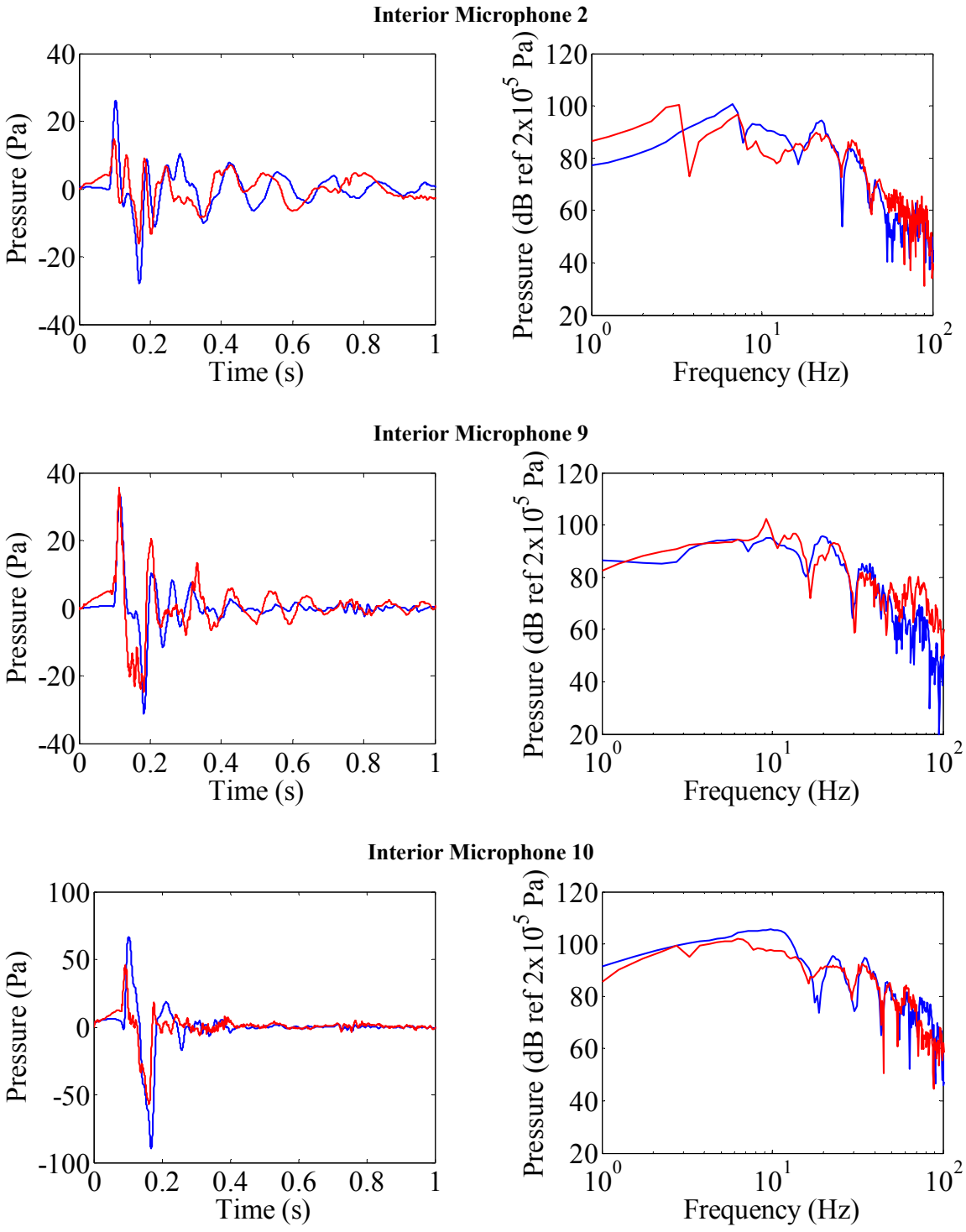

Figure 3.43: Pressures inside the two-room structure, time histories (left) and magnitudes of the FT (right), measured (blue) and predicted (red), due to a sonic boom produced from the second detonating location (blast site 2).

3.4 Room Openings

The two-room structure described in Section 3.3.1 is used to validate the novel formulation for room openings. Three configurations of the structure were tested; configuration 1: both doors closed; configuration 2: interior door open – exterior door closed; and configuration 3: both doors open.

3.4.1 Modal Analysis

The same mesh as that shown in Figure 3.37 was used to discretize the structure into shell elements. Within the boundaries of the door, the material is assumed isotropic. When a door is closed, the material is assumed to have a Young's modulus of 14.5 GPa and a mass per unit area of 5.2 kg/m^2. When a door is open, the Young's modulus for the "rigid piston" elements is set to 1000 GPa, and that of the transition elements to 10 Pa. The equivalent mass of the piston modeling the opening is 2.2 kg, so a mass per unit area of 1.6 kg/m^2.

The first 300 structural modes were computed for the structural-acoustic model, which covers a frequency range of 0 to 60 Hz. The natural frequencies of the structure with both doors open (configuration 3) are reported in Table 3.8. Figure 3.45 shows the first four modes of the structure in this configuration. These modes correspond to the motion of the openings, which clearly move as rigid bodies (pistons). Note that the external surfaces on the front of the structure were not plotted, for visualization purposes. Modes 1 and 2 show the elements of the door openings moving along the normal to the openings. Because the transition elements are also shell elements with membrane

capabilities, motion is also observed within the planes of the openings, e.g. modes 3 and 4. However these modes (3 and 4) do not affect the interior acoustic response because only the normal structural displacement is a source term to the acoustic equations. Modes 5 to 10 are similar to modes 3 and 4, and thus are not plotted. The resonant frequencies of these modes are all below 1 Hz. Modes 11 and 14 reported in Table 3.8 correspond to the motion of the window assembly, i.e. modes 1 and 4 in Figure 3.38.

Table 3.8: Natural frequencies of the structure with both doors open (configuration 3) computed numerically.

n	f_n^s (Hz)
1	0.3
2	0.3
3	0.5
4	0.5
5	0.6
6	0.6
7	0.6
8	0.6
9	0.7
10	0.7
11	7.5
12	11.4
13	12.3
14	12.5
15	12.9

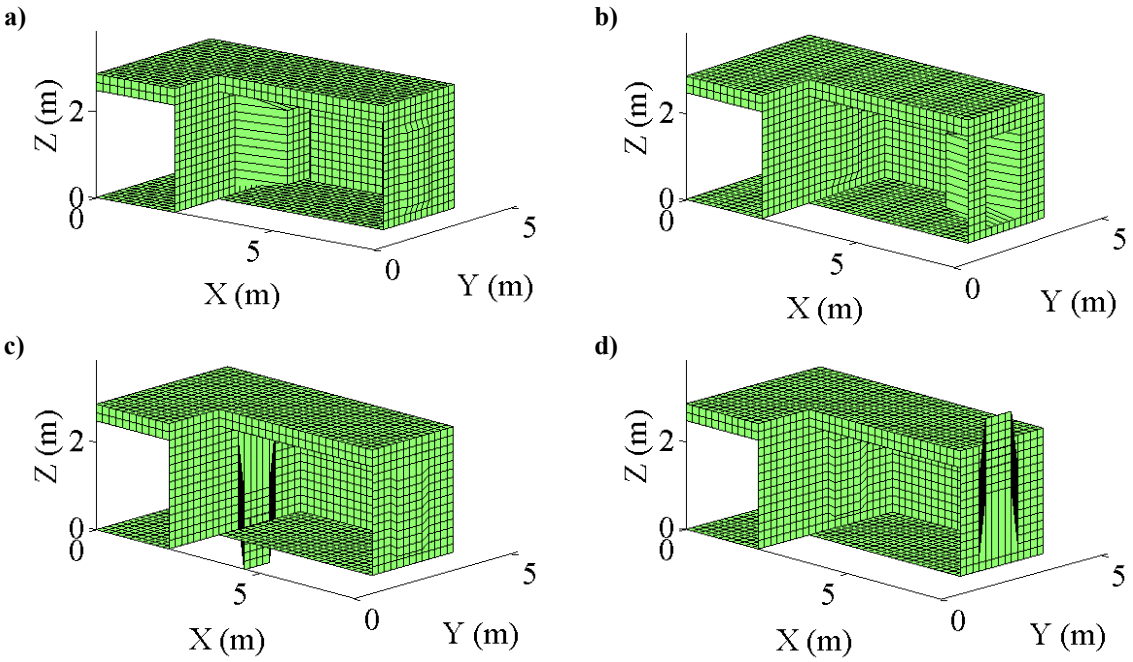

Figure 3.44: Modes shapes of the two-room structure with both doors open (configuration 3) computed numerically; modes a) n = 1, b) 2, c) 3, and d) 4.

Corcoran [57] modeled the structure in configurations 2 (open-closed door) and 3 (open-open door) as single- and two-degree of freedom systems, respectively. Schematics of these Helmholtz resonator systems are reproduced in Figure 3.45. The stiffness constants of rooms 1 and 2 are k_1 = 10 and k_2 = 13.4 kN/m. Both openings have the same equivalent mass of m = 2.2 kg. The resonant frequency of the room in configuration 2 is then equal to 16.6 Hz. The room in configuration 3 has two resonant frequencies, at 7.39 and 18.35 Hz. These frequencies are smaller than the first acoustic natural frequencies of rooms 1 and 2 with perfectly reflecting surfaces, computed at 36 and 41 Hz, respectively. Note that the natural frequency of the structural mode 11 is very close to the first Helmholtz resonance at 7.39 Hz when both doors are open. Therefore, strong coupling between the window assembly and the room acoustics is expected around this frequency.

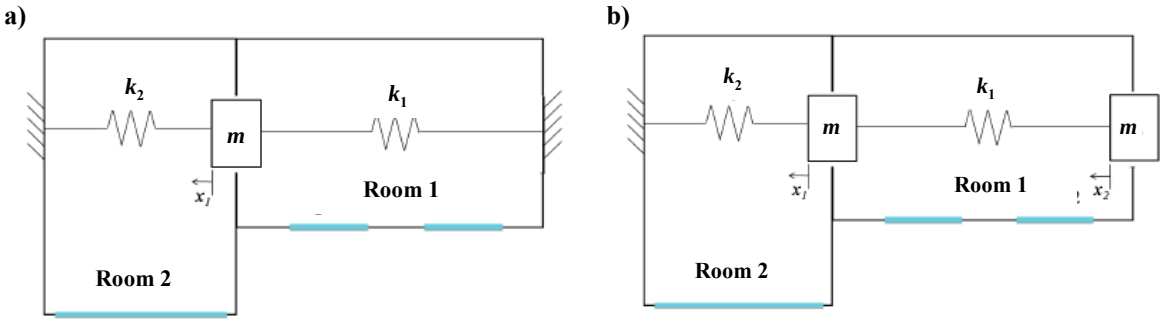

Figure 3.45: Schematic of the structure in configurations 2 and 3.

Conventional spectrum measurement of the room acoustics was carried out to detect the Helmholtz resonances of the rooms, for various door configurations of the structure. A speaker playing pink noise was successively placed in a corner of room 1 and room 2. On the other hand, two microphones were placed in a corner of each room to record the pressure fluctuation. The pressure spectra measured by the microphone in room 1 while the speaker was in the same room for the three different door configurations are plotted in Figure 3.46a) and the pressure spectra measured in room 2 while the speaker was in that room is plotted in Figure 3.46b).

First examining Figure 3.46a) for room 1, the most obvious difference in door configurations occurs at low frequencies. From 1 to 30 Hz, the spectrum measured when both doors are open demonstrates strong resonances from 5 to 7 Hz and again around 22 Hz. From the calculations performed previously, it can be seen that these resonances are close to the natural frequencies of the two rooms when treated as Helmholtz resonators, indicating that this effect is significant at low frequency when the doors are opened. Another major difference occurs between the blue and the red curves around 6 Hz; when the interior door is open, the spectrum jumps up about 6 dB. This can be explained by the

fundamental structural mode found previously in the structural modal analysis. It was shown that this mode corresponds primarily to the motion of the large window assembly of room 2 and when the door is closed, the microphone in room 1 does not sense the sound radiated from the vibration of this mode well. Other than those key differences at low frequencies, the spectra are virtually the same above 35 Hz, indicating little change in the acoustic nature of the rooms when doors are open or closed. This result suggests that the mass of the air in an opening only couples interconnected rooms when the acoustic wavelength is greater than the characteristic length of the opening (about 1.5 m), which correspond to the critical frequency of 35 Hz.

Looking at Figure 3.46b) for room 2, again the large jump in magnitude due to the Helmholtz resonator effect is demonstrated by the black curve. However, now the difference in magnitude between the blue and red curves around 6 Hz is not nearly as great as measured in the room 1. In fact, the level is higher when the interior door is closed due to the pressure build-up from the wall assembly vibrating in its fundamental mode in room 2. Additional differences in magnitude in the 10 to 30 Hz frequency-range can be explained by structural modes, such as the resonance occurring in the red curve at about 20 Hz, which corresponds to the motion of the large wall of room 1 with the two small windows. In room 2, the Helmholtz resonance for rooms in configuration 2 (red curve) can be clearly seen around 13 Hz, which is close to the predicted value of 16.6 Hz. Again, the curves come in close agreement past 35 Hz, thus reinforcing the lack of mechanical coupling (Helmholtz resonator behavior) between rooms at wavelengths smaller than the characteristic length of the opening.

Both figures indicate that the transition occurring at the critical frequency of 35 Hz is rather abrupt. Therefore, in future research, it would be a reasonable assumption to model the frequency-dependent properties of room openings using step functions, as described in Section 2.6 (see Figure 2.8). In this study, the acoustic responses of interconnected rooms are computed below the critical frequency only, where the opening properties are not frequency dependent.

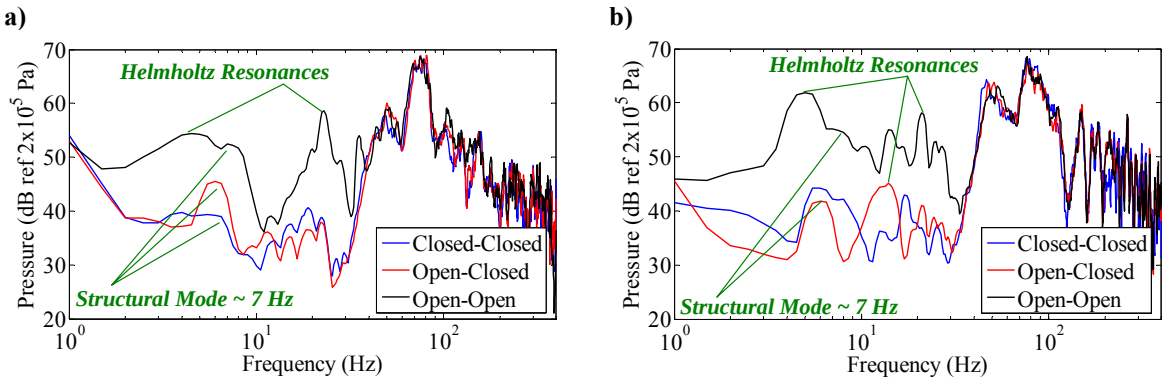

Figure 3.46: Magnitudes of the FT of the pressures measured in a corner of a) room 1 and b) room 2, due to pink noise being played through a speaker in an opposite corner of the same room for three door configurations.

3.4.2 Interior Acoustic Response to a Sonic Boom

Figure 3.47 shows the magnitudes of the FT of the pressures, at the locations of interior microphones 2 (center of room 2), 5 (in room 1, close to the doorway of the interior door), and 9 (in room 1, close to the doorway of the exterior door). Results are shown for the three configurations of the structure; configuration 1 (left column), configuration 2 (center column) and configuration 3 (right column). In the figures, the annotations SR and HR refer to structural and Helmholtz resonances, respectively. The blue and red curves correspond to the measured and predicted responses, respectively.

a) Configuration 1: closed-closed

Below the fundamental acoustic resonance of a room (36 Hz for room 1 and 41 Hz for room 2), the response of the room is due to the bulk compressibility, i.e. no dynamics of the cavity acoustics. The resonances observed in this frequency range are thus those of the structural modes producing a net change of volume in the room. The spectrum of the acoustic response at the center of room 2 (microphone 2) is dominated by the structural mode around 7 Hz, which corresponds to the motion of the window assembly. As seen before, this dominant component is not observed in the response of room 1, e.g. microphones 5 and 9, because rooms 1 and 2 are not interconnected. Rather, a resonance can be observed around 20 Hz, which corresponds to the motion of the large wall of room 1 with the two small windows.

b) Configuration 2: open-closed

The acoustic responses to sonic booms of the rooms in configuration 2 (center column) are significantly different from those in configuration 1 (left column), in particular below 20 Hz. The experimental measurements (blue) show clearly the Helmholtz resonance around 13 Hz, in both rooms. The model (red) also predicts a Helmholtz resonance, which can be clearly seen at the three microphone positions but at lower frequency, around 11 Hz. In addition, the structural resonance around 7 Hz that cannot be seen in room 1 when the interior door is closed has now been transmitted into room 1. This mechanism is also predicted by the model since a resonance can observed at the location of microphones 5 and 9, around 5 Hz.

c) Configuration 3: open-open

The acoustic responses of the rooms in configuration 3 (right column) clearly show the first Helmholtz resonance around 4 Hz, both experimentally and numerically, at the three microphone positions. The second Helmholtz resonance around 22 Hz can be observed experimentally by microphones 2 and 5 but not in the predictions. The second Helmholtz resonance is most likely predicted by the model but its frequency might be too close to the resonance of the large wall in room 1 with the small windows, which dominate the acoustic response around this frequency. Again, with both doors open, the structural resonance of the large window assembly around 7 Hz can now be observed in the acoustic response of room 1, around 7 Hz experimentally and around 5 Hz numerically.

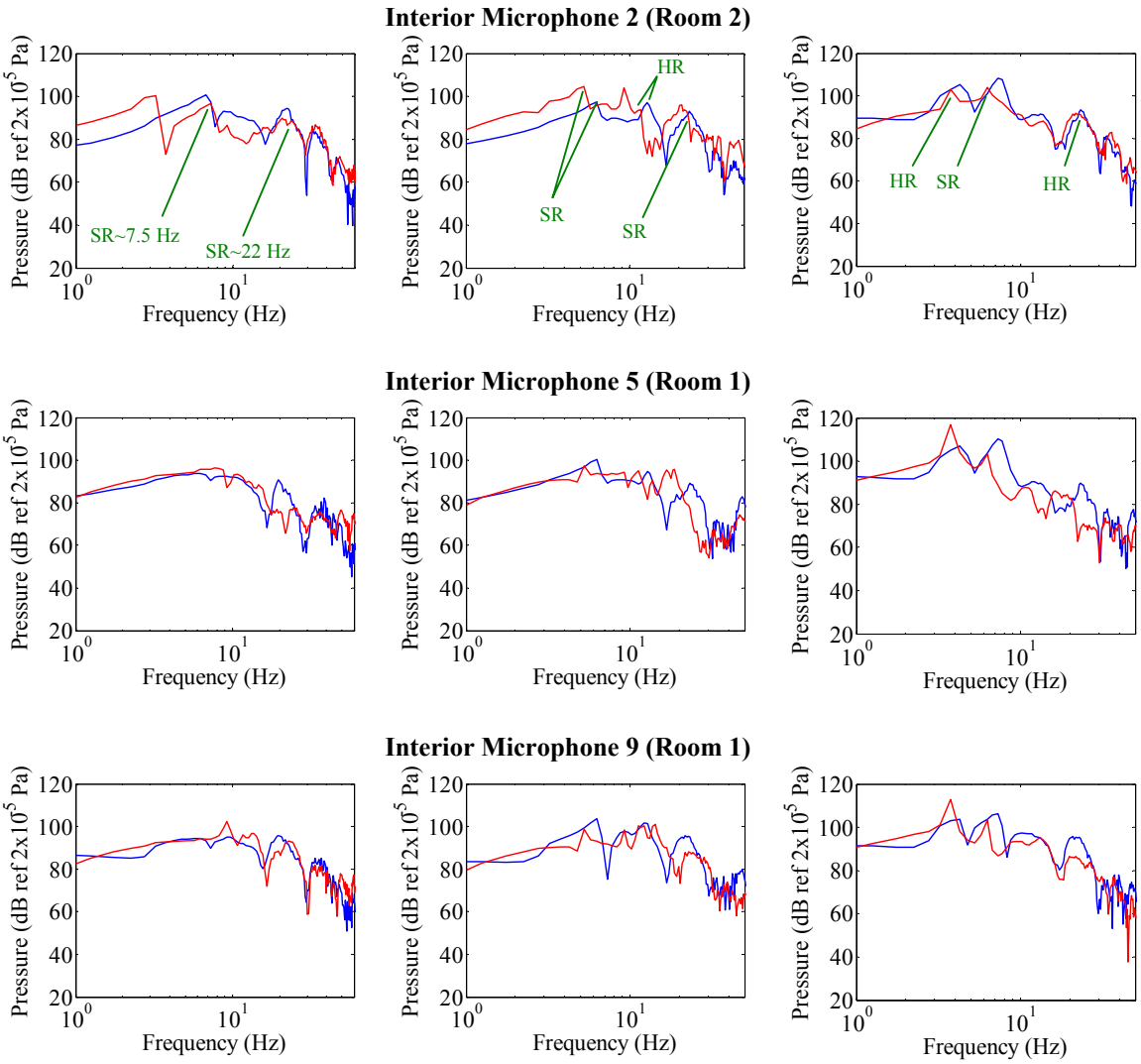

Figure 3.47: Magnitudes of the FT of the pressures inside the structure, measured (blue) and predicted (red), for the structure in configurations 1 (left column), 2 (center column), and 3 (right column).

4. Parametric Study

A preliminary parametric study is conducted to assess the effects of the incident-wave parameters and effects of the structure geometry on the response of a single wall backed by a rigid rectangular enclosure. The model does not compute the pressure loading over a given structure based on the shape and orientation of the incident sonic boom. This pressure loading is estimated experimentally. For the case of a two-dimensional structure like the single wall, the pressure loading can be estimated assuming that the pressure at a given instant of time is due to a uniform plane wave at normal incidence acting over the wall assumed baffled. For the other two structures that have three-dimensional geometries, the effects of diffraction cannot be ignored. Therefore, parametric studies were not carried out for these structures.

4.1 Effect of N-wave Duration

The pressure distribution considered in this subsection is an N-wave with maximum and minimum overpressures of ±100 Pa, rise and fall times $t_r = t_f = 2$ ms, and a duration that is varied from $t_d = 10$ to 300 ms in 2-ms increments. The room and wall have the same dimensions as in the previous section, which are $L_{rx} = 2.24$ m, $L_{ry} = 2.31$ m, $L_{rz} = 2.59$ m, $L_{sx} = 1.82$ m, and $L_{sy} = 2.21$ m. Calculations were also carried out for the same geometry but with an increased room depth, $L_{ry} = 6.17$ m, such that the natural frequency of the third acoustic mode, (0,1,0) mode, matches that of the first structural mode, (1,1) mode.

To make meaningful comparisons between the responses, it is necessary to define some dimensionless parameters. The peak amplitude of the acceleration times m_s at a given point on the wall surface, $\ddot{w}^{\max}$, compared to the shock wave overpressure, $p_{sw}^{\max}$, defines the peak amplitude ratio $R_a = m_s \ddot{w}^{\max} / p_{sw}^{\max}$. Similarly, the largest pressure at a given point inside the room, $p^{\max}$, compared to the shock wave overpressure defines the peak amplitude ratio $R_p = p^{\max} / p_{sw}^{\max}$. It was shown in the previous section that the system response is dominated by the first structural mode. Therefore, the boom duration is normalized by the fundamental mode period, i.e. $T_d^s = t_d f_1^s$ where f_1^s is the natural frequency of the first structural mode.

Figure 4.1 shows the amplitude ratio of the acceleration at the center of the wall as a function of the normalized boom duration. For the room with a depth of 2.31 m (solid curve), the amplitude ratio is maximum for T_d^s = 0.85 and then reaches local maxima at integer multiples of T_d^s. This result is in good agreement with the fact that the structural response is indeed dominated by the fundamental mode. For the room with a depth L_{ry} = 6.17 m (dashed line), R_a does not exactly follow this trend. It exhibits a slightly lower amplitude as a result of the vibro-acoustic coupling that occurs between the first structural and third acoustic modes. This fact can be verified by omitting the term corresponding to the room acoustic pressure in the dynamic equation of the wall, i.e. artificially removing vibro-acoustic coupling when computing the system response. In the absence of coupling, the variation of R_a with T_d^s is the same for L_{ry} = 2.31 m ("×" markers) and L_{ry} = 6.17 m ("+" markers).

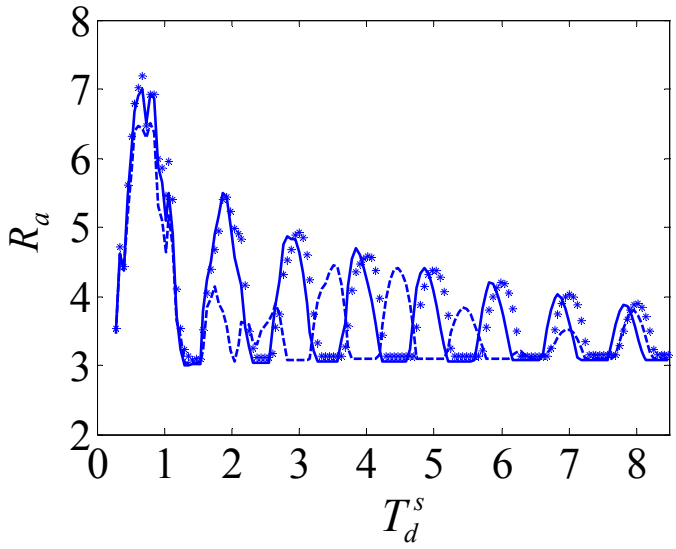

Figure 4.1: Amplitude ratio of the acceleration R_a at the center of the wall as a function of the structural period ratio T_d^s (t_r = 2 ms). Fully-coupled fluid-structure interaction, L_{ry} = 2.31 m (_____) and L_{ry} = 6.17 m (- - - - - -). Uncoupled fluid-structure interaction, L_{ry} = 2.31 m (×) and L_{ry} = 6.17 m (+).

Figure 4.2 shows the amplitude ratio of the pressure close to the center of the wall surface as a function of the normalized boom duration. For the room with a depth of 2.31 m (solid line), the amplitude ratio only exhibits one local maximum value, when T_d^s = 0.85. A similar result was obtained by Wahba et al. [54] in the study of the transmission of sonic booms inside a room with an open window. The fact that no peak was observed for integer values of T_d^s higher than 1 was demonstrated to be caused by damping. As the undamped problem was solved, these peaks could then be observed. For the room with a depth of 6.17 m (dashed line), the asymptotic value R_p tends to, is larger than that for a room depth of 2.31 m and local maxima are observed for values of T_d^s larger than unity. These maxima may now be observed because damping decreases as the volume of the room increases. In the absence of vibro-acoustic coupling, only the response of the room with a depth of 6.17 m is changed. The amplitude ratio exhibits then a much larger value

than for the fully-coupled system and local maxima when T_d^s is an integer. This result also suggests the need to consider the fluid-structure interaction fully-coupled for the solution to be truly representative.

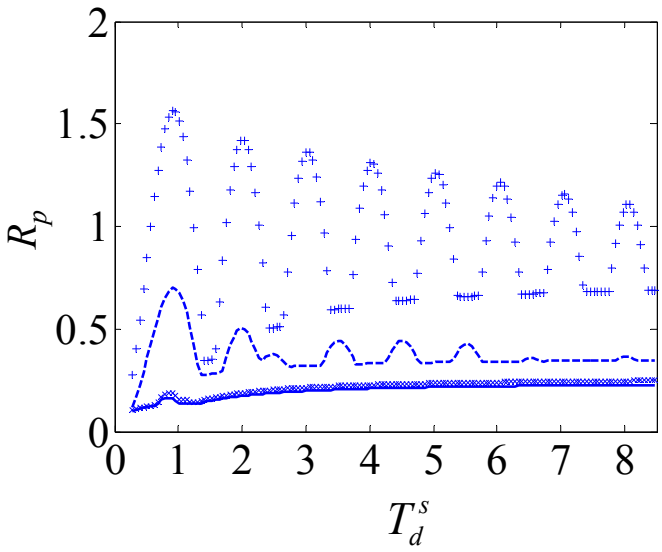

Figure 4.2: Amplitude ratio of the pressure R_p close to the center of the wall surface as a function of the period ratio T_d^s (t_r = 2 ms). Fully-coupled fluid-structure interaction, L_{ry} = 2.31 m (_____) and L_{ry} = 6.17 m (- - - - - -). Uncoupled fluid-structure interaction, L_{ry} = 2.31 m (×) and L_{ry} = 6.17 m (+).

4.2 Effect of N-wave Rise Time

To study the effect of the N-wave rise time, the system response was computed for N-waves with maximum and minimum overpressures of ±100 Pa, period ratios T_d^s = 1 (t_d = 36 ms), 3 (t_d = 108 ms), 5 (t_d = 180 ms), and 7 (t_d = 252 ms), and rise and fall times that are varied from $t_r = t_f = 0$ to $t_d/4$. To assess the effect on the system response of smoothing out the peak of the N-wave overpressure, simulations were also carried out for the excitation being one period of a sine wave of period t_d with maximum and minimum

overpressures of ±100 Pa. The room and wall have dimensions L_{rx} = 2.24 m, L_{ry} = 2.31 m, L_{rz} = 2.59 m, L_{sx} = 1.82 m, and L_{sy} = 2.21 m.

It is interesting to examine the frequency content of an incident wave regardless of the wave duration or amplitude. For this purpose, the weighted energy E at a frequency f is defined as the amount of power contained in the frequency band $0 - f$ relative to the total power of the incident wave. The weighted energy was computed as a function of the normalized frequency $F_d = f^* t_d$ and is plotted in Figure 4.3 for a perfect N-wave (solid line) and N-wave with rise time $t_r = t_d/4$ (dashed line). There is a critical frequency, F_d^c = 1.2, below which the spectral density of the perfect N-wave is larger than that of an N-wave with rise time $t_d/4$ and above which it is smaller. This means that N-waves with longer rise times contain more energy in their low frequency components than those with smaller rise times. This result suggests that the amplitude of the structural response due to an N-wave with rise time $t_d/4$ will be larger than that due to a perfect N-wave around resonance (T_d^s = 1), and smaller above resonance.

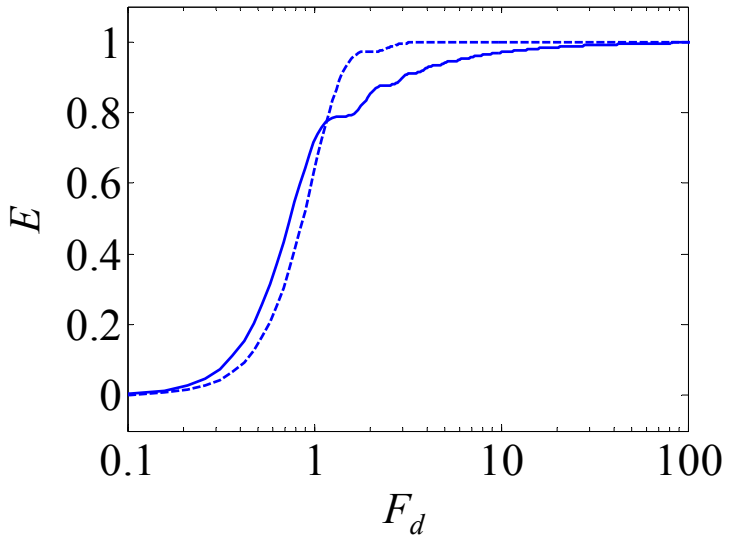

Figure 4.3: Weighted energy E as a function of normalized frequency F_d. N-waves with rise times $t_r = 0$ (_____) and $t_d/4$ (- - - - - -).

Figure 4.4 and Figure 4.5 show the amplitude ratios of the acceleration at the center of the wall and pressure close to the center of the wall surface as a function of the normalized rise time defined as $T_r = t_r/t_d$. In the figures, the hollow circles, squares, triangles, and diamonds correspond to N-waves with T_d^s = 1, 3, 5, and 7, respectively. The solid circles, squares, triangles, and diamonds correspond to one period of a sine wave with T_d^s = 1, 3, 5, and 7, respectively. The amplitudes of the acceleration and pressure increase with the rise time when the boom duration is the same as the natural period of the first structural mode, i.e. T_d^s = 1 (hollow circles) which is analogous to driving the structure at resonance. On the other hand, it decreases when T_d^s is much larger than unity, for instance T_d^s = 5 (hollow triangles) and T_d^s = 7 (hollow diamonds). In the transition between these two cases, e.g. T_d^s = 3 (hollow squares), the amplitudes of the acceleration and pressure decrease with T_r for part of the T_r range only. For all cases except T_d^s = 3, the system response due to a one-period sine wave is much smaller than

that due to an N-wave with rise time $t_d/4$. The fact that for $T_d^s = 3$ the amplitudes do not follow this trend is because at $f = f_1^s$, the spectrum of the N-wave with rise time $t_d/4$ exhibits a minimum of magnitude whereas that of the sine wave does not.

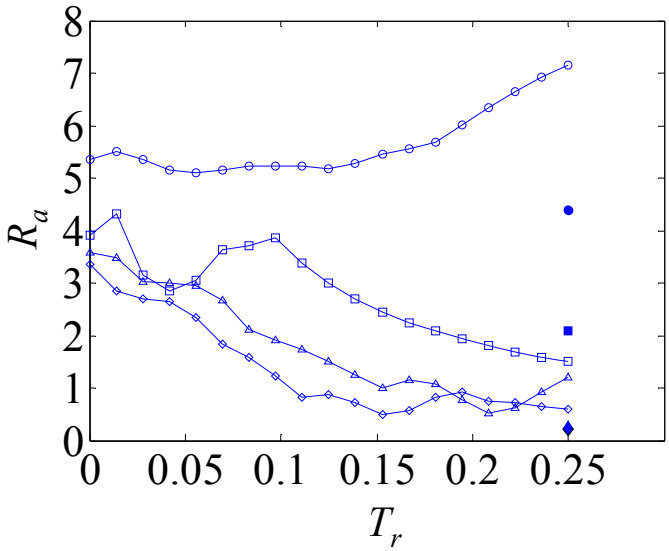

Figure 4.4: Amplitude ratio of the acceleration R_a at the center of the wall as a function of the normalized rise time T_r. Excitation: N-wave with $T_d^s = 1$ (○), 3 (□), 5 (Δ), and 7 (◊); one period of a sine wave with $T_d^s = 1$ (●), 3 (■), 5 (▲), and 7 (♦).

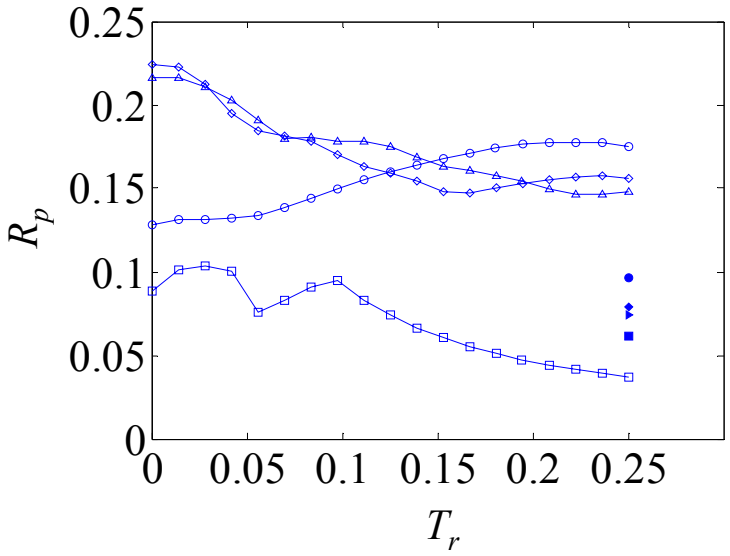

Figure 4.5: Amplitude ratio of the pressure R_p close to the center of the wall surface as a function of the normalized rise time T_r. Excitation: N-wave with T_d^s = 1 (○), 3 (□), 5 (Δ), and 7 (◊); one period of a sine wave with T_d^s = 1 (●), 3 (■), 5 (▲), and 7 (♦).

4.3 Effects of Wall and Room Dimensions

Studying the system response at fixed boom characteristics and varying room dimensions is the inverse problem of that solved in Section 4.l. The incident waves are N-waves with durations of 36 ms and 210 ms, and a rise time of 2 ms. The fundamental frequency of the wall is varied from f_1^s = 10 to 80 Hz in 2 Hz increments. With an aspect ratio of 1.25 such that, L_{sy} = 1.25*L_{sx}, this is equivalent to varying L_{sx} from 3 to 1.1 m. For each wall dimension, the natural frequency of the third acoustic mode, (0,1,0) modes, is varied from f_3^a = 20 to 80 Hz in 2 Hz increments, which is equivalent to decreasing L_{ry} from 8.6 to 2.1 m. The other two room lengths were set equal to those of the wall. The frequencies of the third acoustic modes are normalized and the acoustic period ratio is defined as $T_d^a = t_d f_3^a$.

Variation of the amplitude ratio of the acceleration at the center of the wall with the structural and acoustic period ratios is shown in Figure 4.6a and b for N-waves with durations of 36 and 210 ms, respectively. At a given acoustic period ratio, the amplitude of the acceleration is the largest when T_d^s = 0.85 and then reaches local maxima approximately when T_d^s has an integer value, which is in good agreement with the results obtained in Section 4.1. At a fixed integer value of T_d^s, the amplitude of the acceleration oscillates with T_d^a as a result of the fluid-structure coupling.

Variation of the amplitude ratio of the pressure close to the center of the wall surface with the structural and acoustic period ratios is shown in Figure 4.7. The amplitude of the pressure increases with T_d^a (or with the room depth). The figure also suggests that maxima of amplitudes are reaches when T_d^s and T_d^a are equal the same integer value, the largest value being reached when $T_d^s = T_d^a = 1$.

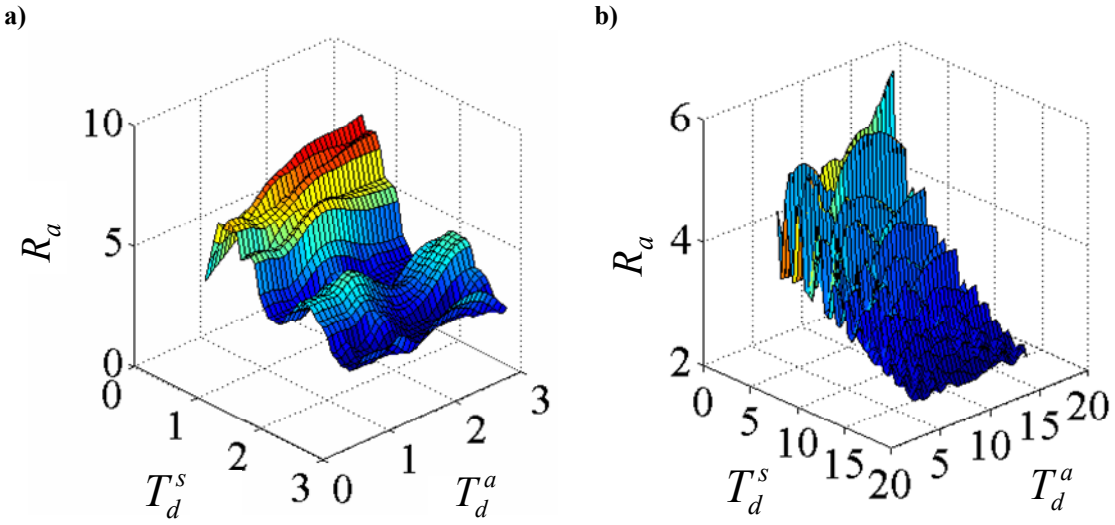

Figure 4.6: Amplitude ratio of the acceleration R_a at the center of the wall as a function of the structural and acoustic period ratios T_d^s and T_d^a. a) t_d = 36 ms and b) t_d = 210 ms.

a) **b)**

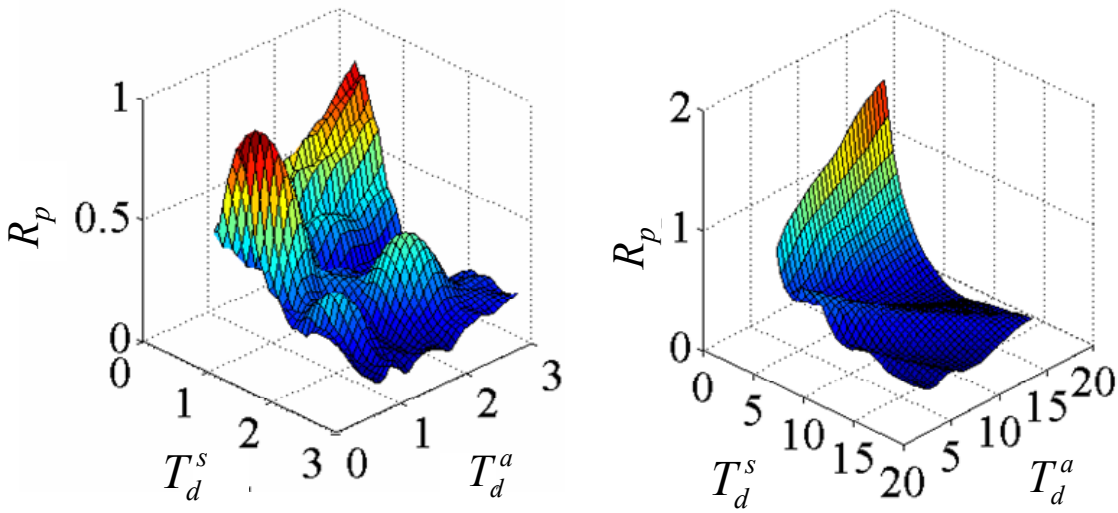

Figure 4.7: Amplitude ratio of the pressure R_p close to the center of the wall surface as a function of the structural and acoustic period ratios T_d^s and T_d^a. a) t_d = 36 ms and b) t_d = 210 ms.

5. Conclusions and Recommended Future Work

A numerical model and a computer code were developed to predict the vibro-acoustic responses of simplified residential buildings exposed to sonic booms, at low frequency, in the 0-200 Hz frequency range. The response of the fluid-structure system, including their fully coupled interaction, was computed in the time domain using a modal-decomposition approach for both the structural and acoustic systems. This approach is easy to implement and computationally efficient at low frequency, when the modal density is relatively low. The model was designed specifically for this application and it includes several novel formulations and capabilities:

i) The numerical model accounts for the fully coupled interaction of the fluid-structure system.

ii) A new shell finite-element was derived to model the structural components, typically used in building construction, that have orthotropic characteristics such as plaster-wood walls, metal roofing, and siding panels.

iii) A new formulation based on the Helmholtz resonator approach was derived to model room openings, interconnecting rooms and to the outside, at low frequency. The formulation was implemented in the fluid-structure model. The formulation is novel in the sense that it models room openings within the coupled interaction of a fluid-structure system.

iv) A dedicated finite element module was developed that implements the new shell element for orthotropic components, a conventional shell element for isotropic components (windows and doors), and the finite element for room openings.

v) The numerical model is applicable to structures with multiple rectangular cavities, isolated or interconnected with openings.

The model and computer code were successfully validated through experiments carried out on three different structures of increasing complexity: i) a single wall backed by a rigid rectangular enclosure, ii) a single-room structure with two-double panel windows and a door, and iii) a structure consisting of two rooms interconnected with a door, and two attic cavities above the rooms. Comparison of the predicted responses with the experimental data showed a number of important validation results:

i) The model predicts fairly accurately (within 5-10 dB difference) the vibration and interior acoustic responses of the three structure tested above 20 Hz. Below 20 Hz, responses are often largely under-predicted as a result of the difficulty in modeling the junction between the subcomponents of a structure. However, for all practical purposes, acoustic responses in the range of 0 to 20 Hz are of little interest as they fall below the range of audible frequencies.

ii) The 2-D shell element developed in this research models very accurately the dynamics of a wall assembly (e.g. studs+OSB+drywall). Therefore, there is no need to model all the individual subcomponents of the assembly and their inter-connections, which would result in solving a complex 3-D problem.

iii) Room openings can accurately be modeled as pistons at low-frequency as most Helmholtz resonances of interconnected rooms can be captured by the model. This result is very important because it means that little modification of the structural-

acoustic model is required to model the dynamic of room openings and the acoustics of interconnected rooms.

Finally, a parametric study was undertaken on the single-wall case. This study showed that the amplitudes of the structural and acoustic responses are the largest when the ratio of wave duration and period of the first structural mode is close to unity. It was also found that for integer values of this ratio, the system response exhibits local maxima when vibro-acoustic coupling is weak but does not necessarily follow this trend otherwise.

The numerical formulation presented in this study can be extended in a number of ways to develop a truly practical tool for predicting the human response to sonic booms inside realistic building structures. Recommendations for future research are as follows:

i) A frequency-domain solver should be developed to handle the frequency-dependent properties of room openings.

ii) In this study, the formulation is applicable to rooms with rectangular geometries only, which allows for the acoustic eigenproperties of the rooms to be determined using simple analytical expressions. The model needs to be extended to handle other room geometries. The use of numerical techniques such as the finite element method may then be required.

iii) In this study, the formulation for computing the pressure loading over the external surfaces of a given structure due to an incident wave with arbitrary shape and orientation was not developed. Instead, the pressure loading was estimated

experimentally. A formulation and a module for the code need to be developed to compute the pressure loading on the structure including the effects of diffractions.

iv) The formulation needs to be extended to predict the vibro-acoustic response of building structures at higher frequencies, i.e. beyond 200 Hz. One possible approach is to use ray-tracing techniques. To implement this approach, the motion of the interior surfaces of the rooms could be modeled as an array of "virtual noise sources." Advantage should be taken of the fact that, in the high frequency region, the structural-acoustic coupling can be neglected. Therefore, the structural response can be computed independently of the interior acoustic response.

v) In this study, the interior acoustic response predicted by the model was that a microphone would measure. However, to investigate human reaction to sonic booms, the binaural response that includes the wave diffraction and reflection properties of the head, pinna, and torso needs to be developed. The process of rendering audible the sound field of a source in a space in such a way as to simulate the binaural listening experience is called auralization.

References

[1] E. Hagerman, "All Sonic, No Boom: New York to LA in Two Hours, Quietly," *Popular Science Magazine*, March 2007.

Sonic Boom Generation, Propagation, and Evolution

[2] K. J. Plotkin, "State of the Art of Sonic Boom Modeling," *Journal of the Acoustical Society of America*, **111**(1), 2002.

[3] W. D. Hayes, "Linearized Supersonic Flow," Ph.D. Thesis, California Institute of Technology; reprinted as North American Aviation AL-222; available as Princeton University AMS Report 852, 1947.

[4] R. T. Whitcomb and T. L. Fischetti, "Development of a Supersonic Area Rule and an Application to the Design of a Wing-Body Combination Having High Lift-to-Drag Ratios," NASA-RM-L53H31a, 1953.

[5] R. T. Jones, "Theory of Wing-Body Drag at Supersonic Speeds," NACA-RM-A53H18a, 1953.

[6] H. Lomax, "The Wave Drag of Arbitrary Configurations in Linearized Flow as Determined by Areas and Forces in Oblique Planes," NACA-RM-A55A18, 1955.

[7] F. Walkden, "The Shock Pattern of a Wing-Body Combination, Far from the Flight Path," *Aeronautical Quarterly*, **9**(2), 1958

[8] D. I. Blokhintzev, "The Propagation of Sound in an Inhomogeneous and Moving Medium I," *Journal of the Acoustical Society of America*, **18**(2), 1946.

[9] J. B. Keller, "Geometrical Acoustics. I. The Theory of Weak Shock Waves," *Journal of Applied Physics*, **25**(8), 1954.

[10] G. B. Whitham, "The Flow Pattern of a Supersonic Projectile," *Communications on Pure and Applied Mathematics,* **5**, 1952.

[11] G. B. Whitham, "On the Propagation of Weak Shock Waves," *Journal of Fluid Mechanics*, **1**(3), 1956.

[12] A. Tokuyama, K. Sakai, and H. Taka, "Experimental Study of Sonic Boom Acceptance," *AIAA, Aircraft Design, Systems and Operations Meeting*, Monterey, CA, August 11-13, 1993. AIAA-1993-3961.

Designs for Sonic Boom Mitigation

[13] A. Bucovsky, J. Eyer, and D. Mavris, "Design Space Exploration for Boom Mitigation on a Quiet Supersonic Business Jet," *AIAA's 3rd Annual Aviation Technology,*

Integration, and Operations (ATIO) Forum, Denver, CO, November 17-19, 2003. AIAA 2003-6802.

[14] R. Seebass and A. R. George, "Sonic-Boom Minimization," *Journal of the Acoustical Society of America*, **51**(2), 1972.

[15] C. Darden, "Sonic Boom Minimization with Nose Bluntness Relaxation," NASA TP-1348, 1979.

[16] H. W. Carlson, R. L. Barger, and R. J. Mack, "Application of Sonic-Boom Minimization Concepts in Supersonic Transport Design," NASA TN D-7218, June 1973.

[17] J. Morgenstern, A. Arslan, V. Lyman, and J. Vadyak, "F-5 Shaped Sonic Boom Demonstrator's Persistence of Boom Shaping Reduction Through Turbulence" *43rd AIAA Aerospace Sciences Meeting and Exhibit*, Reno, NV, January 10-13, 2005. AIAA-2005-12.

[18] D. H. Graham, J. A. Dahlin, K. B. Meredith, and J. L. Vadnais, "Aerodynamic Design of Shaped Sonic Boom Demonstration Aircraft,**"** *43rd AIAA Aerospace Sciences Meeting and Exhibit*, Reno, NV, January 10-13, 2005. AIAA-2005-8.

[19] D. C. Howe, "Improved Sonic Boom Minimization with Extendable Nose Spike," *43rd AIAA Aerospace Sciences Meeting and Exhibit*, Reno, NV, January 10-13, 2005. AIAA-2005-1014.

[20] J. R. Wilson, "Quiet Spike Softening the Sonic Boom," *Aerospace America*, October 2007.

[21] Photograph taken by Carla Thomas from the NASA Dryden Flight Research Center: http://www.dfrc.nasa.gov/Gallery/Photo/Quiet_Spike/HTML/ED06-0184-10.html

Experimental Sonic-Boom Simulation

[22] J. Klos and R. Buehrle, "Vibro-Acoustic Response of Buildings Due to Sonic Boom Exposure: June 2006 Field Test," NASA/TM-2007-214900, 2007.

[23] J. Klos, "Vibro-Acoustic Response of Buildings Due to Sonic Boom Exposure: July 2007 Field Test," NASA/TM-2008-215349, 2008.

[24] I. I. Glass, H. S. Ribner and J. J. Gottlieb, "Canadian Sonic-Boom Simulation Facilities," *Canadian Aeronautics and Space Journal,* **18**(10), 1972.

[25] N. D. Ellis, I. B. Rushwald, and H. S. Ribner, "A One-Man Portable Sonic Boom Simulator," *Journal of Sound and Vibration*, **40**(1), 1975.

[26] N. N. Wahba, I. I. Glass, and R. C. Tennyson, "Pressures Inside a Room Subjected to Simulated Sonic Booms," *Journal of Sound and Vibration*, **68**(2), 1980.

[27] S. J. Hawkins and J. A. Hicks, "Sonic Bang Simulation by a New Explosive Technique," *Nature*, **211**(5055), 1966.

[28] M. J. Harper, S. J. Hawkins, and J. A. Hicks, "Explosively Generated Air Pressure Waves for Structural Forcing," *Journal of Sound and Vibration*, **11**(2), 1970.

[29] R. T. Strugielski, L. E. Fugelso, L. B. Holmes, and W. J. Byrne, "Development of a Sonic Boom Simulator with Detonable Gases," NASA-CR-1844, 1971.

[30] J. D. Leatherwood, K. P. Shepherd, and B. M. Sullivan, "A New Simulator for Assessing Subjective Effects of Sonic Booms," NASA-TM-104150, 1991.

[31] J. D. Leatherwood and B. M. Sullivan, "Laboratory Study of Effects of Sonic Boom Shaping on Subjective Loudness and Acceptability," NASA-TP-3269, 1992.

[32] J. Salamone, "Sonic Boom Simulation Using Conventional Audio Equipment" *Noise-Con 2004*, Baltimore, MD, July 12-14, 2004.

[33] Y. Naka, Y. Makino, and T. Ito, "Laboratory Experiment on Indoor Sonic Booms and Sonic-Boom-Induced Vibration of Buildings," *14th AIAACEAS Aeroacoustics Conference,* Vancouver, BC, Canada, May 5-7, 2008. AIAA-2008-3037

Structural Response Due to Sonic Booms

[34] L. Meirovitch, Analytical Methods in Vibrations, Macmillan, New York, 1967.

[35] D. H. Cheng and S. E. Benveniste, "Transient Response of Structural Elements to Traveling Pressure Waves of Arbitrary Shape," *International Journal of Mechanical Sciences*, **8**, 1966.

[36] M. J. Crocker, "Multimode Response of Panels to Normal and to Traveling Sonic Booms," *Journal of the Acoustical Society of America*, **42**(5), 1967.

[37] J. R. Coleby and J. Mazumdar, "Transient Vibrations of Elastic Panels Due to the Impact of Shock Waves," *Journal of Sound and Vibration*, **77**(4), 1981.

[38] J. Mazumdar and J. R. Coleby, "Simplified Approach to the Vibration Analysis of Elastic Plates due to Sonic Boom," *Journal of Sound and Vibration*, **45**(4), 1976.

[39] A. Craggs, "The Response of a Simply Supported Plate to "N" Waves at Oblique Incidence," *Journal of Sound and Vibration*, **16**(2), 1971.

[40] N. Popplewell, “The Vibration of a Box-Type Structure. I. Natural Frequencies and Normal Modes,” *Journal of Sound and Vibration*, **14**(3), 1971.

[41] N. Popplewell, “The Vibration of a Box-Type Structure. II. Response to a Travelling Pressure Wave,” *Journal of Sound and Vibration*, **18**(4), 1971.

[42] N.N. Wahba, “Analysis of a Plaster-Wood Wall Using a Series Solution,” *Computers & Structures*, **35**(2), 1990.

[43] N.N. Wahba, “Dynamic Response of a Plaster-Wood Wall to Sonic Booms Using a Series Solution,” *Computers & Structures*, **35**(2), 1990.

[44] N.N. Wahba, “Analysis of a Plaster-Wood Wall using Finite-Element Method,” *Computers & Structures*, **36**(4), 1990.

Fluid-Structure Coupling

[45] A. J. Pretlove, “Free Vibrations of a Rectangular Panel Backed by a Closed Cavity,” *Journal of Sound and Vibration*, **2**(3), 1965.

[46] A. J. Pretlove, “Forced Vibrations of a Rectangular Panel Backed by a Closed Cavity,” *Journal of Sound and Vibration*, **3**(3), 1966.

[47] A. J. Pretlove and A. Craggs, "A Simple Approach to Coupled Panel Cavity Vibrations," *Journal of Sound and Vibration*, **11**(2), 1970.

[48] A. Craggs, "Computation of the Response of Coupled Plate-Acoustic Systems Using Plate Finite Elements and Acoustic Volume-Displacement Theory," *Journal of Sound and Vibration*, **18**(2), 1971.

[49] A. Craggs, "The Transient Response of a Coupled Plate-Acoustic System Using Plate and Acoustic Finite Elements," *Journal of Sound and Vibration*, **15**(4), 1971.

[50] F. Fahy; Sound and Structural Vibration: Radiation, Transmission and Response, Academic Press, New York, 1985.

Transmission of a Sonic Boom through an Opening

[51] P. G. Vaidya, "The Acoustic Response of Rooms with Open Windows to Airborne Sounds," *Journal of Sound and Vibration*, **25**(4), 1972.

[52] P. G. Vaidya, "The Transmission of Sonic Boom Signals into Rooms through Open Windows," *Journal of Sound and Vibration*, **25**(4), 1972.

[53] S. Lin, "Sonic-Boom Analog for Investigating Indoor Acoustical Waves," *Journal of the Acoustical Society of America*, **49**(5A), 1971.

[54] N. N. Wahba, I. I. Glass, and R. C. Tennyson, "Pressures Inside a Room Subjected to Simulated Sonic Booms," *Journal of Sound and Vibration*, **68**(2), 1980.

[55] H. H. Hubbard and K. P. Shepherd, "The Helmholtz Resonance Behavior of Single and Multiple Rooms," NASA/CR-178173, 1986.

Miscellaneous

[56] N. M. Newmark, "A Method of Computation for Structural Dynamics," *ASCE Journal of the Engineering Mechanics Division*, **85**(3), 1959.

[57] J. M. Corcoran "Output-Only Experimental Modal Testing of Large Residential Structures and Acoustic Cavities Using Sonic Booms," Master's Thesis, Virginia Polytechnic Institute and State University, 2009.

[58] S. Timoshenko and S. Woinowsky-Krieger, Theory of Plates and Shells, 2nd ed, McGraw-Hill, New York, 1959.

[59] A. D. Pierce, Acoustics: an Introduction to its Physical Principles and Applications, McGraw-Hill, New York, 1991.

[60] C. L. Morfey, "Acoustic Properties of Openings at Low Frequencies," *Journal of Sound and Vibration*, **9**(3), 1969.

[61] L. E. Kinsler, A. R. Frey, A. B. Coppens, and J. V. Sanders, Fundamentals of Acoustics, 4th ed, John Wiley & Sons, Inc., New York, 4th edition, 2000.

[62] A. Edward and R. Thallon, Fundamentals of Residential Construction, Wiley, New York, 2006.

[63] G. H. James, T. G. Garne, and J. P. Lauffer, "The Natural Excitation Technique (NExT) for Modal Parameter Extraction from Operating Wind Turbines," Report SAND92-1966, UC-261, Sandia National Laboratories, Albuquerque, NM, 1993.

[64] O. C. Zienkiewicz and R. L. Taylor, The Finite Element Method, 4th ed., McGraw-Hill, New York, 1991.

[65] G. Prathap, The Finite Element Method in Structural Mechanics: Principles and Practice of Design of Field-Consistent Elements for Structural and Solid Mechanics, Kluwer Academic Publishers, Dordrecht, 1993.

[66] Y. W. Kwon and H. Bang, The Finite Element Method Using MATLAB, 2nd ed., CRC Press, Boca Raton, 2000.

Appendix A. Newmark-β Numerical Integration Scheme

The most general approach to the solution of the dynamic response of structural systems is the direct numerical integration of the dynamic equilibrium equations. This involves, after the solution is defined at time zero, the attempt to satisfy dynamic equilibrium at discrete points in time. Newmark [56] presented a family of single-step integration methods for the solution of structural dynamic problems for both blast and seismic loading. Newmark's numerical scheme is used here for the computation of the system dynamics.

The dynamic equations governing the vibro-acoustic response of a structure exposed to an arbitrary pressure loading are expressed in condensed form as,

$$\mathbf{M}\ddot{\mathbf{u}}_t + \mathbf{C}\dot{\mathbf{u}}_t + \mathbf{K}\mathbf{u}_t = \mathbf{F}_t \tag{A.1}$$

where bold indicate matrices and vectors. The direct use of Taylor's series provides a rigorous approach to obtain the following two additional equations,

$$\mathbf{u}_t = \mathbf{u}_{t-\Delta t} + \Delta t\dot{\mathbf{u}}_{t-\Delta t} + \frac{1}{2}\Delta t^2\ddot{\mathbf{u}}_{t-\Delta t} + \frac{1}{6}\Delta t^3\dddot{\mathbf{u}}_{t-\Delta t} + \mathrm{O}\left(\Delta t^4\right) \tag{A.2}$$

and

$$\dot{\mathbf{u}}_t = \dot{\mathbf{u}}_{t-\Delta t} + \Delta t\ddot{\mathbf{u}}_{t-\Delta t} + \frac{1}{2}\Delta t^2\dddot{\mathbf{u}}_{t-\Delta t} + \mathrm{O}\left(\Delta t^3\right) \tag{A.3}$$

These equations are truncated and expressed in the following form,

$$\mathbf{u}_t = \mathbf{u}_{t-\Delta t} + \Delta t\dot{\mathbf{u}}_{t-\Delta t} + \frac{1}{2}\Delta t^2\ddot{\mathbf{u}}_{t-\Delta t} + \beta\Delta t^3\dddot{\mathbf{u}}_{t-\Delta t} \tag{A.4}$$

and

$$\dot{\mathbf{u}}_t = \dot{\mathbf{u}}_{t-\Delta t} + \Delta t \ddot{\mathbf{u}}_{t-\Delta t} + \gamma \Delta t^2 \dddot{\mathbf{u}}_{t-\Delta t} \tag{A.5}$$

If the acceleration is assumed to be linear within the time step, the following equation can be written,

$$\dddot{\mathbf{u}}_t = \frac{\left(\ddot{\mathbf{u}}_t - \ddot{\mathbf{u}}_{t-\Delta t}\right)}{\Delta t} \tag{A.6}$$

Substitution of the above equation into Equations (A.4) and (A.5) produces Newmark's equations in standard form,

$$\mathbf{u}_t = \mathbf{u}_{t-\Delta t} + \Delta t \dot{\mathbf{u}}_{t-\Delta t} + \left(\frac{1}{2} - \beta\right)\Delta t^2 \ddot{\mathbf{u}}_{t-\Delta t} + \beta \Delta t^2 \ddot{\mathbf{u}}_t \tag{A.7}$$

and

$$\dot{\mathbf{u}}_t = \dot{\mathbf{u}}_{t-\Delta t} + (1-\gamma)\Delta t \ddot{\mathbf{u}}_{t-\Delta t} + \gamma \Delta t \ddot{\mathbf{u}}_t \tag{A.8}$$

Substitution of Equations (A.7) and (A.8) into Equation (A.1) allows the dynamic equilibrium of the system at time *t* to be written in terms of the unknown $\ddot{\mathbf{u}}_t$,

$$\left(\mathbf{M} + a_1\mathbf{C} + a_2\mathbf{K}\right)\ddot{\mathbf{u}}_t = \mathbf{F}_t - \mathbf{K}\left(\mathbf{u}_{t-\Delta t} + a_3\dot{\mathbf{u}}_{t-\Delta t} + a_4\ddot{\mathbf{u}}_{t-\Delta t}\right) - \mathbf{C}\left(\dot{\mathbf{u}}_{t-\Delta t} + a_5\ddot{\mathbf{u}}_{t-\Delta t}\right) \tag{A.9}$$

where, $a_1 = \gamma\Delta t$, $a_2 = \beta\Delta t^2$, $a_3 = \Delta t$, $a_4 = \left(\frac{1}{2} - \beta\right)\Delta t^2$, and $a_5 = (1-\gamma)\Delta t$. The unknown $\ddot{\mathbf{u}}_t$ is simply,

$$\ddot{\mathbf{u}}_t = \overline{\mathbf{M}}^{-1}\overline{\mathbf{F}}_t \tag{A.10}$$

where $\overline{\mathbf{M}} = \left(\mathbf{M} + a_1\mathbf{C} + a_2\mathbf{K}\right)$ and $\overline{\mathbf{F}}_t = \mathbf{F}_t - \mathbf{K}\left(\mathbf{u}_{t-\Delta t} + a_3\dot{\mathbf{u}}_{t-\Delta t} + a_4\ddot{\mathbf{u}}_{t-\Delta t}\right) - \mathbf{C}\left(\dot{\mathbf{u}}_{t-\Delta t} + a_5\ddot{\mathbf{u}}_{t-\Delta t}\right)$.

The Newmark direct integration algorithm is summarized in Table A.1.

Table A.1: Summary of the Newmark method for direct integration.

1. INITIAL CALCULATION

A. Form static stiffness matrix **K**, mass matrix **M**, and damping matrix **C**

B. Specify integration parameters β and γ.

C. Calculate integration constants

$$a_1 = \gamma\Delta t,\ a_2 = \beta\Delta t^2,\ a_3 = \Delta t,\ a_4 = \left(\frac{1}{2} - \beta\right)\Delta t^2, \text{ and } a_5 = (1-\gamma)\Delta t$$

D. Form effective mass matrix $\overline{\mathrm{M}} = \left(\mathrm{M} + a_1\mathrm{C} + a_2\mathrm{K}\right)$.

E. Specify initial conditions u_0 and $\dot{\mathrm{u}}_0$

2. FOR EACH TIME STEP $t = \Delta t, 2\Delta t, 3\Delta t, \ldots$

A. Calculate effective load vector,

$$\overline{\mathrm{F}}_t = \mathrm{F}_t - \mathrm{K}\left(\mathrm{u}_{t-\Delta t} + a_3\dot{\mathrm{u}}_{t-\Delta t} + a_4\ddot{\mathrm{u}}_{t-\Delta t}\right) - \mathrm{C}\left(\dot{\mathrm{u}}_{t-\Delta t} + a_5\ddot{\mathrm{u}}_{t-\Delta t}\right)$$

B. Solve for $\ddot{\mathrm{u}}_t$,

$$\ddot{\mathrm{u}}_t = \overline{\mathrm{M}}^{-1}\overline{\mathrm{F}}_t$$

C. Calculate u_t and $\dot{\mathrm{u}}_t$

$$\mathrm{u}_t = \mathrm{u}_{t-\Delta t} + a_3\dot{\mathrm{u}}_{t-\Delta t} + a_4\ddot{\mathrm{u}}_{t-\Delta t} + a_2\ddot{\mathrm{u}}_t$$

$$\dot{\mathrm{u}}_t = \dot{\mathrm{u}}_{t-\Delta t} + a_5\ddot{\mathrm{u}}_{t-\Delta t} + a_1\ddot{\mathrm{u}}_t$$

D. Go to Step 2.A with $t = t + \Delta t$

Appendix B. Finite-Element Modeling

The derivation of the mass and stiffness matrices of shell elements is presented for the purpose of modeling most components forming typical building structures encountered in the United States, such as composite walls, windows, and doors. The formulation is based on work reported in references [64-66].

B.1 Shell Element as a Superposition of Plane-Stress and Bending Elements

The derivation of detailed governing equations for a curved shell problem is not trivial. In order to overcome the complexity, many alternative formulations have been proposed, each depending on the approximations being introduced. One formulation consists in considering the shell as an assembly of flat elements, an approximation of physical rather than mathematical nature. A shell has curvature along its surface. If the radius of curvature becomes infinity, the shell geometry becomes a flat plate. When a shell is divided into a number of small finite elements, each element maybe considered as a flat plate with a different orientation in space. Thus, each element may be modeled as a plate bending element. However, each element has a different orientation so that bending in one element may cause in-plane deformation in the next element. Therefore, it is necessary to include membrane capabilities to allow the element for deforming also in-plane and ensure continuity of the displacement at the structure edges. Thus, a shell may be obtained by combining a plate bending element and a plane-stress element in the same way that a 2-D frame element is obtained from a beam bending element and a bar element. As indicated in Figure B.1, a plane-stress element has two in-plane displacements per node. On the other hand, a plate bending element has a transverse

deflection and two bending rotations per node. All together, a shell has five degrees of freedom per node, three displacements and two rotations.

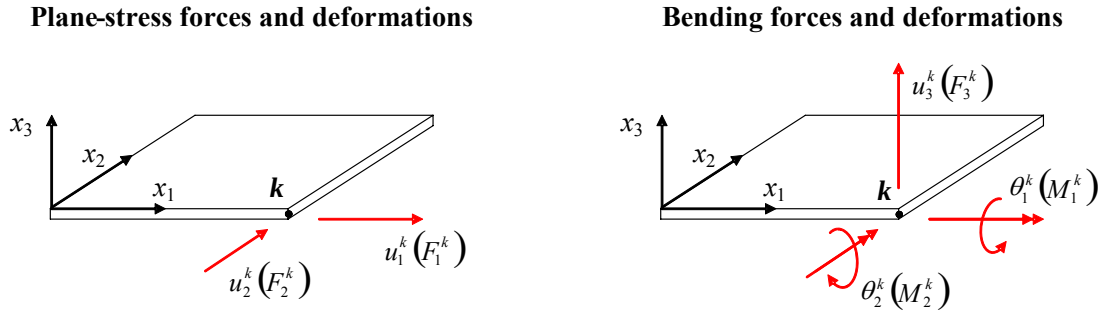

Figure B.1: Shell as a combination of plate bending element and plane stress element.

Figure B.2 shows the geometry of a four-node shell element and its coordinates systems. Three coordinate systems are used:

1. The global Cartesian coordinate system $\left(X_1, X_2, X_3\right)$
2. The running local Cartesian coordinate system at node k $\left(x_1^k, x_2^k, x_3^k\right)$
3. The natural coordinate system (ξ, η, ζ)

A point in a shell structure can be expressed by a vector sum of two vectors. The first vector is a position vector from the origin of the coordinate system to a point on the reference surface (usually the mid-surface) of the shell element. The second vector is a vector normal to the reference surface.

Two linear shape functions are used to describe a position in the element. N^k is the two dimensional shape function in the ξ-η plane defined in terms of the normalized natural domain ($-1 \le \xi \le 1$ and $-1 \le \eta \le 1$) as,

$$N^1(\xi,\eta) = \frac{1}{4}(1-\xi)(1-\eta) \tag{B.1a}$$

$$N^2(\xi,\eta) = \frac{1}{4}(1+\xi)(1-\eta) \tag{B.1b}$$

$$N^3(\xi,\eta) = \frac{1}{4}(1+\xi)(1+\eta) \tag{B.1c}$$

$$N^4(\xi,\eta) = \frac{1}{4}(1-\xi)(1+\eta) \tag{B.1d}$$

H^k is the one-dimensional shape function along the ζ axis defined as,

$$H^k(\zeta) = \frac{1}{4}\left[(1+\zeta)(1-\bar{\zeta}) - (1-\zeta)(1+\bar{\zeta})\right]\left\| \left(x_i^k\right)^{top} - \left(x_i^k\right)^{bottom} \right\| \quad (i = 1,2,3) \tag{B.2}$$

where $\bar{\zeta}$ indicates the location of the reference surface and varies from -1 to 1 ($\bar{\zeta}$ = 0 denotes the mid-surface), x_i^k is the position vector of node k in the reference surface, the superscripts *top* and *bottom* indicate the top and bottom surfaces of the shell, and $\| \ \|$ denotes the Euclidean norm.

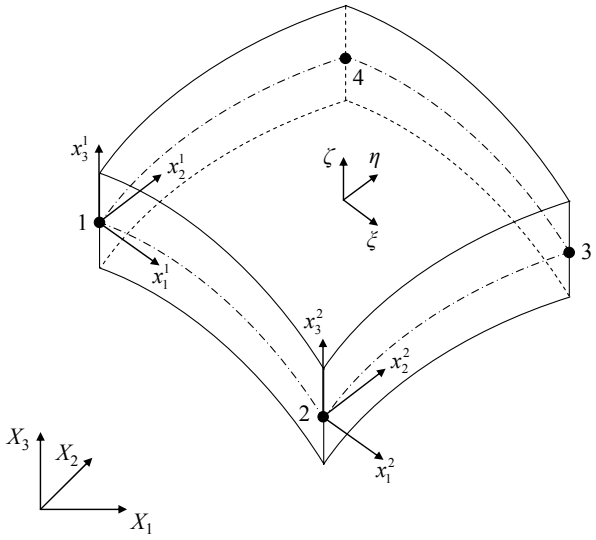

Figure B.2: Description of shell element and its coordinate systems.

It is convenient to define the unit vectors at node *k*, V_{1i}^k, V_{2i}^k, and V_{3i}^k lying along the axes x_1^k, x_1^k, and x_1^k, respectively, with V_{3i}^k defined as,

$$V_{3i}^k = \frac{\left(x_i^k\right)^{top} - \left(x_i^k\right)^{bottom}}{\left\| \left(x_i^k\right)^{top} - \left(x_i^k\right)^{bottom} \right\|} \tag{B.3}$$

A point of the shell may be described in terms of the position vectors of the nodes and the shape functions as,

$$x_i(\xi,\eta,\zeta) = \sum_{k=1}^{n} N^k(\xi,\eta) x_i^k + \sum_{k=1}^{n} N^k(\xi,\eta) H^k(\zeta) V_{3i}^k \quad (i=1,2,3) \tag{B.4}$$

where *n* is the number of nodes per element (four in this case).

B.2 Derivation of the Element Stiffness Matrix

The stiffness matrix [K^{em}] at a node *k* of a plane-stress (membrane) element satisfies,

$$\begin{Bmatrix} F_1^k \\ F_2^k \end{Bmatrix} = \left[K^{em}\right] \begin{Bmatrix} u_1^k \\ u_2^k \end{Bmatrix} \tag{B.5}$$

The stiffness matrix $[K^{eb}]$ at a node k of a bending element satisfies,

$$\begin{Bmatrix} F_3^k \\ M_1^k \\ M_2^k \end{Bmatrix} = \left[K^{eb}\right] \begin{Bmatrix} u_3^k \\ \theta_1^k \\ \theta_2^k \end{Bmatrix} \tag{B.6}$$

Before combining these stiffnesses, two facts should be noted. Firstly, the plane-stress and bending actions are decoupled. Secondly, the rotation θ_3^k that is commonly called "drilling" degree of freedom, does not enter as a parameter into the definition of deformations. While this degree of freedom could be neglected at the present stage, it is convenient to take it into account and associate it with a fictitious couple M_3^k, for reasons that will be apparent later when the element matrices and vectors are assembled into the system matrix and vector. Therefore, the stiffness matrix $[K^e]$ at node k of a shell element satisfies,

$$\begin{Bmatrix} F_1^k \\ F_2^k \\ F_3^k \\ M_1^k \\ M_2^k \\ M_3^k \end{Bmatrix} = \left[\begin{array}{ccc:ccc:c} & \left[K^{em}\right] & & 0 & 0 & 0 & 0 \\ & & & 0 & 0 & 0 & 0 \\ \hdashline 0 & 0 & & & & & 0 \\ 0 & 0 & & & \left[K^{eb}\right] & & 0 \\ 0 & 0 & & & & & 0 \\ \hdashline 0 & 0 & & 0 & 0 & 0 & 0 \end{array}\right] \begin{Bmatrix} u_1^k \\ u_2^k \\ u_3^k \\ \theta_1^k \\ \theta_2^k \\ \theta_3^k \end{Bmatrix} \tag{B.7}$$

The matrix and vectors above are expressed in terms of the running local Cartesian coordinate system $\left(x_1^k, x_2^k, x_3^k\right)$. Transformation of coordinates to the global Cartesian

coordinate system (X_1, X_2, X_3) is necessary to assemble the elements and to write the appropriate equilibrium equations. At each node the relation between the local and global degrees of freedom is expressed as,

$$\begin{Bmatrix} u_1^{local} \\ u_2^{local} \\ u_3^{local} \\ \theta_1^{local} \\ \theta_2^{local} \\ \theta_3^{local} \end{Bmatrix} = \begin{bmatrix} l_{11} & l_{12} & l_{13} & 0 & 0 & 0 \\ l_{21} & l_{22} & l_{23} & 0 & 0 & 0 \\ l_{31} & l_{32} & l_{33} & 0 & 0 & 0 \\ 0 & 0 & 0 & l_{11} & l_{12} & l_{13} \\ 0 & 0 & 0 & l_{21} & l_{22} & l_{23} \\ 0 & 0 & 0 & l_{31} & l_{32} & l_{33} \end{bmatrix} \begin{Bmatrix} u_1^{global} \\ u_2^{global} \\ u_3^{global} \\ \theta_1^{global} \\ \theta_2^{global} \\ \theta_3^{global} \end{Bmatrix} \tag{B.8}$$

where l_{ij} is the direction cosine between the local axis x_i and global axis X_j. This relation can be used for each node. Therefore, the transformation matrix for a four-node element becomes,

$$[T] = \begin{bmatrix} [T_d] & [0] & [0] & [0] \\ [0] & [T_d] & [0] & [0] \\ [0] & [0] & [T_d] & [0] \\ [0] & [0] & [0] & [T_d] \end{bmatrix} \tag{B.9}$$

where the matrix $[T_d]$ is that used in Equation (B.8) of size 6×6.

Using this transformation matrix, the transformed stiffness matrix of a four-node shell element becomes,

$$[K^{global}] = [T]^T [K^{local}][T] \tag{B.10}$$

B.2.1 Element Displacement Field

The displacement field in the shell is written as,

$$u_i(\xi,\eta,\zeta)=\sum_{k=1}^{n}N^k(\xi,\eta)u_i^k+\sum_{k=1}^{n}N^k(\xi,\eta)H^k(\zeta)\left(-V_{2i}^k\theta_1^k+V_{1i}^k\theta_2^k\right)\ (i=1,2,3) \tag{B.11}$$

where u_i^k is the nodal displacement at node *k*, θ_1^k and θ_2^k are rotational degrees of freedom along the unit vectors V_{1i}^k and V_{2i}^k, respectively.

B.2.2 Strain-Displacement Relation

Six strain components are computed from Equation (B.11) by taking the derivative with respect to x_i. The result may be written in matrix form as,

$$\{\varepsilon\}=[B][d] \tag{B.12}$$

where,

$$\{\varepsilon\}=\{\varepsilon_{11}\quad\varepsilon_{22}\quad\varepsilon_{33}\quad\gamma_{12}\quad\gamma_{23}\quad\gamma_{13}\}^T \tag{B.13}$$

$$[B]=\begin{bmatrix}B^1 & B^2 & \dots & B^n\end{bmatrix} \tag{B.14}$$

And

$$\{d\}=\begin{Bmatrix}d^1 & d^2 & \dots & d^n\end{Bmatrix}^T \tag{B.15}$$

The detailed expression for $[B^k]$ is,

$$[B^k]=\begin{bmatrix}
\frac{\partial N^k}{\partial x_1} & 0 & 0 & -g_1^kV_{21}^k & g_1^kV_{11}^k \\
0 & \frac{\partial N^k}{\partial x_2} & 0 & -g_2^kV_{22}^k & g_2^kV_{12}^k \\
0 & 0 & \frac{\partial N^k}{\partial x_2} & -g_3^kV_{23}^k & g_3^kV_{13}^k \\
\frac{\partial N^k}{\partial x_2} & \frac{\partial N^k}{\partial x_1} & 0 & -g_2^kV_{21}^k-g_1^kV_{22}^k & g_2^kV_{11}^k+g_1^kV_{12}^k \\
0 & \frac{\partial N^k}{\partial x_3} & \frac{\partial N^k}{\partial x_2} & -g_3^kV_{22}^k-g_2^kV_{23}^k & g_3^kV_{12}^k+g_2^kV_{13}^k \\
\frac{\partial N^k}{\partial x_3} & 0 & \frac{\partial N^k}{\partial x_1} & -g_3^kV_{21}^k-g_1^kV_{23}^k & g_3^kV_{11}^k+g_1^kV_{13}^k
\end{bmatrix} \tag{B.16}$$

where,

$$g_i^k = \frac{\partial N^k}{\partial x_i} H^k + N^k \frac{\partial H^k}{\partial x_i} \tag{B.17}$$

B.2.3 Jacobian Matrix

The Jacobian matrix [*J*] is required to compute derivatives such as $\frac{\partial N^k}{\partial x_i}$ and $\frac{\partial H^k}{\partial x_i}$,

$$[J] = \begin{bmatrix} x_{1,\xi} & x_{2,\xi} & x_{3,\xi} \\ x_{1,\eta} & x_{2,\eta} & x_{3,\eta} \\ x_{1,\zeta} & x_{2,\zeta} & x_{3,\zeta} \end{bmatrix} \tag{B.18}$$

where,

$$\frac{\partial x_i}{\partial \xi} = \sum_{k=1}^{n} \frac{\partial N^k}{\partial \xi} x_i^k + \sum_{k=1}^{n} \frac{\partial N^k}{\partial \xi} H^k V_{3i}^k \quad (i = 1,2,3) \tag{B.19}$$

$$\frac{\partial x_i}{\partial \eta} = \sum_{k=1}^{n} \frac{\partial N^k}{\partial \eta} x_i^k + \sum_{k=1}^{n} \frac{\partial N^k}{\partial \eta} H^k V_{3i}^k \quad (i = 1,2,3) \tag{B.20}$$

$$\frac{\partial x_i}{\partial \zeta} = \sum_{k=1}^{n} N^k \frac{\partial H^k}{\partial \zeta} V_{3i}^k \quad (i = 1,2,3) \tag{B.21}$$

B.2.4 Constitutive Equations

With the strain through the thickness being neglected, the stress corresponding to the strains are given as,

$$\{\sigma'\} = [D'] \{\varepsilon'\} \tag{B.22}$$

where $\{\sigma'\}$ and $\{\varepsilon'\}$ are the stress and strain components expressed in the local axes which are set along the reference plane made of vectors V_1 and V_2.

The constitutive matrix $[D']$ is then transformed into a matrix in terms of the stresses and strains of the global axes. The transformed matrix is,

$$[D] = [T]^T [D'][T]$$

where,

$$[T] = \begin{bmatrix} l_{11}^2 & l_{12}^2 & l_{13}^2 & l_{11}l_{12} & l_{12}l_{13} & l_{13}l_{11} \\ l_{21}^2 & l_{22}^2 & l_{23}^2 & l_{21}l_{22} & l_{22}l_{23} & l_{23}l_{21} \\ l_{31}^2 & l_{32}^2 & l_{33}^2 & l_{31}l_{32} & l_{32}l_{33} & l_{33}l_{31} \\ 2l_{11}l_{21} & 2l_{12}l_{22} & 2l_{13}l_{23} & (l_{11}l_{22}+l_{21}l_{12}) & (l_{12}l_{23}+l_{22}l_{13}) & (l_{13}l_{21}+l_{23}l_{11}) \\ 2l_{21}l_{31} & 2l_{22}l_{32} & 2l_{23}l_{33} & (l_{21}l_{32}+l_{31}l_{22}) & (l_{21}l_{32}+l_{31}l_{22}) & (l_{23}l_{31}+l_{33}l_{21}) \\ 2l_{31}l_{11} & 2l_{32}l_{12} & 2l_{33}l_{13} & (l_{31}l_{12}+l_{11}l_{32}) & (l_{32}l_{13}+l_{12}l_{33}) & (l_{33}l_{11}+l_{13}l_{31}) \end{bmatrix} \quad \text{(B.23)}$$

with l_{ij} being the direction cosines of the unit vector V_i with respect to the x_j-axis.

a) Isotropic material

The constitutive matrix for an isotropic material may be expressed as,

$$[D'] = \frac{E}{(1-\nu^2)} \begin{bmatrix} 1 & \nu & 0 & 0 & 0 & 0 \\ \nu & 1 & 0 & 0 & 0 & 0 \\ 0 & 0 & \frac{1-\nu}{2} & 0 & 0 & 0 \\ 0 & 0 & 0 & \frac{1-\nu}{2} & 0 & 0 \\ 0 & 0 & 0 & 0 & \frac{1-\nu}{2S_f} & 0 \\ 0 & 0 & 0 & 0 & 0 & \frac{1-\nu}{2S_f} \end{bmatrix} \quad \text{(B.24)}$$

where E = Young's modulus of elasticity

ν = Poisson's Ratio

S_f = Shear factor (S_f = 1.2, assuming a parabolic variation along the thickness)

The constitutive matrix $\left[D^{'}\right]$ can be decomposed into the matrices $\left[D_m^{'}\right]$, $\left[D_b^{'}\right]$, and $\left[D_s^{'}\right]$, the membrane, bending, and shear components, respectively,

$$\left[D_m^{'}\right]=\frac{Eh}{\left(1-\nu^2\right)}\begin{bmatrix}1 & \nu & 0\\ \nu & 1 & 0\\ 0 & 0 & \frac{(1-\nu)}{2}\end{bmatrix} \tag{B.25}$$

$$\left[D_b^{'}\right]=\frac{h^2}{12}\left[D_m^{'}\right] \tag{B.26}$$

$$\left[D_s^{'}\right]=\frac{Eh}{2S_f\left(1+\nu\right)}\begin{bmatrix}1 & 0\\ 0 & 1\end{bmatrix} \tag{B.27}$$

h is the thickness of the element.

b) Orthotropic material

The constitutive matrices for an orthotropic material can be expressed as,

$$\left[D_m^{'}\right]=h\begin{bmatrix}\frac{E_x^2}{E_x-E_y\nu^2} & \frac{E_xE_y\nu^2}{E_x-E_y\nu^2} & 0\\ \frac{E_xE_y\nu}{E_x-E_y\nu^2} & \frac{E_xE_y}{E_x-E_y\nu^2} & 0\\ 0 & 0 & G_{xy}\end{bmatrix} \tag{B.28}$$

$$\left[D_b^{'}\right]=\frac{h^2}{12}\left[D_m^{'}\right] \tag{B.29}$$

$$\left[D_s^{'}\right]=\frac{h}{S_f}\begin{bmatrix}G_{yz} & 0\\ 0 & G_{xz}\end{bmatrix} \tag{B.30}$$

where E_x and E_y are the Young's modulii of elasticity of the material along the local x_1 and x_2 axes, respectively; G_{xy}, G_{yz}, and G_{xz} are the shear modulii, and v is the Poisson's ratio.

The Young's modulii of elasticity may be expressed in terms of the orthotropic constants D_x and D_y as,

$$E_x = \frac{12D_x\left(1-\nu^2\right)}{h^3} \tag{B.31}$$

$$E_y = \frac{12D_y\left(1-\nu^2\right)}{h^3} \tag{B.32}$$

B.2.5 Element Stiffness Matrix

The element stiffness matrix is computed from,

$$\left[K^e\right] = \int_{\Omega^e} [B]^T [D][B] d\Omega^e \tag{B.33}$$

However, the rotational degrees of freedom are expressed in terms of the local vectors and they should be expressed in terms of the global axes so that they can be assembled properly. Such transformation is obtained from,

$$\left\{d^k\right\}_{global} = \left[T_{rot}\right]\left\{d^k\right\} \tag{B.34}$$

where,

$$\left[T_{rot}\right] = \begin{bmatrix} 1 & 0 & 0 & 0 & 0 & 0 \\ 0 & 1 & 0 & 0 & 0 & 0 \\ 0 & 0 & 1 & 0 & 0 & 0 \\ 0 & 0 & 0 & l_{11} & l_{21} & l_{31} \\ 0 & 0 & 0 & l_{12} & l_{22} & l_{32} \\ 0 & 0 & 0 & l_{13} & l_{23} & l_{33} \end{bmatrix} \tag{B.35}$$

For a four-node shell element, the transformation matrix for rotational degrees of freedom becomes,

$$\left[\widetilde{T}_{rot}\right]=\begin{bmatrix}\left[T_{rot}\right] & [0] & [0] & [0]\\ [0] & \left[T_{rot}\right] & [0] & [0]\\ [0] & [0] & \left[T_{rot}\right] & [0]\\ [0] & [0] & [0] & \left[T_{rot}\right]\end{bmatrix} \tag{B.36}$$

The local nodal degrees of freedom vector in Equation (B.34) includes θ_3 for the proper coordinate transformation. As a result, the element stiffness matrix $[K^e]$ should be expanded to incorporate θ_3 as shown in Equation (B.7). Then the transformed element stiffness matrix is,

$$\left[\widetilde{K}^e\right]=\left[\widetilde{T}_{rot}\right]^{-T}\left[K^e\right]\left[\widetilde{T}_{rot}\right]^{-1} \tag{B.37}$$

B.3 Derivation of the Element Mass Matrix

The element mass matrix is formulated fairly simply. First it is assumed that each degree of freedom has its inertia decoupled from the rest of the system. Then, at each of the four nodes of the shell element, the translation degrees of freedom are attributed a quarter of the mass of the element m^e and the rotational degrees of freedom a quarter of the polar moment of inertia about the corresponding axis of rotation. With L_1^e and L_2^e the dimensions of the element along the x_1^k and x_2^k axes, respectively, the polar moments of inertia of a rectangular element are,

$$\begin{cases} J^e_{x_1^k} = \dfrac{m^e\left(L_2^e\right)^2}{12} \\ J^e_{x_2^k} = \dfrac{m^e\left(L_1^e\right)^2}{12} \\ J^e_{x_3^k} = \dfrac{m^e\left(\left(L_1^e\right)^2+\left(L_2^e\right)^2\right)}{12} \end{cases} \tag{B.38}$$

The mass matrix at all nodes of the element is the same and may then be expressed as,

$$\left[M^k\right] = \begin{bmatrix} \dfrac{m^e}{4} & 0 & 0 & 0 & 0 & 0 \\ 0 & \dfrac{m^e}{4} & 0 & 0 & 0 & 0 \\ 0 & 0 & \dfrac{m^e}{4} & 0 & 0 & 0 \\ 0 & 0 & 0 & \dfrac{J^e_{x_1^k}}{4} & 0 & 0 \\ 0 & 0 & 0 & 0 & \dfrac{J^e_{x_2^k}}{4} & 0 \\ 0 & 0 & 0 & 0 & 0 & \dfrac{J^e_{x_3^k}}{4} \end{bmatrix} \tag{B.39}$$

The element mass matrix may then be written as,

$$\left[M^e\right] = \begin{bmatrix} \left[M^k\right] & [0] & [0] & [0] \\ [0] & \left[M^k\right] & [0] & [0] \\ [0] & [0] & \left[M^k\right] & [0] \\ [0] & [0] & [0] & \left[M^k\right] \end{bmatrix} \tag{B.40}$$

The matrix above is expressed in terms of the running local Cartesian coordinate system. Transformation of coordinates to the global Cartesian coordinate system is necessary to assemble the elements and to write the appropriate equilibrium equations. The transformed element mass matrix is,

$$\left[\widetilde{M}^{e}\right] = \left[T_d\right]^T \left[M^{e}\right] \left[T_d\right] \tag{B.41}$$

where $\left[T_d\right]$ was given in Equation (B.8).